TÉCNICO LISBOA

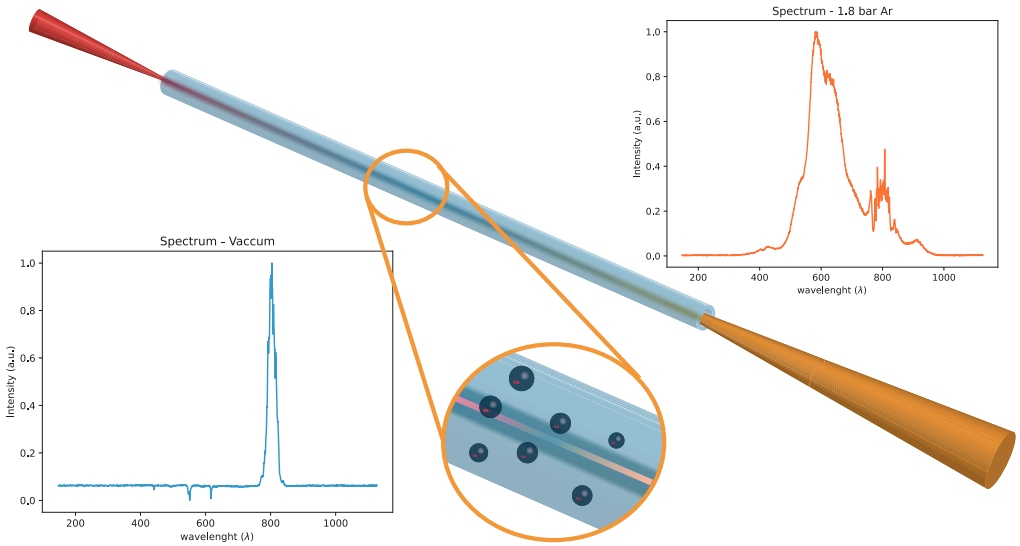

Production of single-cycle laser pulses through nonlinear pulse compression

Mariana da Cunha e Silva

Thesis to obtain the Master of Science Degree in

Engineering Physics

Supervisor: Prof. Marta Leitão Mota Fajardo
Dr. Rodrigo Lopez-Martens

Examination Committee

Chairperson:	Prof. João Alberto dos Santos Mendanha Dias
Supervisor:	Prof. Marta Leitão Mota Fajardo
Members of the Committee:	Prof. Hugo Filipe de Almeida Pires

November 2022

”Lock up your libraries if you like;
but there is no gate, no lock, no bolt that you can
set upon the freedom of my mind.”
– Virginia Wolf

Acknowledgments

To start, I would like to thank my supervisor, the person who first believed I could do this monumental task. Thank you for all the wonderful and exciting discussions about optics and lasers and also for your valuable career and personal advice. Marta, you were not only kind enough to offer me the possibility to study and design post-compression in Instituto Superior Técnico but you also trusted me to adventure on my own, outside of VOXEL, and for that, I offer immeasurable gratitude.

I would also like to thank the whole VOXEL team for being by my side through this crazy ride. Gareth, Patrícia, Sebastião and André, not only did we have important discussions about physics, but you also reminded me constantly of how science can be done with humour and joy.

To my co-supervisor Rodrigo and the rest of the PCO group, thank you for being so kind as to welcome me into your world. I learned so much and left Paris with renewed delight towards the field of laser development.

To Victor, thank you for all the help, I couldn't have done this without your constant non-judgemental aid. You can be my assistant any time you want.

This thesis represents the end of a big chapter in my life. Although the work described in this document spans only one year, it couldn't have happened without the 5 previous ones. For the help in this journey, and because there are not many opportunities in life to exult those who allow me to be here, let me be cheesy for a bit.

To my friends, that stayed by my side through the best and worst moments of the last months, Tomás, Pedro, Diogo, Adriana, Glória, Josué, Pablo, Patrícias, Carolina e Leandro, this work is only here only thanks to your support and care. To Paula and Beatriz, who know all the stories from my stupid teenage years, thank you for staying and not revealing to anyone the mess we were.

To my troupe, Ana, Ricardo and Carolina, I will never be able to thank you enough for picking me up when I was right on the verge of giving up. May we always be able to have our mental health lunches, no matter where we end up in the world.

To Bruno and Varela, who instantaneously became family, thank you for being my home away from home. Your hugs and advice have constantly fixed the cracks in my heart and I hope we never stop being just a little bit weird. To João Pedro, thank you for walking by my side at all points of this course. Your friendship is to me proof that soulmates are sometimes purely platonic.

To my father, thank you for never being afraid to tell me how proud you are of me. To Tiago, who has shown me new wonders in life from the day he was born, I learn so much from you still. To my mother, for holding me up when I couldn't and celebrating all the little things with me. This thesis is not mine, it's ours.

I come to the end of this page realising I have what has to be the best problem ever: too many people to thank and not enough space. To my huge, messy, northern family, I hope you forgive me but I will thank you all by thanking just two of the most important women in my life.

To my aunt, Sónia, who taught me from an early age how beautiful science is, I will forever appreciate the memories of us looking through telescopes, listening to you read to me and the hours of oil painting

we did together. The first time I thought about how important it is to dress up for important moments, was when you took me to the huge confusing world of university laboratories. Years later, I still can't believe I work in one.

Finally, to my grandmother, Maria. Even though the world was sometimes so unkind to you, you never gave up. You will always be an inspiration to me and I will never forget how amazed I was when I walked into your house and, in your 80s, you were reading Steinbeck outside with your fisherman's hat, lounging on your red chair.

This work is supported by the Portuguese FCT– Foundation for Science and Technology under projects PTDC/FIS-PLA/31868/2017, PINFRA/22124/2016 and UID/FIS/50010/2023. It is also supported by the European Union's Horizon 2020 research and innovation programme under grant agreement 871161 and grant agreement No 101047223.

Resumo

Atualmente, a maioria dos lasers ultracurtos são capazes de produzir impulsos com durações na ordem das dezenas de femtossegundos. Estes impulsos ultracurtos são a ferramenta ideal para explorar a dinâmica dos eletrões em átomos, sólidos e nanoestruturas. Como a resolução temporal está limitada pela duração do impulso, alcançar impulsos mais curtos permite-nos explorar os processos inacessíveis até então. Estes impulsos podem existir na forma de impulsos isolados de atossegundos, produzidos por lasers de impulsos com poucos ciclos óticos num processo de geração de harmónicas de ordem elevada, permitindo assim o desenvolvimento de ferramentas de diagnóstico como difração de raios-x nos atossegundos ou espetroscopia com fontes de pequenas dimensões.

Para obtermos impulsos laser de um ciclo ótico, criámos, no laboratório VOXEL (GoLP/IPFN, Instituto Superior Técnico), um sistema de pós-compressão. Utilizando um laser comercial (40 fs, 800 nm, 3 mJ, 1 kHz) impulsos ultra-rápidos são focados numa fibra oca com um diâmetro interno de 250 μm, sujeita a uma pressão diferencial de Árgon. O impulso, com uma maior largura espetral, é re-colimado antes de ser comprimido e analisado por um sistema D-Scan da empresa Sphere Ultrafast Photonics. Produzimos impulsos com menos de 4 fs com pouco GDD e uma transmissão de 33%. Este sistema permite agora que sejam criados, em laboratório, impulsos isolados de atossegundos com frequências na gama mais alta dos ultravioletas.

Estudamos, no *Laboratoire d'Optique Apliquée* (LOA), parte do *Institut Polytechnique de Paris*, dois métodos estado-da-arte da pós-compressão. Apresentamos também conclusões sobre o método mais apropriado para cada situação.

Palavras-chave: ótica não-linear; impulsos lasers de ciclo único;
pós-compressão de impulsos ultracurtos;
impulsos isolados de atossegundo

Abstract

Today's most ultrashort lasers are capable of producing pulses in the order of dozens of femtoseconds. These ultrashort pulses are the tool of choice for exploring electron dynamics inside atoms, molecules, solids, and nanostructures. As temporal resolution is limited by pulse duration, achieving shorter pulses allows us to look at previously hidden processes. This can be achieved with isolated attosecond pulses (IAPs) produced through few-cycle laser-driven high-harmonic generation (HHG), unlocking diagnostic tools like attosecond x-ray diffraction, and spectroscopy with tabletop sources.

To achieve the few-cycle laser pulses, we created a post-compression installation at the Voxel laboratory (GoLP/IPFN at Instituto Superior Técnico). Our setup consists of a Coherent Astrella laser (40 fs, 800 nm, 3mJ, 1kHz) whose output is focused onto a 250μm inner diameter differentially pumped hollow core fibre, pressurized with Argon gas. The spectrally broadened output from the hollow core fibre is recollimated before the beam is both compressed and measured in time by a d-scan system from Sphere Ultrafast Photonics. We have achieved sub-4 fs with minimal group delay dispersion (GDD) and transmission of 33%. The setup represents a powerful tool for table-top single-cycle laser pulses in laboratories and we are now ready to produce attosecond pulses in the XUV region through high-harmonic generation.

There was also a study done at the *Laboratoire d'Optique Apliquée* (LOA), a part of *Institut Polytechnique de Paris*, where two state-of-the-art methods of post-compression were performed and analysed. A conclusion regarding the most appropriate method for different situations is also presented.

Keywords: nonlinear optics; single-cycle laser pulses;
ultrashort post-compression; isolated attosecond pulses

Contents

List of Tables

List of Figures

Acronyms

CEP Carrier Envelope Phase.

CPA Chirped Pulse Amplification.

FROG Frequency Resolved Optical Gating.

FTL Fourier Transform Limited.

FWe2 full width at $1/e^2$.

FWHM full width at half maximum.

GDD Group Delay Dispersion.

HCF Hollow-Core Fiber.

HHG High-Harmonic Generation.

IAP Isolated Attosecond Pulses.

MIIPS Multiphoton Intrapulse Interference Phase Scan.

MPC Multipass Cell.

NIR near infrared (760 nm - 1500 nm).

RMS Root Mean Square.

SHG Second Harmonic generation.

SPM Self-Phase modulation.

TOD Third-Order Dispersion.

XPW Cross-Polarized Wave Generation.

XUV extreme ultraviolet (10 nm - 124 nm).

Chapter 1

Introduction

We humans are very limited in the timescales that we can perceive. While a plant grows too slowly for us to be able to grasp it, a bee beats its wings too fast. To see any of these phenomena we need to take several snapshots of the event at the appropriate time scales. We can only recognise a tiny fraction out of all the natural processes, these range from the age of the universe (4.5×10^{17} s) down to the atomic unit of time (2.4×10^{-17} s) or shorter. The fraction we can visualise is around the centre of this vast scale. It is not surprising that our heart rate of around $1\ s^{-1}$ serves as a reference.

In 1999, Ahmed Zewail was awarded the Nobel Prize in Chemistry for femtochemistry, a solution to our lack of ability to see the vibrations of atoms and molecules, resolving motion at the femtosecond scale for the first time through pump-probe experiments. Innovations have also been made at the attosecond scale, that of the electron dynamics in atoms, molecules, and solid-state matter. There are currently two methods for measuring these ultrafast dynamics in matter: ultrafast electron diffraction and attosecond spectroscopy. Both are quite similar to the pump-probe experiments in femtochemistry: the former uses an electron bunch of a few femtoseconds in duration as a pulse and the latter attosecond light pulses.

In Instituto Superior Técnico, pulses at the femtoseconds regime, enabling these techniques, have been hosted since 2017 at the VOXEL laboratory[1]. Being one of few facilities in Portugal dedicated to such short pulses, the VOXEL group takes advantage of a process called High-Harmonic Generation (HHG) to create some of the shortest man-made pulses. These pulses need to be in higher frequencies since for each wavelength there's a limit to the pulse duration. In the NIR region, like our femtosecond pulses, the limit is set at around 2.5 fs, for soft X-Ray pulses the limit is much lower, in the attosecond range.

HHG is normally achieved by using femtosecond lasers and a gas cell to produce pulses in the extreme ultraviolet (10 nm - 124 nm) region with hundreds of attoseconds. Having achieved a reliable coherent XUV source [1] a few years ago, the group is now looking to progress towards Isolated Attosecond Pulses (IAP). These even shorter durations promise new insight into physical, chemical, and biological processes, thanks to the previously mentioned methods of attosecond x-ray diffraction and

[1] The VOXEL laboratory is part of the Group of Lasers and Plasmas of Instituto de Plasma e Fusão Nuclear. https://www.ipfn.tecnico.ulisboa.pt/VOXEL

spectroscopy with tabletop sources. Imaging techniques with IAP require hundreds of μJ of energy on target [2] with pulse durations close to the single-cycle regime, i.e. less than 4fs in 800 nm.

Pulses with such characteristics are on the front edge of laser technology. Since the invention of the laser in 1960, we have seen several remarkable advances in the development of ultrafast laser systems, in particular, the Chirped Pulse Amplification (CPA) technique [3], illustrated in figure 1.1, for which Gérard Mourou and Donna Strickland were awarded the 2018 Nobel Prize in Physics. This technique allowed the development of brighter and shorter laser sources after a hiatus of two decades when damage in the laser's gain medium implied that higher energy lasers could only arise from extremely large laser facilities. With CPA now an established technique, most ultrashort lasers are already capable of producing pulses in the order of a few of femtoseconds using mode-locked Ti:Sapphire oscillators with several millijoules of energy. However, commercial lasers have a clear limit: the pulse duration is limited to tenths of femtoseconds due to the limited gain bandwidth of the amplifying medium. As we just referred, Isolated Attosecond Pulses need not only high enough energy but also pulse durations in the order of 3-5 fs, this needs however to occur after the amplification of the laser.

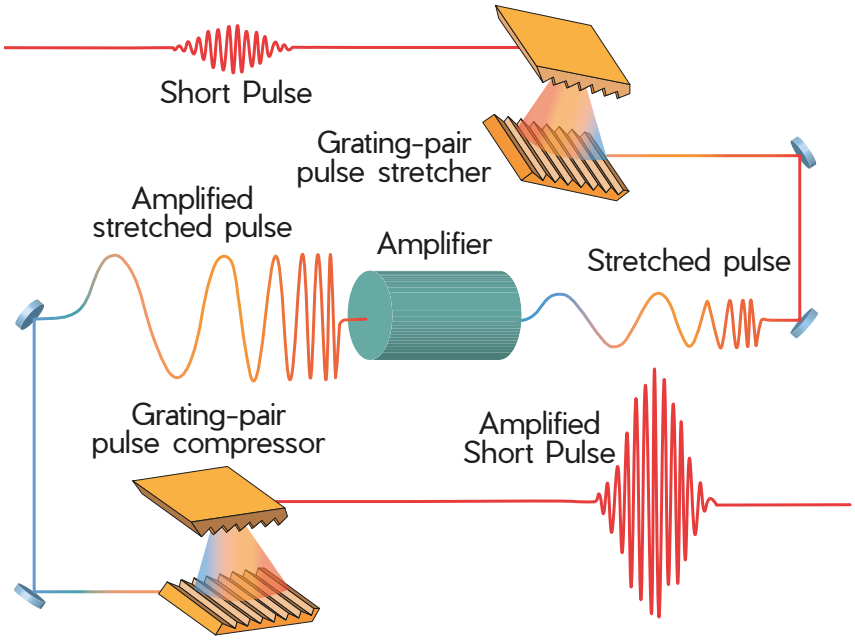

Figure 1.1: Schematic of the CPA method. A technique used to amplify ultrashort laser pulses to the Petawatt level.

This thesis is part of the IMPULSE project [2] (**I**ntegrated **M**anagement and reliable o**P**erations for **U**ser-based **L**aser **S**cientific **E**xcellence) which is connected to ELI (Extreme Light Infrastructure). In the ELI-Alps[3], beam time of attosecond pulses is available for users having also a group dedicated to single-cycle lasers (SYLOS laser). For the widening of the ELI project, it makes sense to develop skills in the applications of single-cycle laser pulses outside of the main facilities, this thesis tries to accomplish exactly that.

[2] https://eli-laser.eu/impulse/
[3] https://www.eli-alps.hu/

1.1 Description of Ultrashort pulses and Nonlinear Optics

To achieve the desired single-cycle pulses, we need to start by looking at the fundamental behaviour of electromagnetic wave packets: a pulse can be fully described either in the time or in the frequency domain which are connected by the Fourier transform. This is, of course, analogous to particles in quantum mechanics where the domains in question are momentum and space. And so, we have the bandwidth theorem where the product of the representation of the two domains can not be arbitrarily small but must respect a minimum value. In quantum mechanics this is known as Heisenberg's uncertainty relation, in ultrafast optics, it reads as

$$\Delta\omega \cdot \Delta t \geq \text{constant}, \tag{1.1}$$

where $\Delta\omega$ is the spectral bandwidth and Δt is the pulse duration. When the product is at its minimum value we say that it is at the Fourier Transform Limit (FTL).

We have then two goals: (i) we need to achieve a broad enough bandwidth to allow a shorter pulse and (ii), all the components of the spectral phase have to be compensated into the same value (to achieve FTL). As said before, common lasers have too narrow a gain bandwidth, therefore the spectrum of their pulses cannot be broadened within the laser itself. Instead, the beam needs to be broadened outside the laser source before it can be compressed to a single-cycle duration [4]. This technique is called **post-compression** (compression after broadening) and is the core of this work [4].

1.1.1 Temporal Domain

Just looking at the temporal description of a laser pulse we can separate the electric field into a real-valued amplitude and a complex oscillating part,

$$\vec{E}(t) = \vec{E_0}(t) \cdot \exp(-i\phi(t)), \tag{1.2}$$

where $\phi(t)$ is called the temporal phase. The actual observable electric field needs to be of course a real-valued quantity

$$\vec{\mathcal{E}}(t) = \frac{1}{2}\vec{E}(t) + cc. \tag{1.3}$$

E_0 relates to the shape of the pulse, i.e. the temporal intensity profile, whereas the intensity of a laser pulse is defined as a time-averaged quantity – averaged over a time longer than the field oscillations, but short enough for the timescale of interest. This leads to:

$$I(t) = \frac{1}{2\eta} \cdot |E(t)E*(t)| \tag{1.4}$$

[4] There's also an alternative to spectral broadening: to find a media that provides enough bandwidth to create or amplify few-cycle pulses. An arbitrary broad spectral range is supported by optical parameters amplifiers and is only limited by phase-matching conditions and the spectral transmission range of the amplifying medium. Optical parametric chirped-pulse amplifiers (OPCPA) can be a solution, having enough bandwidth for direct few-cycle generation [5]. That solution is, however, out of the scope of this thesis.

with $\eta = \sqrt{\mu_0/\varepsilon}$, $\varepsilon = \varepsilon_0 \cdot (1 + \chi^{(1)})$.

A typical temporal pulse shape is the well know Gaussian form,

$$I(t) = I_0 \cdot \exp(\frac{t^2}{2 \cdot \tau^2}) \tag{1.5}$$

We need then a definition of the temporal width of the pulse, this is done by calculating the mean square deviation of a pulse centred in $t = 0$,

$$\sigma_\tau^2 = \frac{\int_{-\infty}^{+\infty} t^2 I(t)}{\int_{-\infty}^{+\infty} I(t)} \tag{1.6}$$

For a gaussian profile, this is identical to the usual quantity full width half maximum (FWHM), $\tau_{FWHM} = 2\sqrt{2\ln 2}\sigma_\tau$ and to the full width at $1/e^2$ (FWe2) as $\tau_{FWe2} = 4 \cdot \sigma_\tau$.

Of the utmost importance to this is work is also the temporal phase, $\phi(t)$, with some intuitive and key properties,

$$\phi(t) = \phi_0 - \omega_0 \cdot t + \phi_{NL}(t), \tag{1.7}$$

ω_0 is the carrier frequency with which the field oscillates and ϕ_0 is the temporal offset from the field maxima to the envelope peak, as can be seen in figure 1.2. Although negligible in long pulses, where there are several oscillations of the electric field, the Carrier Envelope Phase becomes significant in the single-cycle regime as will be explained in this chapter.

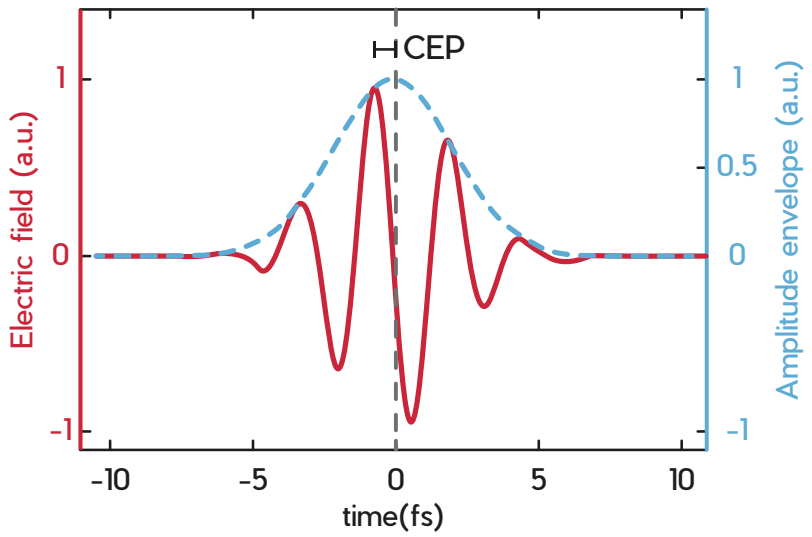

Figure 1.2: Electric field of a few-cycle laser pulse where the field oscillations are shifted relative to the pulse envelope by the CEP. Adapted from [6]

One of the most important concepts for this thesis arises from $\phi_{NL}(t)$, a nonlinear component that leads to an instantaneous frequency shift throughout the pulse. We will look into this further in the chapter.

1.1.2 Spectral Domain

An ultrashort pulse can also be described in the spectral domain, a natural consequence of the Fourier Transform. From this, the pulse can be decomposed from an oscillating field into overlaying monochromatic waves with a given phase offset. In linear optics, the monochromatic waves can be treated as separate during propagation and so there's an easy understanding of how the material affects the pulse shape.

Defining the spectral amplitude from the Fourier transform

$$\tilde{E}(\omega) = \frac{1}{\sqrt{2\pi}} \int_{-\infty}^{+\infty} E(t) \cdot \exp(-i\omega t) \mathrm{d}t. \tag{1.8}$$

We can then do the same separation as before, one real amplitude part $A(\omega)$ and a complex term,

$$\tilde{E}(\omega) = A(\omega) \cdot \exp(i\varphi(\omega)) \tag{1.9}$$

where $A(\omega) = |\tilde{E}(\omega)|$.

We can here, as before, define an intensity,

$$\tilde{I}(\omega) = \frac{1}{2\eta} |\tilde{E}(\omega)|^2 \tag{1.10}$$

and spectral width,

$$\sigma_\omega^2 = \frac{\int_{-\infty} + \infty \omega^2 \tilde{I}(\omega_0 + \omega)}{\int_{-\infty} + \infty \tilde{I}(\omega)} \tag{1.11}$$

The temporal and spectral width are related through the uncertainty principle described in the beginning, $\sigma_\tau \sigma_\omega \geq FTL$. The minimum value of this inequality depends on the pulse shape, tipical values are $TBP_{Gaussian} = 0.441$ for a Gaussian shape and $TBP_{Sech^2} \approx 0.315$ for a sech^2 shape.

The phase in equation 1.9 can be developed into a Taylor series around the central frequency ω_0 making some effects much more intuitive,

$$\varphi(\omega) = \varphi_0 + \varphi^{(1)} \cdot (\omega - \omega_0) + \frac{\varphi^{(2)}}{2} \cdot (\omega - \omega_0)^2 + \frac{\varphi^{(3)}}{6} \cdot (\omega - \omega_0)^3 + \cdots \tag{1.12}$$

with $\varphi^{(n)} = \frac{\mathrm{d}^n \varphi}{\mathrm{d}\omega^n}|_{\omega_0}$, φ_0 again relates to CEP.

The envelope of a light pulse as seen in figure 1.2 travels at the group velocity v_g,

$$v_g = \frac{\partial \omega}{\partial k} \tag{1.13}$$

and so we can see that the second term, $\varphi^{(1)}$, corresponds to the group delay, a quantity that gives information regarding the delay in the time of the pulse envelope relative to a given reference. This is usually not of interest.

$\varphi^{(2)}$ is called the group delay dispersion (GDD) or chirp, a quantity which describes how different spectral lines travel at different velocities. In fact, from this term, we map a linear group delay versus

frequency relation. This type of phase change leads to a longer pulse than what could be obtained from the spectral bandwidth. The broader the spectrum, the stronger the influence of higher order terms is. Due to 1.1, which tells us that at FTL a shorter pulse has larger bandwidth, a 3.5 fs pulse (with a centre wavelength of 800 nm and gaussian shape) travelling through only 1mm of glass will be stretched to 29 fs, so an eight times increase. On the other hand, a 25 fs long pulse stretches only by 1.3% of its original duration [6, 7].

$\varphi^{(3)}$ or third order dispersion (TOD) leads to a quadratic group delay versus frequency relation and, for example, to the generation of pre or post-pulses. A visual explanation of these effects is present in figure 1.3, on the left we can see how GDD affects the duration of the pulse while on the right we see how TOD is related to the formation of post pulses.

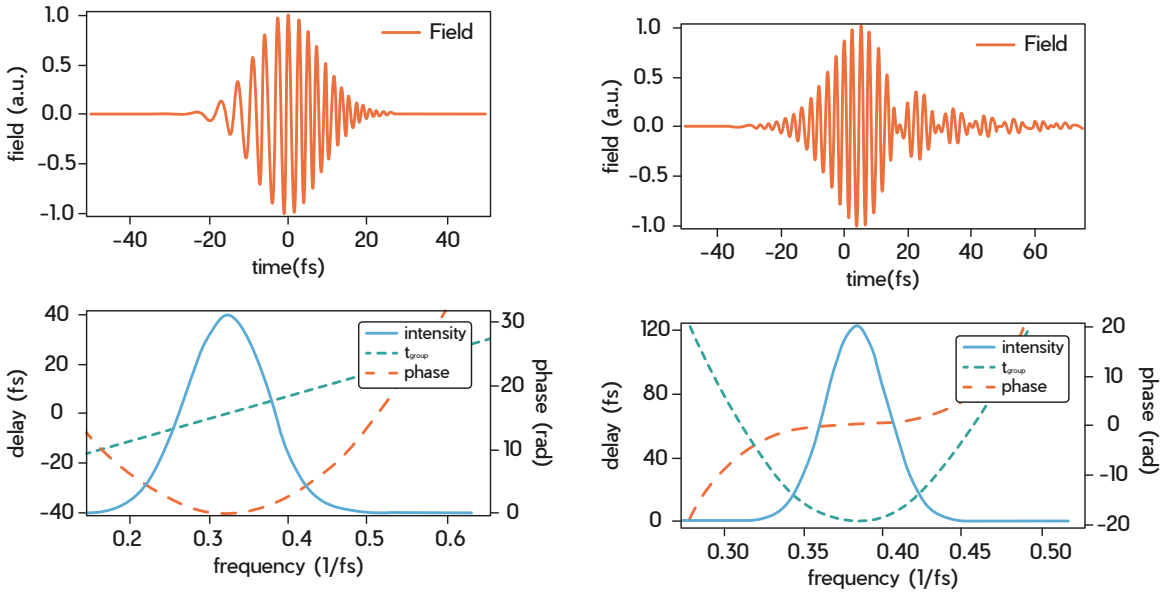

Figure 1.3: Effects on the pulse shape coming from a quadratic (pure GDD, left) or cubic (right) spectral phase. Adapted from [8]

Higher order phase terms also lead to pulse distortion. In fact, when an optical pulse with low peak intensity travels through a dispersive $n(\omega)$ medium of length L we can apply the linear approximation to the acquired spectral phase,

$$\varphi(\omega) = \frac{n(\omega)}{c}\omega L. \tag{1.14}$$

1.1.3 Notes on Nonlinear Optics

Nonlinear optics is the study of phenomena that occur as a consequence of the modification of the optical properties of a material system by the presence of light. Typically, only laser light is sufficiently intense to modify the optical properties of a material system. Examples of such optical phenomena appear in this work as so there's a need to quickly address it here.

In order to describe more precisely what we mean by optical nonlinearity, let us consider how the dipole moment per unit volume or polarisation $\tilde{P}(t)$, of a material system depends on the strength $\tilde{E}(t)$ of an applied optical field. In linear optics, the induced polarisation depends linearly on the electric field strength in such manner,

$$\tilde{P}(t) = \epsilon_0 \chi^{(1)} \tilde{E}(t) \tag{1.15}$$

where $\chi^{(1)}$ is known as the linear susceptibility and ϵ_0 is the permittivity of free space. When we cross to higher intensities and get into the field of nonlinear optics, the optical response needs to be written differently. While equation 1.15 is correct, it only accounts for $\chi^{(1)}$ and so we need to generalise by expressing $\tilde{P}(t)$ as a power series in the field strength $\tilde{E}(t)$. It is represented by 1.16 in an isotropic media.

$$\begin{aligned} \tilde{P}(t) &= \epsilon_0 \left[\chi^{(1)} \tilde{E}(t) + \chi^{(2)} \tilde{E}^2(t) + \chi^{(3)} \tilde{E}^3(t) + \cdots \right] \\ &\equiv \tilde{P}^{(1)}(t) + \tilde{P}^{(2)}(t) + \tilde{P}^{(3)}(t) + \cdots . \end{aligned} \tag{1.16}$$

Here, we find $\chi^{(2)}$ and $\chi^{(3)}$, known as the second and third-order nonlinear optical susceptibilities, respectively.

An example of a $\chi^{(2)}$ is the process of second-harmonic generation and an example of a $\chi^{(3)}$ is the process through which there is the creation of an intensity-dependent refractive index, both of these processes occur in this thesis and will be further described [5].

1.2 High Harmonic Generation and Isolated Attosecond Pulses

High Harmonic Generation, refers to the process where, by the non-linear interaction of a high-intensity laser pulse with a gas (or solid) target, harmonics with odd multiples of the incident laser frequency are created. At the level of an individual atom or molecule, the process can be explained through a three-step model [11], represented in figure 1.4. In the first step, the electron is ionised from the atom by tunnelling. In the second step, this electron is accelerated by the electric field of the laser. Finally, in the third step, the same electron recombines with the atom and the kinetic energy that it gained in the second step is emitted as radiation. This process is repeated at every half period of the laser's electric field (hence the odd harmonic frequency spectrum) and is highly temporal and spatially coherent [12].

IAP can appear from several gating mechanisms applied on normal "long" pulses [12]. However, using single cycle driving pulses is still the only way to ensure the proper and constant creation of the attosecond pulses desired since employing single (or few) cycle(s) laser pulses naturally restricts the emission of the highest energetic photons to a single (or double) event. This is illustrated in figure 1.5 where the blue dashed line represents the threshold necessary to create the highest order of harmonics. If one can control the CEP value, and sets it to $\phi = 0$, there is only one peak with high enough energy that can create higher order harmonics, this is, only one isolated attosecond bunch can be emitted.

[5] More information can be consulted in the first chapter of [9]

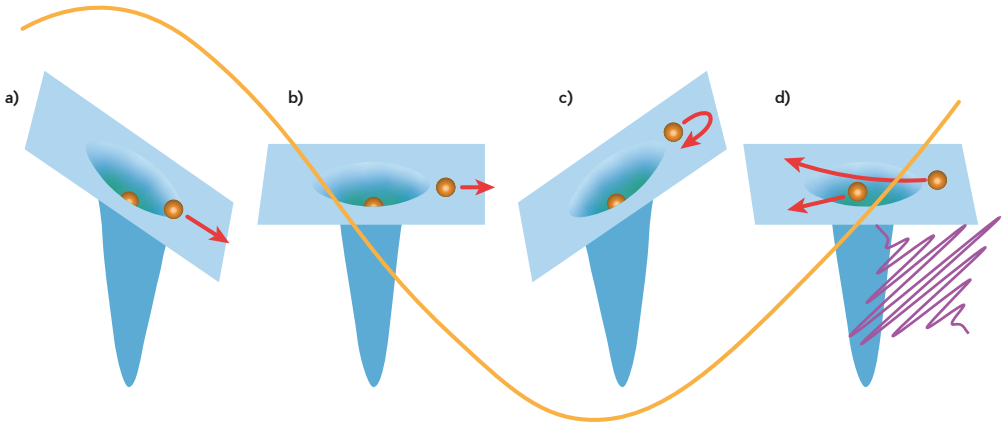

Figure 1.4: The three-step model of HHG. a–d) An intense femtosecond near-infrared or visible pulse (yellow) extracts an electron wave packet from an atom or molecule. First, the electron is pulled away from the atom near the peak of the optical field (a) and accelerated (b). When the optical field reverses, the electron is driven back (c) where it can *recollide* during a small fraction of the laser oscillation cycle (d). This way the parent ion sees an attosecond electron pulse that can be used directly, or its kinetic energy, amplitude and phase can be converted to high harmonics on recollision. [10]

This singularity destroys the discrete nature of harmonics at high energies since there is no interference between attosecond pulses of the same nature anymore and the HHG spectrum becomes continuous [13–16]. If, however, there is no CEP control, a second situation can also occur where the threshold can hold two peaks of high intensity of the electric field. When this occurs there is interference between the two emitted bunches and the spectrum becomes discrete again.

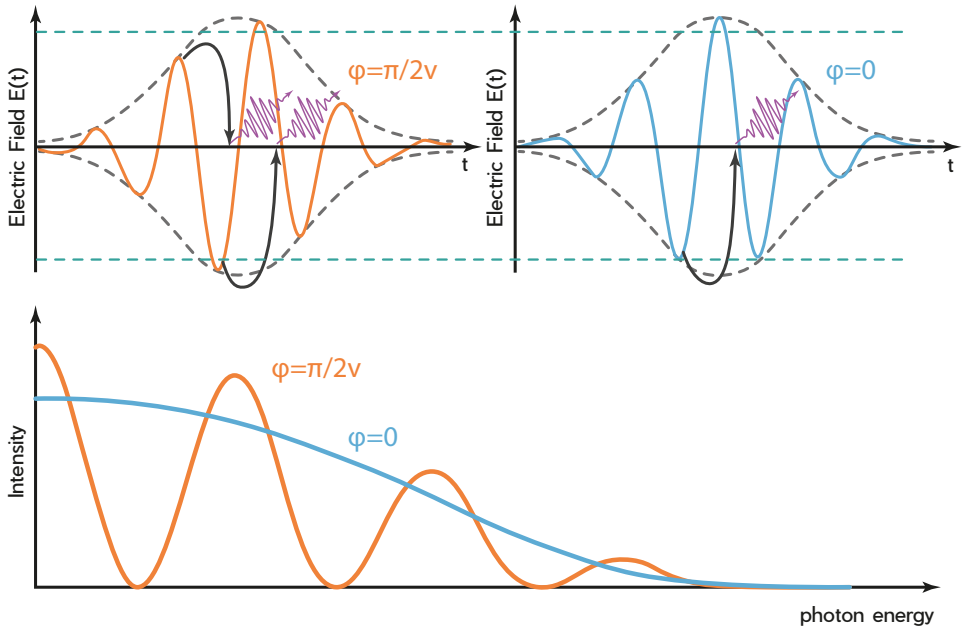

Figure 1.5: Emission of soft X-rays with the highest photon energy with different values of CEP, the blue dashed lines define the threshold necessary to create the highest order of harmonics (top) and X-Ray spectral distribution in the cut-off range (bottom).

At the VOXEL laboratory, there is no way to measure or control the Carrier Envelope Phase and so we will have a mixture of the two situations. This is not an isolated attosecond source but will, in any case, create much shorter harmonics than those available until now.

1.3 Fundamentals of Post Compression

To understand the potential and limits of post-compression we need to first look at the fundamentals of spectral broadening, the process through which we achieve a broader spectrum. We are going to focus on self-phase modulation (SPM), the typical nonlinear process used on post-compression techniques. Spectral broadening can, however, also occur through other nonlinear effects such as photoionisation.

The electric field of an ultrafast laser pulse propagating in the z axis can be described as the equation shows.

$$E(t,z) = A(t,z)cos(\phi(t,z)) \tag{1.17}$$

with an envelope $A(t,z)$ and a phase term

$$\phi(t,z) = \omega_0 t - k_0 z = \omega_0 t - z\omega_0 \frac{n}{c} \tag{1.18}$$

where ω_0 denotes the angular carrier frequency, n the refractive index of the medium and c the speed of light in vacuum. It's also of interest to describe then the instantaneous frequency i.e, the time-derivative of the phase term,

$$\omega_{inst}(t,z) = \frac{\partial \phi}{\partial t} = \omega_0 - \frac{\omega_0}{c}\frac{\partial n(t,z)}{\partial t} z. \tag{1.19}$$

When we described ultrashort pulses we only discussed how the beam propagates in a material where the light field is sufficiently weak, this is, when we need only to consider $n = n_0$. That isn't always the case, in fact, the correct way of presenting the refractive index in many materials is the following,

$$n = n_0 + n_2 \left\langle \tilde{E}^2 \right\rangle + \cdots \tag{1.20}$$

where n_0 represents the usual, weak-field refractive index and n_2 is a new optical constant (also called the second-order index of refraction) that indicates how the refractive index changes with different intensities of light. This is called the optical Kerr effect.

As we saw before, in equation 1.16, the interaction of light with a nonlinear material can also be described in terms of nonlinear polarisation. While the general form of third-order interactions induced by a field is not presented here (since the nonlinear polarisation has 44 possible different complex amplitudes) [6], we want still to present a portion of the general case, the part that influences the propagation of a beam of frequency ω,

[6] But can be consulted, again, in subsection 1.2.9 of [9]

$$P^{NL}(w) = 3\epsilon_0\chi^{(3)}(w = w + w - w)\,|E(\omega)|^2\,E(\omega) \tag{1.21}$$

Again, for some simplification, we are assuming a linearly polarised beam and suppressing the tensor nature of $\chi^{(3)}$. The total polarisation of the material is then

$$P^{TOT}(\omega) = \epsilon_0\chi^{(1)}E(\omega) + 3\epsilon_0\chi^{(3)}|E(\omega)|^2E(\omega) \tag{1.22}$$

where a new quantity appears, the effective susceptibility

$$\chi_{eff} = \chi^1 + 3\chi^{(3)}\,|E(\omega)|\,, \tag{1.23}$$

that we can relate to the refractive index by $n^2 = 1 + \chi_{eff}$. Using equations 1.20 and 1.23 and some algebra we find how the linear and nonlinear refractive indices are related to the linear and nonlinear susceptibilities,

$$n_0 = (1 + \chi^{(1)})^{1/2} \tag{1.24}$$

and

$$n_2 = \frac{3\chi^{(3)}}{4n_0}. \tag{1.25}$$

Looking back on equation 1.19, we can be remembered that the instantaneous frequency is dependent on the refractive index. It makes then sense to rewrite the mathematical quantity with our new intensity-dependent refractive index. This equation is the reason why we can create new frequencies when the beam passes through a nonlinear medium, a process we call spectral broadening,

$$\omega_{inst}(t,z) = \frac{\partial\phi}{\partial t} = \omega_0 - n_2\frac{\omega_0}{c}\frac{\partial I(t,z)}{\partial t}z. \tag{1.26}$$

How much the Kerr effect modifies the pulse can be quantified by the B-integral, a measure of the nonlinear phase shift of light here presented for constant n_2 and I.

$$B = \frac{\omega_0}{c}\int_0^L n_2(z)I(z)dz = \frac{2\pi}{\lambda}n_2I_0L_{eff} \tag{1.27}$$

where $\lambda = 2\pi c/\omega_0$ is the central wavelength in vacuum, $I_0 = I(t = 0, z = 0)$ the peak intensity of the input pulse and $L_{eff} = \int_0^L n_2(z)/n_2 \cdot I(z)/I_0 dz$ is the effective length of the nonlinear interaction. The effective length takes into account intensity changes during propagation, e.g. due to losses or gain and also if the nonlinearity of the medium changes due to pressure variations in gases.

SPM due to the Kerr Effect can also be seen as a change in the phase velocity $v_{ph} = \omega/k = c/n$ and changes in the refractive index will then lead to spectral broadening as before. Taking then a look at the group velocity, $v_g = \partial\omega/\partial k = c/(n + \omega\partial k/\partial\omega)$, it becomes clear that this too will be intensity-dependent. As the pulse envelope propagates with the group velocity, the peak of the pulse will propagate slightly slower than its flanks. Therefore, the slope of its leading edge decreases while the falling edge will be

steeper and there will be a more enhanced blueshift of the spectrum (as in figure 1.6). This effect is called self-steepening and in extreme cases will create wings in the blue region of the spectrum that are no longer compressible [17].

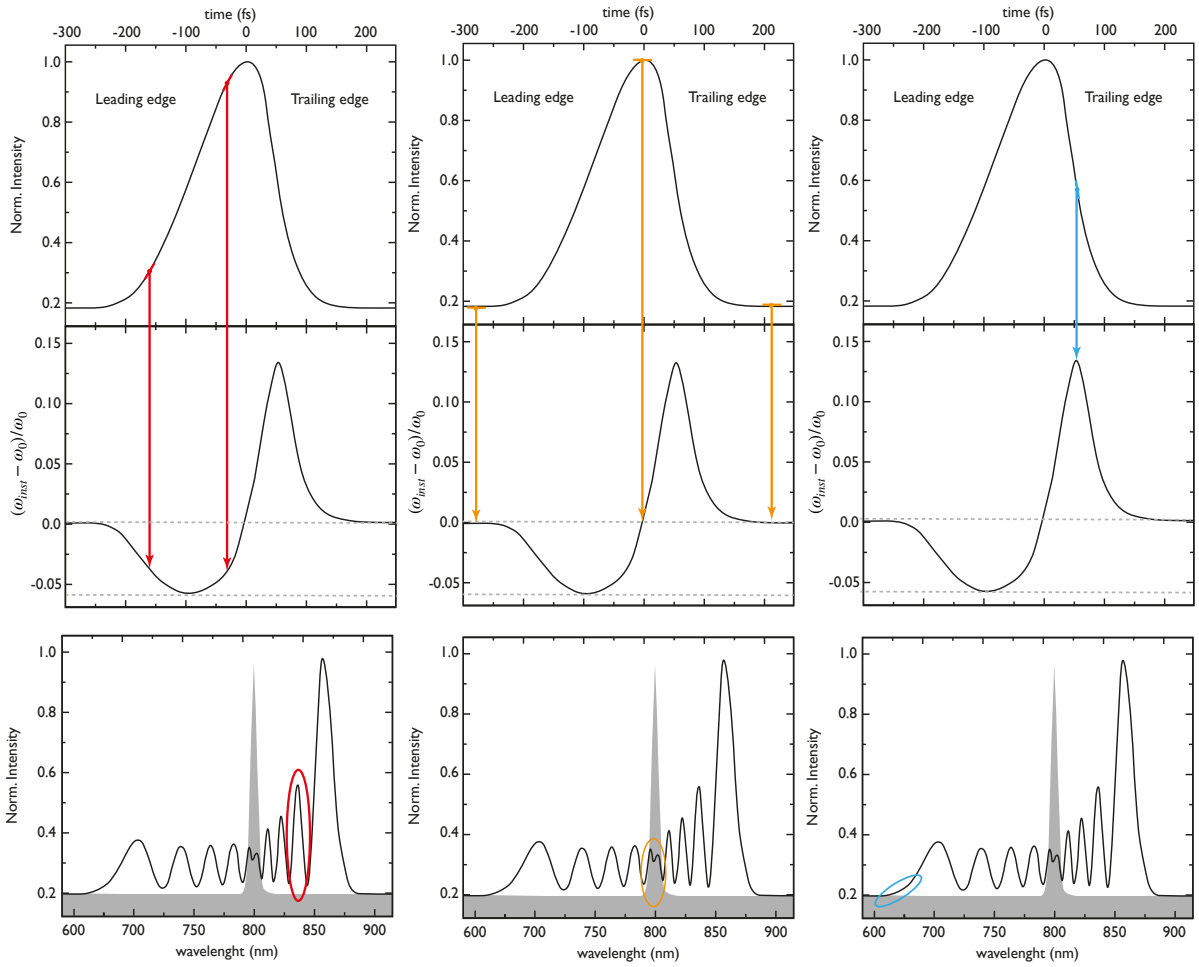

Figure 1.6: Self-phase modulation due to the optical Kerr-effect. For each section of the pulse we have (a) input pulse shape, (b) normalised instantaneous angular frequency shift, (c) SPM-broadened spectrum at a B-integral of 9π (the input spectrum is marked by a shaded area). Inspired by [4].

The Kerr effect also modifies the spatial properties. Gaussian beams collect maximum phase shift at the centre of the beam profile during propagation in Kerr-media and the phase shift gradually decreases as the intensity drops along the beam radius. This is analogous to propagation through a convex lens, and so this effect is normally called self-focusing. Depending on the intensity of the nonlinear effect, the Kerr lensing can overcome the natural divergence of the free propagating beam. Since both effects induce a spherical wavefront curvature which scales inversely to the square of the beam size, it is not the intensity but the peak power that governs the effect. If the peak power reaches the critical power of self-focusing (P_{cr}) then the effects balance and the beam size remain constant through propagation, after this threshold, the beam will be focused. Critical power is calculated as

$$P_{cr} = \frac{1}{2\pi}\frac{\lambda^2}{n_0 n_2}. \tag{1.28}$$

1.3.1 Spectral Broadening during free propagation

Propagating a beam freely inside a homogeneous nonlinear media is the simplest picture of a spectral broadening method. The method has, however, its limitations: (i) the spectral broadening is proportional to the B-integral and so it can vary across the beam profile if the intensity is not uniform, (ii) if the peak power rises over the critical power then we have self-focusing, this occurs not only in the full beam but also on the smaller scale which leads to beam break up [18]. This can be corrected by dividing the interaction into smaller stages with a moderate B-integral and then filtering the beam between stages.

Free propagation in bulk

The idea of using bulk materials for post-compression of ultrashort laser pulses was first suggested by C. Rolland and P. B. Corkum [19] in 1988 and then also discussed by Petrov et al in 1989 [20]. These early results achieved 19-24fs pulses with 7-110 μJ by filtering out the wings of the beam. This comes however with a problem, the trade-off between spectral uniformity and temporal profile left a transmission of only $4-20\%$. More recently, a group in Russia has achieved 3.25J at an average duration of 13fs since, in fact, the pulse duration strongly varied from 6.4fs to 29fs along the beam profile [21].

Multi-plate continuum generation

Although it seems similar to the previous method, multi-plate compression is indeed quite different. In this method, several slabs of a nonlinear medium are carefully distributed around one or more foci of the propagating beam [22].

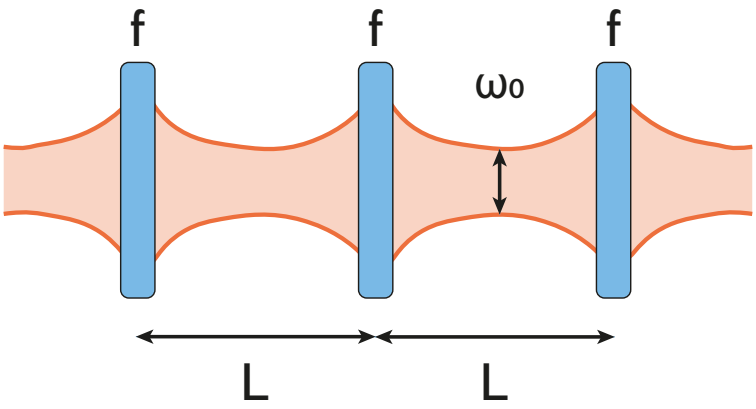

Figure 1.7: Schematics of the method of multi-plate continuum generation. Adapted from [23].

In this way, by limiting the nonlinearity at each stage, the interaction geometry can keep the Spatio-temporal couplings under control. The downside is the poor energy scalability available (sub-mJ regime)

and the existing spacial chirp of the output beam [24]. The method is in any case described by figure 1.7.

Multi-Pass Cells

Similar to the multi-plate compression's idea of having the nonlinear interaction happen within the sequence of foci, multi-pass cells take advantage of the same regime but creates it with reflective optics. In this technique, a Herriott-type cell is employed to preserve the beam parameters and behaves like a "discrete" waveguide. This allows meters-long interaction at low local B-integral, a condition necessary to maintain the beam parameters and so match the cavity. At first, slabs of glass were incorporated in the cavity as the nonlinear medium for low-energy (few μJ) lasers. More recently, to increase the energy, the cavity has been closed and filled with a noble gas [25, 26].

Multi-pass cells exhibit great throughput in the range of $85 - 96\%$ depending on the number of roundtrips and the reflectivity of the cavity mirror. Recently, M. Müller et al achieved spectral broadening with 388W output average power and 776μJ pulse energy. This was obtained at 82% cell transmission with a high output beam quality ($M_2 < 2.3$) and spatio-spectral homogeneity (97.5%), reaching compression of the output pulses down to 6.9 fs duration [27]. This method will be further discussed in chapter 4.

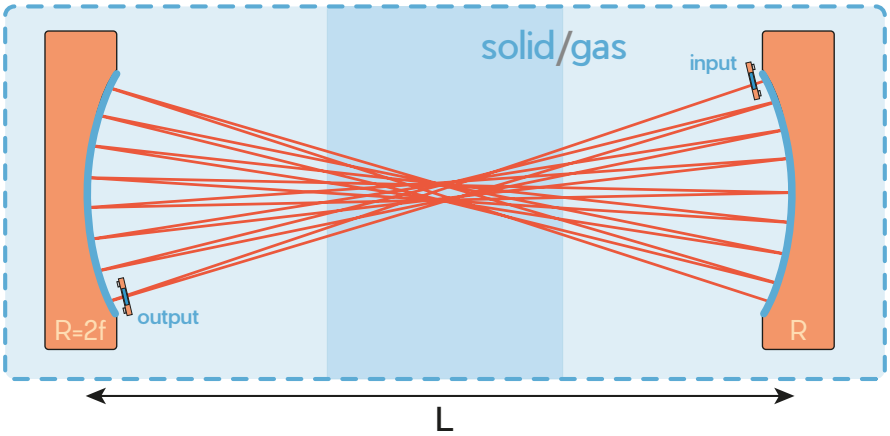

Figure 1.8: Schematic layout of a nonlinear MPC. The nonlinear medium is either a bulk slab inserted inside the cell (dark blue) or a gas surrounding the cell (light blue). Adapted from [23].

1.3.2 Spectral Broadening in waveguides

Waveguides can be a solution for two problems of free-space propagation: (i) In a waveguide the pulses maintain their beam size and so high intensity on an extended length defined only by the geometry of the waveguide, which is larger than the Rayleigh length of a focus by several orders of magnitude. This allows for the accumulation of large B-integrals and therefore we can have extended spectral broadening. (ii) The beam undergoes constant reflections throughout the waveguide, creating coherent mixing of

different parts of the beam and forming eigenmodes. These eigenmodes have the same spectral and temporal behaviour over the entire beam profile allowing perfect pulse compression [4].

To achieve controlled spectral broadening with minimal losses, it has been shown that one needs to fulfil two limiting criteria [28]. First, the peak power of the input pulse should be below the critical power of self-focusing,

$$P_0 < P_{cr} = \frac{1}{2\pi}\frac{\lambda^2}{n_0 n_2}. \tag{1.29}$$

Secondly, the peak intensity should stay below the ionisation threshold of the nonlinear media,

$$I_0 < I_{th}. \tag{1.30}$$

In a waveguide each eigenmode has its effective area A_{eff} which is dependent only on the mode profile,

$$I_0 = \frac{P_0}{A_{eff}}. \tag{1.31}$$

According to the first criteria (equation 1.29), while increasing the peak power, self-focusing can still be avoided if the critical power is also to rise. This requires the reduction of the nonlinear refractive index,

$$n_2 < \frac{1}{2\pi}\frac{\lambda_2}{n_0 P_0}. \tag{1.32}$$

This, when looked through the definition of B-integral, equation 1.27, becomes

$$B = \frac{2\pi}{\lambda} n_2 I_0 L_{eff} < \frac{\lambda}{n_0}\frac{L_{eff}}{A_{eff}} \tag{1.33}$$

This means then that, for a given central wavelength, one needs only to worry about the fibre length to avoid self-focusing.

We now need to look at the second criterion. To avoid ionisation by scaling the peak power the effective mode area also needs to be increased according to 1.31, $A_{eff} > \frac{P_0}{I_{th}}$. This can be summed up as a single, combined relationship showing the limits of spectral broadening during a well-controlled propagation inside a waveguide:

$$B < \frac{\lambda}{n_0}\frac{I_{th}}{P_0} L_{eff}. \tag{1.34}$$

Note that this then means that to avoid mode mixing the maximal achievable spectral broadening is dependent on the input pulse (λ, P_0), on the nonlinear medium (n_0, I_{th}) and the waveguide geometry (L_{eff}). Given a central wavelength, when the peak power of the input pulse goes up (and consequently there's a match from the effective area and the nonlinear index of refraction) the achievable spectral broadening goes down and can only be compensated by increasing the length of the nonlinear interaction. This all leads us to one single scaling law,

$$P_0 \propto \frac{1}{n_2} \propto A_{eff} \propto L_{eff}. \tag{1.35}$$

Hollow Core Fibres

An innovation in propagation was achieved once M. Nisoli and coworkers gave up the single mode approach and decided to go with their new risky idea, using a gas-filled capillary or hollow-core fibre (HCF) [29], instead of the core of fused silica used in the previous single-mode waveguides. This allowed for the nonlinearity to be decreased by thousands due to the gas medium and the mode area could also be increased by a large factor, by the scaling law 1.35.

Unlike optical fibres with a cladding of lower refractive index than the core, a hollow core fibre cannot profit from the total internal reflection of silica fibres. This makes HCFs "low-quality waveguides" that just loosely bind the light to its core, relying on grazing-incidence reflection that makes the fibre inherently lossy and sensitive to bending.

Waves propagating in this structure can have three types of modes [7]: the transverse electric or TE, transverse magnetic or TM, and the hybrid modes or EH. The transverse modes are either pure electric or magnetic fields and so only hybrid modes allow for a quasi-linearly polarised wave. The electric fields of the EH_{nm} modes can be represented by the Bessel function,

$$\vec{E}_{nm} = J_{n-1}\left(\frac{u_{nm}\cdot r}{a}\right)\cdot[cos(m\theta)\cdot\vec{e}_\theta + sin(m\theta)\cdot\vec{e}_r] \tag{1.36}$$

where a is the inner core radius, J_n the n^{th} order of the Bessel function and u_{nm} the m^{th} zero of the n^{th} order of the Bessel function. There's an attenuation constant for the hybrid modes that arise from the intrusion into the dielectric cladding,

$$\alpha_{nm} \propto \left(\frac{u_{nm}}{2\pi}\right)^2\cdot\frac{\lambda^2}{a^3} \tag{1.37}$$

With the proportionality being dependent on the refractive index of the cladding. The transmitted power becomes

$$P(L) = P_0\cdot e^{-2\alpha L} \tag{1.38}$$

The attenuation is quadratic in the mode order n or m, assuming very crudely that the zeros of the Bessel function are linearly spaced. This means that under the correct conditions the higher orders can be attenuated in contrast to the fundamental mode. This can be useful for spatially cleaning the pulse since the lowest order mode very much resembles the Gaussian beam profile.

It is then obvious that we have to couple most of the laser beam into the fundamental mode of the fibre which is only possible if we match the focus of the beam inside at the entrance of the fibre with the fundamental node. Luckily this is possible since the Gaussian beam can be adjusted to be a close match. We need then to calculate the coupling efficiency. Let's consider a Gaussian beam with linear polarisation that is focused centrally on the HCF,

$$E(r,\omega_0) = \sqrt{\frac{2}{\pi}}\cdot\frac{1}{\omega_0}\cdot exp\left(-\frac{r^2}{\omega_0^2}\right) \tag{1.39}$$

[7] The properties of waveguide propagation were described in 1964 by Marcatili and Schmeltzer and can be consulted in [30]

Since the beam is linearly polarised we can only have hybrid modes with EH_{1m}. The absolute field amplitude of those modes is, from 1.36,

$$E_{1m} = \frac{1}{\sqrt{Q_m}} \cdot J_0\left(\frac{u_{1m} \cdot r}{a}\right) \tag{1.40}$$

with $Q_m = \int J_0^2\left(\frac{u_{1m} \cdot r}{a}\right) 2\pi r \mathrm{d}r$. To develop the Gaussian input beam onto eigenstates we have to calculate the inner product for all combinations,

$$c_m = \int E(r, \omega_0) E_{1m} \cdot 2\pi r \, \mathrm{d}r \tag{1.41}$$

We have then the relative optical power inside a given mode $P_m(\omega_0) = [c_m(\omega_0)]^2$.

With all the theoretical background described before we are still left with the fundamental question: what ω_0 optimises the coupling into the fundamental mode? Fortunately for us, this has been studied previously by Frederik Böhle in his PhD thesis concerning post-compression and relativistic plasmas mirrors [6]. Figure 1.9 is from this work and represents the relative energy in the different modes depending on the Gaussian beam size.

$$2\omega_0 = 0.64 \cdot ID \tag{1.42}$$

This is then the optimal beam size where 98% of the coupling is optimised for the fundamental mode, ID is the inner diameter.

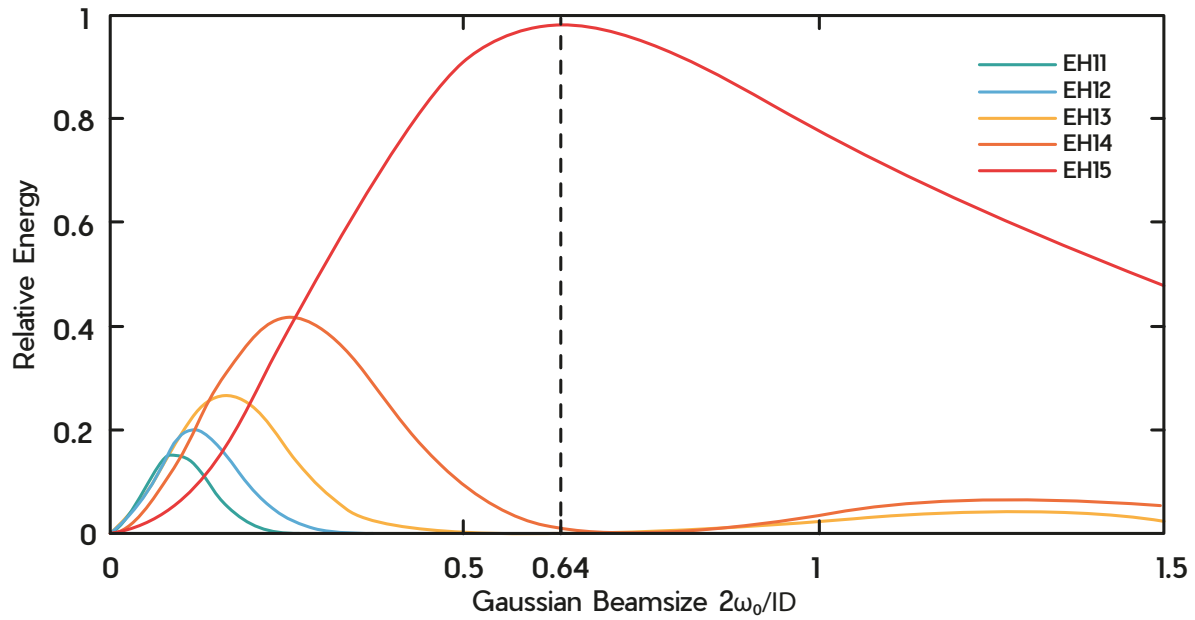

Figure 1.9: Coupling coefficients between the hybrid modes EH_{1m} for a HCF and a Gaussian beam with the mode size of ω_0. From [6]

.

1.3.3 Temporal Compression

Knowing now how we can broaden the original monochromatic beam, it is our final task to look at how we can correct the phase problems we are left with after spectral broadening. For that, we need chirp management, a process that brings all spectral components in phase and makes the spectral phase constant. Most compression setups include a series of chirped mirrors and additional wedges of fused silica that apply continuous tuning of the chirp, such is the case of our project [31]. Once 1.5 or fewer optical cycles are achieved, then there's a need to incorporate additional chirp compensation such as third-order dispersion (TOD) compensation using a combination of bulk materials with different ratios of the group-delay dispersion (GDD) to the TOD [32]. Other techniques exist such as pulse shapers or pulse synthesizers but they are out of the scope of this work. The pulse might also self-compress at certain positions in the course of the nonlinear propagation without extra chirp management [33].

1.4 Resources

Although the theory of post-compression is of extreme interest and importance, a true understanding of single-cycle laser pulses comes only from experimental work done in the laboratories. This thesis uses both the resources of VOXEL, a part of Instituto Superior Técnico as previously mentioned and Salle Noire 2.0 and 3.0 at the *Laboratoire d'Optique Appliquée* (LOA) a part of *Institut Polytechnique de Paris*. Although they have different areas of interest, both facilities mentioned provide ultrashort laser pulses in the orders of a few to dozens of femtoseconds, all with 800 nm of central wavelength. It is then important to characterise the laser pulses.

The laser beams emitted in these stations are understandably hard to caracterize, after all, the only way to measure something in time is by comparing it with a shorter event and ultrashort laser pulses represent some of the fastest man-made phenomena. [8] This makes the field of measuring ultrashort pulses as complex as the field of ultrafast optics. The solution found to measure the pulse duration was, in fact, straightforward, the pulse could only be measured in one way: by comparing it with itself. This concept created then the basis of autocorrelation, the method through which the first ultrashort pulses were measured [34].

1.4.1 Frequency Resolved Optical Gating

Although revolutionary at the time, using the event to measure itself isn't a good enough measurement. It is as short as the event but not shorter. As a result, autocorrelation measures provide a ambiguous measurement of the pulse's intensity over time requiring a known pulse shape. To overcome this limitation, in 1991 Kane and Trebino introduced Frequency Resolved Optical Gating (FROG), a simple spectrally resolved autocorrelation that measures the spectrum vs the delay of a mix of the two pulses [35–39].

[8] Typical measurement diagnostics are done on electronic devices. However, the fastest response in such devices is limited by semiconductor dynamics, in the nanosecond to picosecond regime, which makes it impossible to measure pulses, for example, in the femtosecond region.

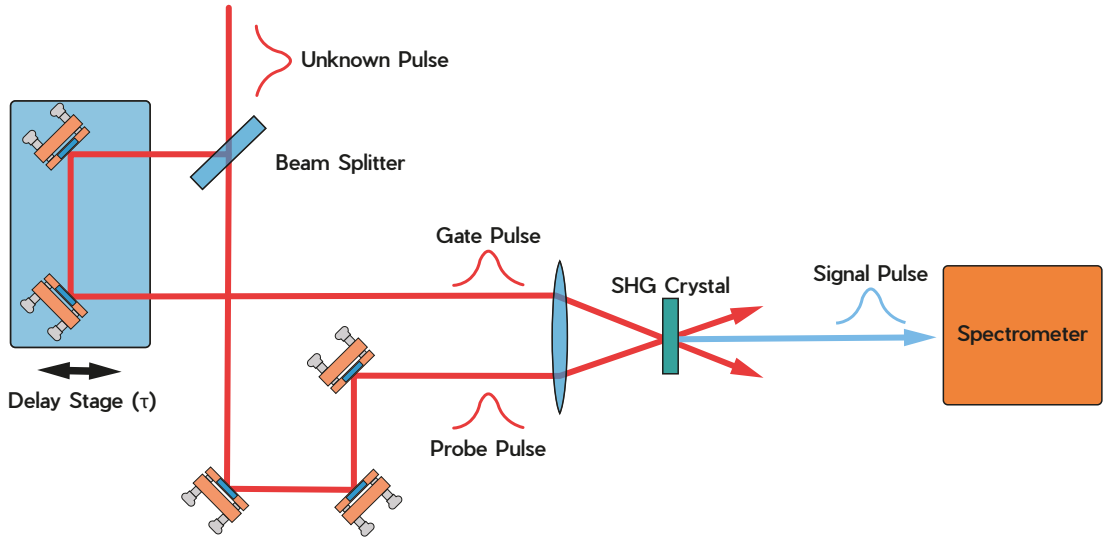

Figure 1.10: Schematic example of an SHG FROG setup. Adapted from [8].

There are several forms of FROG measurements but here we will focus on SHG-FROG, a technique based on a sum-frequency generation nonlinear effect, denominated Second-Harmonic Generation (SHG), deriving from the creation of a doubled frequency beam when two high-intensity fundamental frequency beams overlap in space and time.

The setup is based on the creation of two different beam paths using a beam splitter. One of the beams follows a fixed path length to the nonlinear crystal and the other goes through a path with a delay stage usually controlled by a motor and a manual delay stage. The two beams are focused onto the nonlinear crystal with a lens in a background-free autocorrelation geometry. If phase-matching conditions are met, the second-harmonic signal is created. The generated autocorrelation signal is spectrally resolved with a spectrometer for multiple time delays between the two paths and presented in a 2D contour trace (time delay vs wavelength) as represented in Figure 1.11, denominated FROG trace.

The intensity and spectral phase of the pulse can be retrieved from the FROG trace through an iterative retrieval algorithm. The convergence of any of the available algorithms applied to the FROG trace, to the right signal electrical field, can be achieved with a minimum error by considering the nonlinear effect of the pulse interaction.

The signal field for SHG FROG, i.e., the generated second-harmonic signal can be approximated by

$$E_{sig}(t,\tau) = E(t)E(t-\tau) \tag{1.43}$$

where $E(t)$ is the fixed path replica and $E(t-\tau)$ the delayed replica.

The signal field is spectrally resolved by the spectrometer, which, considering a Fourier-transform spectrometer, produces the Fourier transform of the signal field$E_{sig}(t,\tau)$ with respect to time. The squared magnitude of this signal produces the spectrogram in the following way,

$$I_{FROG}^{SHG} = \left| \int_{-\infty}^{+\infty} E_{sig}(t,\tau) e^{-iwt} dt \right|^2 = \left| \int_{-\infty}^{+\infty} E(t)E(t-\tau) e^{-iwt} dt \right|^2, \tag{1.44}$$

this represents the FROG trace.

After creating the FROG trace, its matrix is retrieved or reconstructed. This requires an algorithm, called FROG code. To quantify the progress of the retrieval, i.e., the convergence of the algorithm, we must further define a measure of the error between exact and derived pulse fields. We define the FROG error in the k-th iteration as

$$G^{(k)} = \sqrt{\frac{1}{N^2}\sum_{i,j=1}^{N}\left|I_{FROG}(\omega_i,\tau_j) - \mu I^{(k)}_{FROG}(\omega_i,\tau_j)\right|^2} \tag{1.45}$$

where μ is a real normalisation constant that minimises the error $G^{(k)}$. $I_{FROG}(\omega_i,\tau_j)$ is the measured FROG trace, $I^{(k)}_{FROG}(\omega_i,\tau_j)$ is the k-th iteration of the retrieved FROG trace.

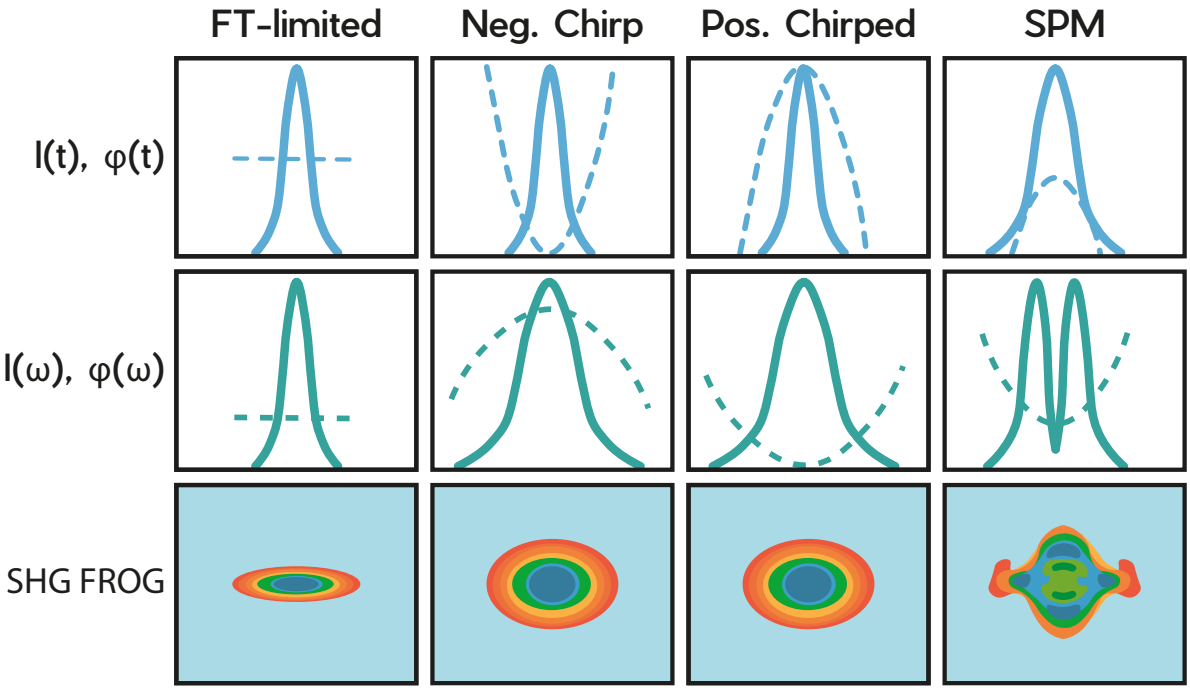

Figure 1.11: SHG FROG traces for typical ultrashort pulses. The top row shows the temporal profile. The middle row shows the spectrum. The bottom row shows the FROG traces. Adapted from [37].

Figure 1.11 shows the full pulse characterisation (temporal profile and spectrum) and SHG-FROG traces for typical ultrashort pulses. The first column corresponds to a FTL pulse which presents a flat spectral phase ($\phi(\omega) = 0$). The second and third column present negatively and positively chirped pulses, respectively and the fourth, pulses after SPM. Notice that in SPM pulses, the high-intensity areas are presented in the borders of the FROG trace as opposed to in the centre.

1.4.2 Multiphoton intrapulse interference phase scan

A much more recent paradigm in pulse characterisation based on phase scanning is the Multiphoton Intrapulse Interference Phase Scan (MIIPS). [40] This method is a fundamental part of the D-Scan

instrument designed to simultaneously compress and measure the pulse which will be described in detail in the following chapter.

It has long been known that nonlinear optical processes are sensitive to the second derivative of the phase. This method takes advantage of exactly that. To start, let us remember the Taylor expansion of the spectral phase $\phi(\omega)$ on the time profile of an ultrashort pulse,

$$\phi(\omega) = \phi_0 + \phi_1(\omega - \omega_0) + \frac{1}{2}\phi_2(\omega - \omega_0)^2 + \frac{1}{6}\phi_3(\omega - \omega_0)^3 + ... \tag{1.46}$$

As before, the zeroth phase ϕ_0 (or absolute phase) determines how the carrier wave is related to the pulse envelope. The first order phase ϕ_1 corresponds to a shift of the envelope in time. These two terms, ϕ_0 and $\phi 1$, are of little interest, the first since it has very little impact on the electric field and the second since it only changes when the pulse arrives, but not its shape. The second and higher orders do have an impact on the time profile of the pulse and so, it becomes clear, that studying $\phi''(\omega)$ gives all the information concerning the pulse shape [41].

MIIPS studies $\phi''(\omega)$ by successively imposing a set of parameterised reference spectral phases $-f(\omega, p)$ to the pulses with unknown phase distortion $\phi(\omega)$ and acquiring the corresponding nonlinear optical spectra. In the second derivative space, the reference functions, $f''(\omega, p)$, work as a grid into which the unknown $\phi''(\omega)$ will be mapped i.e. the points where $f''(\omega, p)$ intersects $\phi''(\omega, p)$ at any desired frequency ω_i,

$$\phi''(\omega_i) = f''(\omega_i, p_{max}). \tag{1.47}$$

For each such point, the reference function cancels the local chirp and the ω_i is maximised, hence the required parameter is labelled as p_{max}.

To understand better this method one has to start with the simplest grid, a series of constant functions $f''(\omega, p) = p$ i.e. linear chirp as is shown in figure 1.12. The different amounts of linear chirp can be added with any passive or adaptive optics and, in the case of the D-Scan, this is done with two wedges of fused silica that add both chirp and TOD. For each of these horizontal lines, a nonlinear optics spectrum is acquired as we see in 1.12b). This is plotted as a two-dimensional contour map in which the height corresponds to the nonlinear optical intensity. If a second-harmonic generation crystal is used as a nonlinear optic, the height would be the intensity of the SHG signal.

The references are unlimited when a adaptive pulse is used and include sinusoidal references such as $f(\omega, \delta) = \alpha sin[\gamma(\omega - \omega_0) - \delta]$, where δ is a parameter scanned across a 4π range [42, 43]. The spectrum can also be plotted as a function of δ. If so, diagonal parallel straight lines separated by π will be obtained for $\delta_{max}(\omega)$ when the pulses are in FTL. Additional group delay dispersion GDD causes a change in the spacing of the curves and third order dispersion (TOD) will change the inclination of the curves [44].

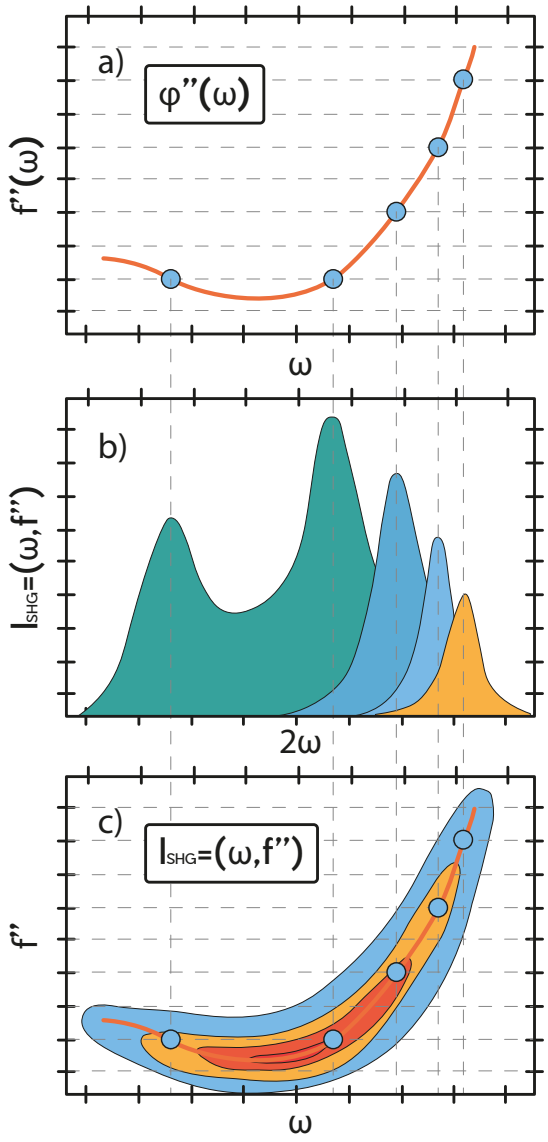

Figure 1.12: Principle of the method. (a) The unknown $\phi''(\omega)$ function is probed using a set of reference linear chirps represented by the horizontal grid. (b) The maximum SHG intensity for every frequency indicates that the corresponding reference chirp value compensates for the unknown function at the position of the maximum. (c) A two-dimensional contour plot mapping the intensity of the SHG as a function of chirp and frequency directly reveals the unknown $\phi''(\omega)$. Adapted from [45]

1.4.3 Working regimes of the resources

Now that we have looked at both techniques, we can conclude that although the Multiphoton Intrapulse Interference Phase Scan method is much more precise, and can be implemented with the simultaneous task of compressing the pulse, it is limited by the size of their wedges which are usually small to guarantee high resolution. The Frequency Resolved Optical Gating method, however, is much more flexible and can be applied in a much broader range of pulse durations, albeit with a much lower resolution. A limitation of the FROG is, of course, the complexity inherent to its setup that even in commercial systems

is not always avoided, while the simpl MIIPS method which is much easier to implement since it doesn't require matching in space and time of two pulses.

For easier understanding, the discussion is summarised in table 1.1 which shows the limitations of each technique and what are the typical regimes of commercial examples. It also shows how an autocorrelator would compare to them.

	Autocorrelator	FROG	MIIPS
Range	$\sim$ 30 fs to $>$ 100 ps	10 fs to $>$ 100 ps	$<$ 10 fs
Resolution	$>$ 1 fs	$>$ 100 as	$>$ 10 as
Alignment	medium	complex	easy

Table 1.1: Comparison between the three pulse diagnostic techniques.

1.5 Summary

To conclude let us summarise all the conclusions from this chapter.

- Isolated Attosecond Pulses are the shortest man-made events and so the VOXEL laboratory is looking to benefit of such a process.
- Creating IAP requires single-cycle laser pulses.
- By the bandwidth theorem $\Delta\omega\Delta t >$ constant, to shorten the duration of a pulse at FTL one needs to first broaden it's spectrum.
- Although there are several ways to broaden an ultrafast pulse, in the VOXEL laboratory we will use a Hollow-Core Fiber. The reason why this is so is described further in chapter 5.
- After spectral broadening the pulse needs to have chirp management in order to bring the pulse back to FTL, this is usually done with wedges and chirped mirrors.
- We presented two diagnostic methods for the temporal domain of the pulse.
  - (i) The first, a Frequency Resolved Optical Gating, will be used for pulses larger than 10 fs, i.e. pulses from the primary laser source;
  - (ii) The second, a Multiphoton Intrapulse Interference Phase Scan, will be used for pulses shorter than 10 fs, i.e. post compressed pulses.

Chapter 2

Post Compression with a Hollow Core Fibre at the VOXEL lab

2.1 Research infrastructure

The VOXEL (**Vo**lumetric medical **X**-ray imaging at **e**xtremely **l**ow dose) project started in June of 2015 and ended in May 2019 as part of Horizon2020. The ultimate goal of VOXEL was to provide an alternative to tomography with a disruptive technology enabling 3D X-ray imaging at very low dose [46–48] and for that, a new laboratory was built in Instituto Superior Técnico. The project ended successfully and GoLP was left with two commercial lasers from Coherent, Inc. [49]:

- Astrella, an Ultrafast Ti:Sapphire Amplifier with integrated Vitara oscillator and Revolution Pump laser with up to 7 mJ of energy, around 35fs of pulse duration and a variable repetition rate from 10-1000Hz,
- Hidra, an High Energy Ti:Sapphire Amplifier seeded by Astrella with 20 mJ of energy, a pulse duration of 45 fs and a repetition rate of 10Hz.

As of the beginning of this thesis work only Astrella was employed in the beam line due to some unalignment inside the Hidra and also some instability of the beam pointing. HHG studies and application studies of those XUV pulses are also still under continuous development. For this, the beam was inserted into an elevator and directed into an attenuator to clean and rotate its polarisation, from here a series of mirrors and a focusing lens focus the beam into the gas cell that creates the high harmonics that are desired. The XUV pulses created are absorved in the air and so a vacuum connection has to be made into a vacuum chamber where interaction occurs.

Several experiments were developed within this setup including a plenoptic camera setup that uses Light Field technology to capture 3D images of objects and a pump and probe setup created to analyse warm dense titanium. This last had to be dismantled in order to implement our new beamline.

A schematic of the VOXEL laboratory before this project is presented in figure 2.1.

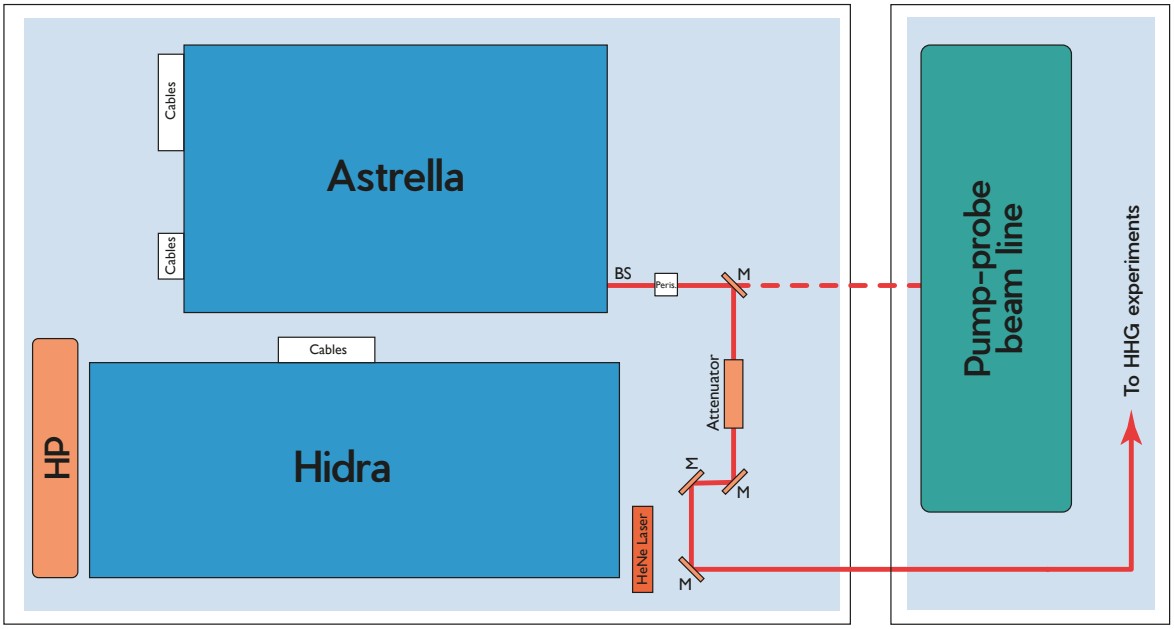

Figure 2.1: Simple schematic of two of the optical tables at the VOXEL laboratory at the start of this project. Also included are the HeNe laser that will be used for alignment and the Hydra pumping system (HP).

2.1.1 Pulse Duration measurements in the 20 -100 fs range

To start the implementation of a post-compression system it's first necessary to analyse the initial conditions with which one is working. Unfortunately, the VOXEL laboratory had no permanent diagnostic tools available and so new devices for this purpose had to be developed and implemented. These tools are of the utmost necessity in a laser laboratory.

There are several quantities that ought to be measured to ensure the proper functioning of a laser, this could be the study of the near and far field, the quality of the M^2 or the quality of the temporal contrast. In VOXEL, we decided to start by analysing the pulse duration and the stability of the beam pointing, this was the case since the industrial grade of the lasers gives confidence in the previously mentioned measurements.

For the pulse duration, we resorted to the Frequency Resolved Optical Gating technique described in chapter 1. Ana Ribeiro had already implemented a FROG diagnostic in VOXEL [50] but this was done in LEGO material that, although cost-effective, was not as stable as required from the complex optic path. There was then a demand to rebuild the diagnostic tool with "normal" optical components.

A laser laboratory is normally a permanently evolving room. With new experiments being constructed over previous ones. The FROG diagnostic needed then to be mobile and easy to implement and so designing on a 25cm by 30cm optical breadboard was the perfect solution, since although mobile it easily becomes part of the main optical table.

According to equation 1.43 we need to divide the beam into two paths: one fixed and one delayed. To start, we took a small portion of the Astrella beam and aligned it with two mirrors in order to fix the

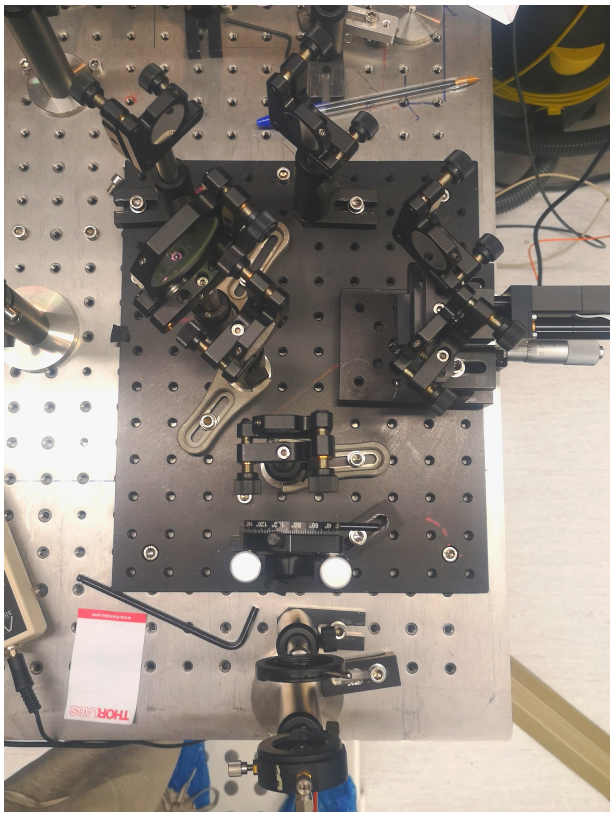

Figure 2.2: Image of the new FROG setup.

entrance of the setup, this is done so that moving the breadboard into new positions requires only a straight beam line. Once a straight line is achieved, a 50/50 beam splitter from Thorlabs is positioned in order to split our beam into two, one through the optical component and the other one reflected with a 90º degree angle as can be seen in 2.4. The reflected beam is aligned by two mirrors into a BK7 lens ($f = 75$ mm). The transmitted beam is likewise directed into two mirrors now supported on a Standa 0.052 μm motorised translation stage. This, is in turn, placed on top of a manual translation stage for initial, more coarse adjustments. After this, the delayed beam is also directed into the BK7 lens. Both the beams are focused into a 1 mm BBO (β-barium borate) crystal that creates a second harmonic signal.

Figure 2.3: Image of experimental second-harmonic generation. The two beams on the side are the original beams and at the center we find the signal resultant from the overlay of the pulses. The center beam is then the one we study.

At this point, we have both beams overlapping in the BBO crystal but we don't yet have them matched in space and time. For this, careful adjustment of the manual translation is necessary. The paths ought to match perfectly in length in order to have the pulse overlap necessary. Once this happens a third second-harmonic signal appears for a length of micrometres in the manual translation stage. This signal can be observed in figure 2.3. We need then to analyse the SHG signal, for this, the beam is directed through a small lens that is coupled with an optical fibre that conducts the signal into a spectrometer (Ocean Optics Modular USB spectrometer 2000+) that spectrally resolves it.

This setup is described in figure 2.4.

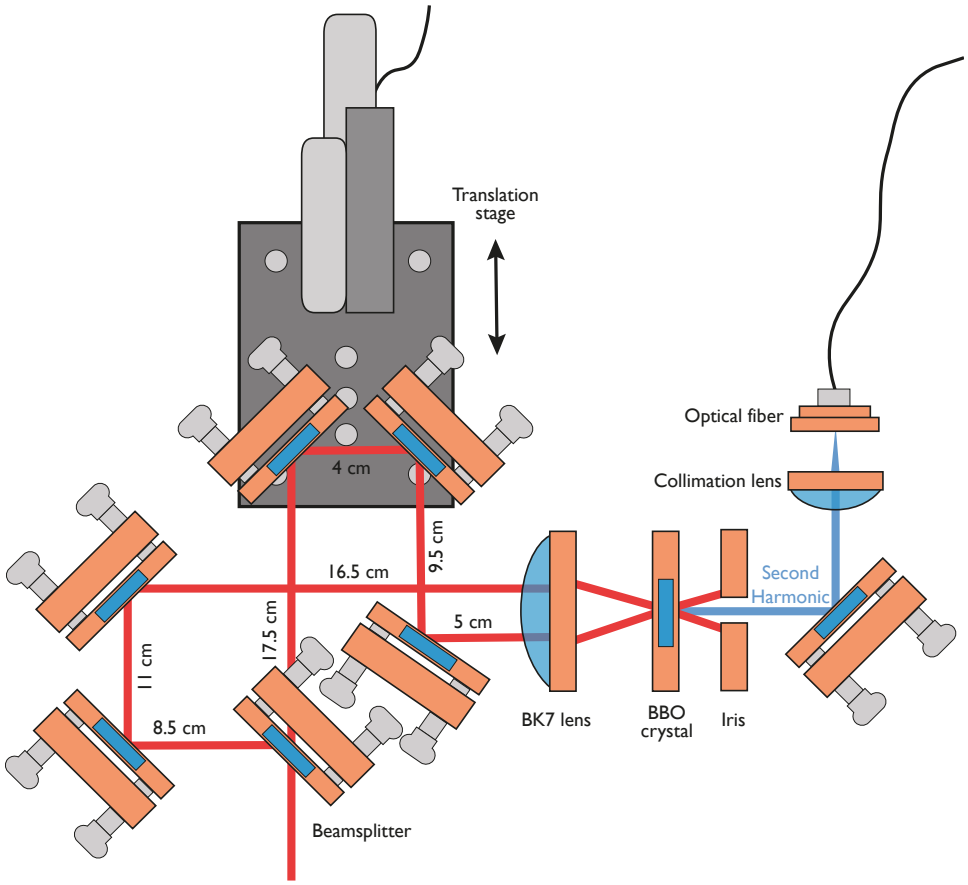

Figure 2.4: Experimental arrangement for compact SHG FROG: The input beam is split into two with a beam splitter. Both beams are focused onto a BBO crystal with a BK7 lens. The generated SHG signal is collimated onto an optical fibre

To create the FROG trace described in equation 1.44 one has to retrieve an SHG spectrum for each time delay step. This needs to be automated and so a LabVIEW program was implemented that simultaneously controls the motor of the delay stage and retrieves data from the spectrometer. Every time the motorised translation stage is made to move, it goes through a fixed step of $0.052\ \mu$m, adding then $0.104\ \mu$m to the length of the path. This corresponds to a minimum temporal resolution of 0.346 fs, suitable for existing laser pulse sources at the VOXEL laboratory. The algorithm of the software *LabVIEW* delivers then a two-dimensional matrix where, for each time delay, the intensity of the spectrum is plotted. Some of these traces are presented in figure 2.5 for several delays of the Pockels cells [1].

[1] A Pockels cell is a device consisting of an electro-optic crystal (with some electrodes attached to it) through which a light beam

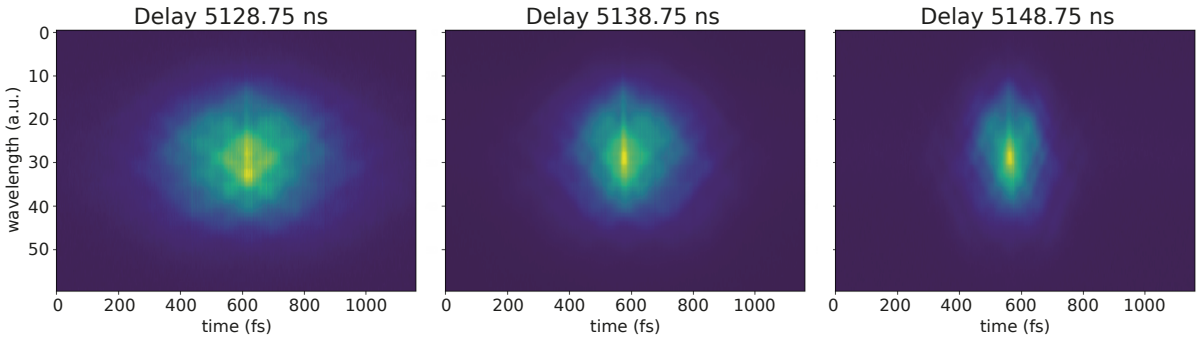

Figure 2.5: Evolution of the FROG trace through several delays of the Pockels cells.

After creating the matrix, we need to calculate the temporal and spectral profile represented by the trace. This is done via free FROG software from the defunct company FemtoSoft Technologies, LLC. The software works by applying different retrieval algorithms to the trace: the basic algorithm, the generalised projections algorithm and different over-corrections and minimisation techniques for multiple iterations. This is done while displaying the FROG error between measured and retrieved traces [38]. To start this retrieval one has only to clean up the noise of the raw data beforehand, being careful to not delete necessary information, this is done in the software itself. An example of the raw and retrieved trace is presented in figure 2.6.

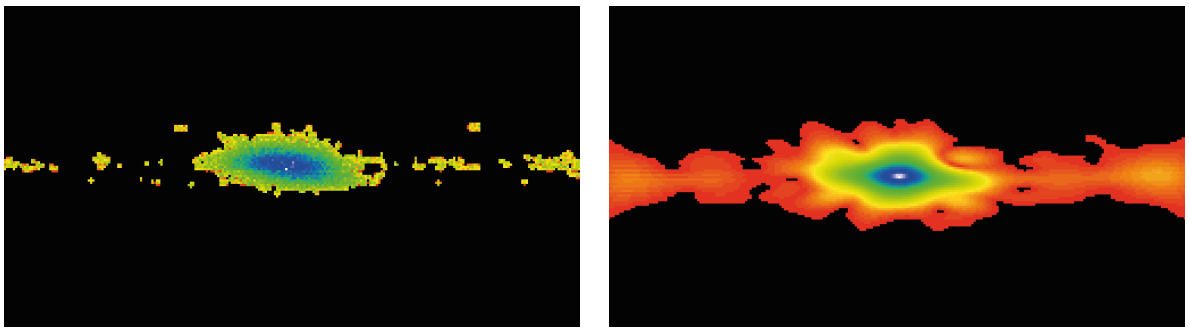

Figure 2.6: Raw (on the left) and corresponding retrieved FROG trace (on the right).

Several measurements were made with a variation of the delays of the pockels cells and of inner compression of the laser. Unfortunately, the Astrella has a compressor without an encoder and so a proper study was not possible. The shortest pulse duration found was 39.4 fs and the profiles corresponding to that duration are plotted in figure 2.7.

At the end of this measurements we went over the damage energy threshold of the BBO crystal making it unusable as can be seen in figure 2.8. Further improvements of the FROG setup were then impossible until a new crystal arrived, which took several months. Practicality meant then that this realignment had to be done only after the conclusion of this thesis.

To verify the measurements taken, we had the opportunity of analysing our beam with a D-Shot, a professional single-shot measurement tool by Sphere Ultrafast Photonics [51], a Portuguese company we will revisit further in this chapter. The D-shot R system used has a spectral range of $700 - 900$nm

can propagate. The phase delay in the crystal can be modulated by applying a variable electric voltage. The Pockels cell thus acts as a voltage-controlled waveplate.

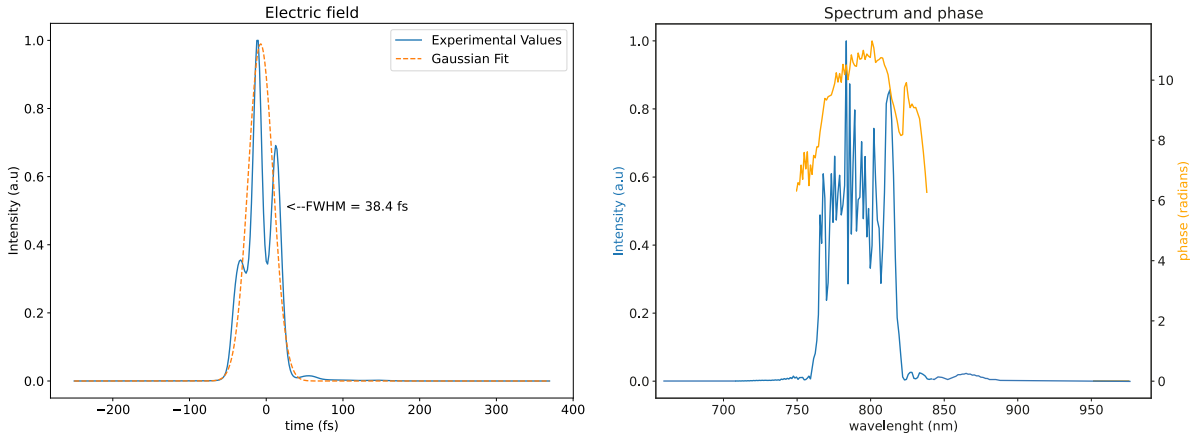

Figure 2.7: Pulse's temporal intensity and its Gaussian fit (on the left) and corresponding spectrum and spectral phase (on the right).

with an available FTL pulse duration from 10fs to 45fs being then perfect to analyse the Astrella beam.

This study revealed that the laser has a bandwidth supporting 38 fs and we were able to compress these pulses down to 43 fs. This was done much after the FROG measurements and in a very short time so its results were not expected to match perfectly. This might also be due to the current state of the Astrella.

Figure 2.8: Second Harmonic signal through the damaged BBO.

2.1.2 Beam Pointing Study

Let's now look at how the pointing of the Astrella acts on the entrance of the fibre we are implementing on the VOXEL laboratory. For this, a leak from a mirror after the focusing lens used for the coupling is directed into a CinCam CMOS-1201 beam profiler by CINOGY Technologies GmbH with the beam size necessary to properly couple into the fibre as discussed in the previous chapter.

Several one-hour measurements were made but it was revealed that such a short interval made the results inconclusive. To correct this, a seven-hour measurement was performed after the laser was warmed up. The results are shown in figures 2.9 and 2.10 where the deviation from the mean position in the vertical and horizontal directions is plotted. It is then obvious that there's a much stronger drift in

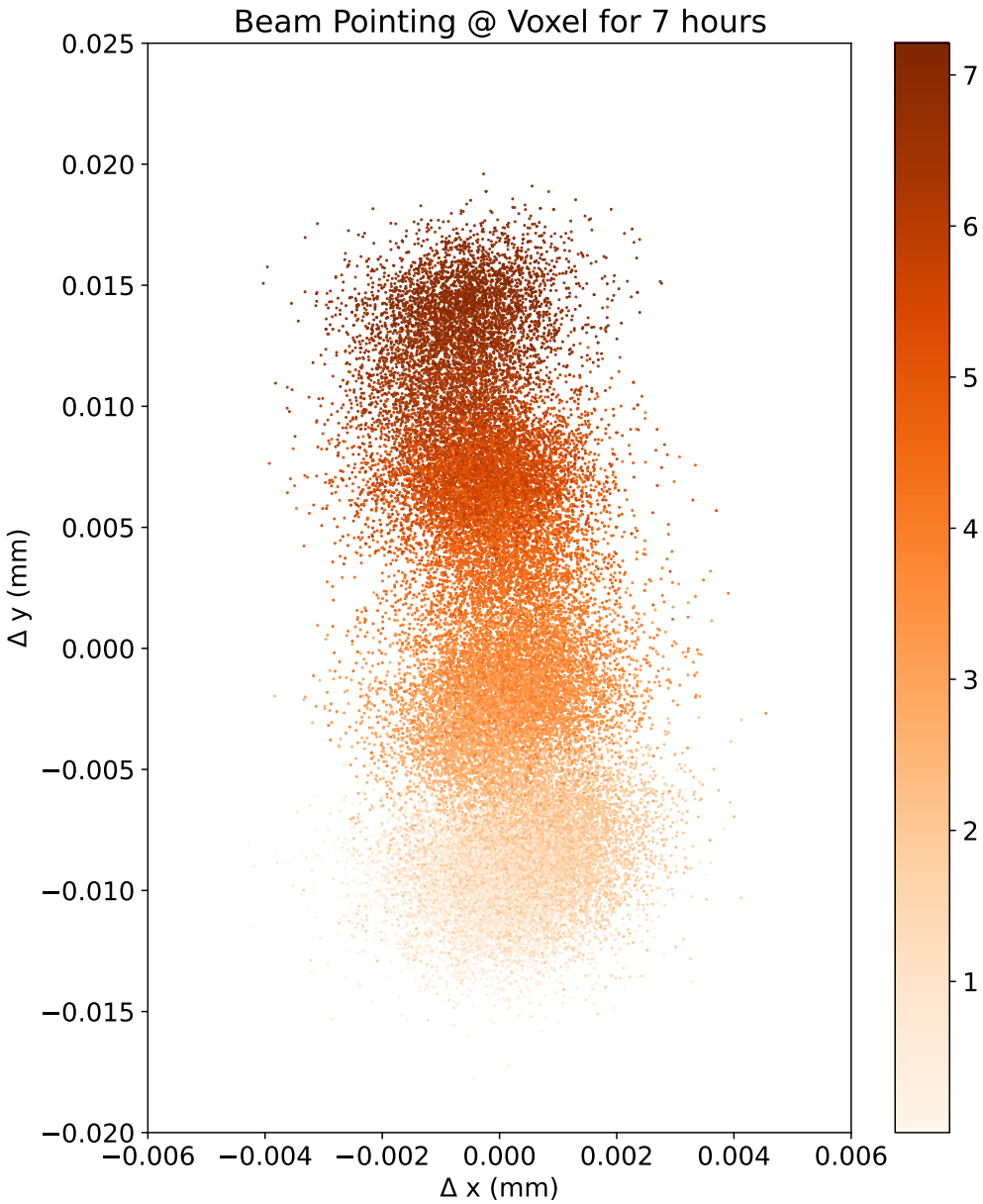

Figure 2.9: Horizontal and vertical deviation of the beam centre measured with the beam profiler for over 7 hours. Note the axis scale.

the vertical direction than in the horizontal one. This could have several origins but the most probable is the rising temperature from the back of the laser. This will be studied further within the next months.

During this study, an interesting observation was made during an attempt at a 24-hour measurement, a beam block was re-positioned during the measurement to improve laser safety overnight. When it was placed on the optical table, a sharp jump in the beam position was observed. This effect was easily reproduced. The sharp jump is most likely due to vibrations, which can be reduced by correctly fastening the used optics. After fastening, the jumps reduced but did not entirely disappear. Thus, it is advised in future experiments to place objects on the optical table as gently as possible to reduce vibrations. Additionally, it is recommended to use different beam blocks with less strong magnets. For this, there's the need to thank another colleague, Luc Verwaal, who was so kind to analyse these measurements.

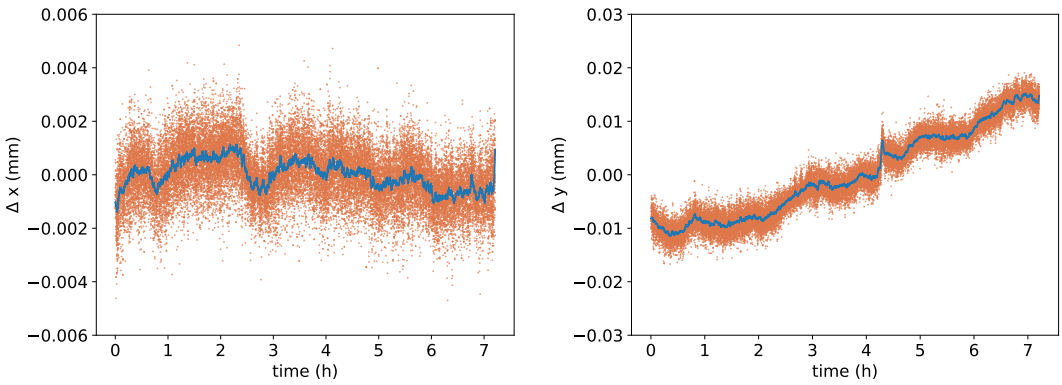

Figure 2.10: Horizontal and vertical deviation of beam centre plotted against time. A moving average is also plotted to better interpret the data. Note the vertical scale.

The report from his time at the VOXEL lab can be found in [52].

This level of instability is rather problematic for the coupling. With a continuous drift in the vertical direction, hour-long operations of few-cycle beams become impossible without constant re-alignment. It also causes permanent damage to the fibre since the beam starts depositing energy into the cladding and not the hollow core itself. There is, in any case, a solution, to counteract this motion one only needs two piezo motors and two quadrant photodiodes. The sensor could detect any pointing fluctuations and give feedback to an active piezo mirror that opposes the lack of stabilisation. This setup is under development by Mohammed Merkache, the third of the wonderful interns that helped us in this study. An Active Beam Stabilisation system by TEM Messtechnik GmbH is also under commission and should be implemented in the VOXEL laboratory within a few months. With a stable beam, a new door of applications of few-cycle laser pulses could open up.

2.2 Broadening

The installation of the Hollow-Core Fiber was not a trivial task. The Hollow-Core Fibre is not only extremely sensitive to bending and torsion but is also very easily damaged by pointing fluctuations at the entrance of the fibre, as will be shown in a few paragraphs. For this reason, careful planning and installation of the waveguide were necessary.

Right at the start of planning the installation of the HCF setup an unfortunate fact made itself clear, the two laser systems placed at the main optical table did not permit enough space for the planned beamline, it was then necessary to move both the Hydra and the Astrella in order to free up space. Not only are laser systems inherently unstable but also are the optical tables where they rest. Moving two objects of such weight in the optical table created instabilities and oscillations that did not permit immediate work. Instead, the laboratory had to be shut down for several days until the new equilibrium point of the optical table was achieved. After, we also needed to re-align the laser itself since it had been misaligned during all this movement.

Having now enough space, the installation could finally commence. The first step was then to rethink

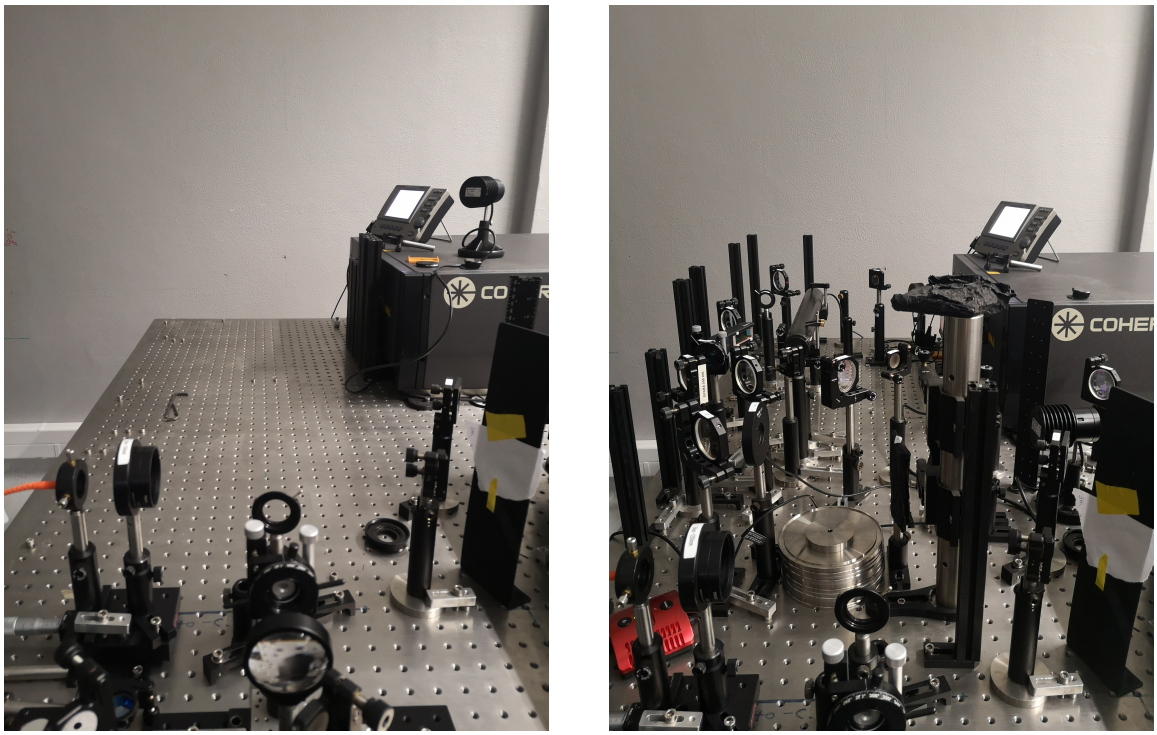

Figure 2.11: Installation of the HCF (before and after adding the new beamline).

the previous beamline that directed the beam only to the HHG experiments. For this, a beamsplitter had already been purchased, allowing us to have both the new and old beamline working simultaneously, however, a new problem appeared in the meanwhile: our laser was no longer able to reach the 8mJ promised by the manufacturer and the energy emitted could no longer allow concurrent experiments. After some re-planning, we concluded that the new beamline should be created using a flip mirror to change whether the beam follows the original beamline or the new one.

The entire spectral broadening system includes not only the fibre but also the whole support structure and the gas and vacuum control station. Although the Hollow-Core Fiber came with an instruction manual, we found the installation steps deficient. For future installations, a detailed description of the alignement process as well as the entire characterisation of the gas system are present in appendix A.

The new beamline was created after the attenuator present in figure 2.1. The attenuator is used since it cleans and rotates our polarisation, this, however, required that we place an waveplate after, to allow us the fine tune of the input polarisation of the fibre. The beam was then directed through a long path between the laser systems, into an achromatic lens ($f = 750$ mm) that allowed the coupling of the beam into the fibre.

We then started the implementation of the fibre system. This included the alignement of the support system with a visible laser, the placement of the gas system, the alignement of the Brewster windows and, of course, the placement of the fibre. The system was also tested in three different modes: evacuation, fill and differential pumping (again, described in appendix A). Finally, to ensure the proper coupling and to study any deviations of the beam pointing, we installed a beam profiler at exactly the same distance from the lens as the input of the fibre.

The whole spectral broadening system is schematised in figure 2.12.

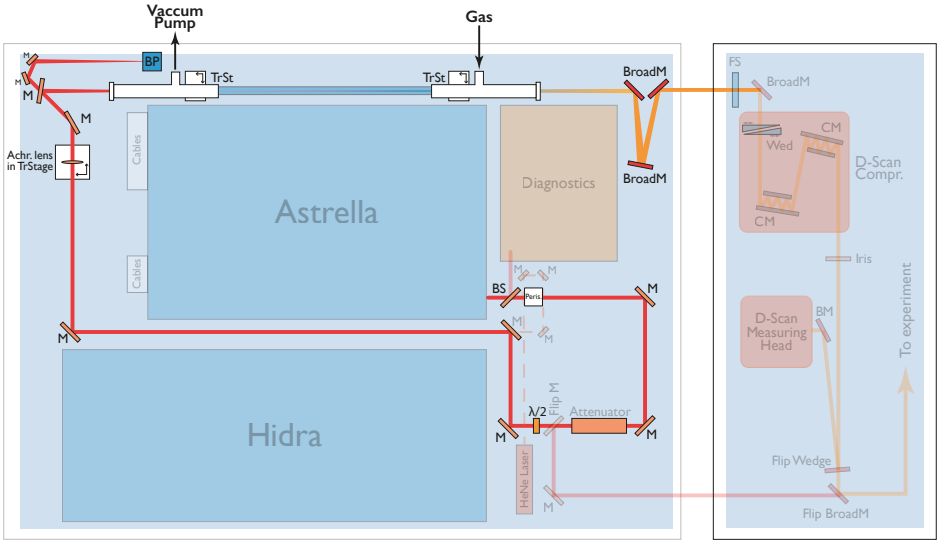

Figure 2.12: Scheme of the setup of the HCF in the VOXEL lab.

2.2.1 Optimisation of the Spectral Broadening system

Once we followed these new steps, we could finally start to couple the NIR beam into the fibre. Ideally, all the preparation that went into finding the focal spot and the overall correct alignment should have allowed for easy coupling of the fundamental mode, that, however, very rarely happens. The core diameter is much smaller than any natural oscillation that might occur at any point of the installation and so some fine-tuning is almost always necessary. Remember, the beam pointing is also subpar, as concluded by our studies, which might also be a big factor in this optimisation issue.

Ensuring proper propagation throughout the waveguide is a long process, any change in the vertical and horizontal direction of the focal plane needs to also be corrected at the output side to secure the parallel line necessary for propagation in the waveguide. This was done with both a camera and a beam profiler that checked the shape of the modes transmitted, a Power Meter was also used to measure where the transmission percentage was at its highest. This first was done in evacuation mode to avoid any undesired ionisation and damage before proper coupling.

Once a reasonable transmission was achieved, we went into the static fill mode just described before. Unfortunately, due to the original dispersion in our beam, we weren't able to see spectral broadening instantly. Only by changing the compressor inside the Astrella could we finally achieve the right amount of dispersion at the entrance point of the fibre. With these changes in pulse duration, we finally saw some spectral broadening occurring in the form of a red circle of light. Finally, we had moved to a more fortunate state: the new frequencies moved our spectrum to the visible range and we could now see the hybrid modes themselves. While here we were still just seeing red, increasing the gas pressure would boost the B-integral and more colours would appear. A larger pressure gradient leads us then to the white light seen in figure 2.13 b). Besides it, we have a more colourful figure, this picture is of special

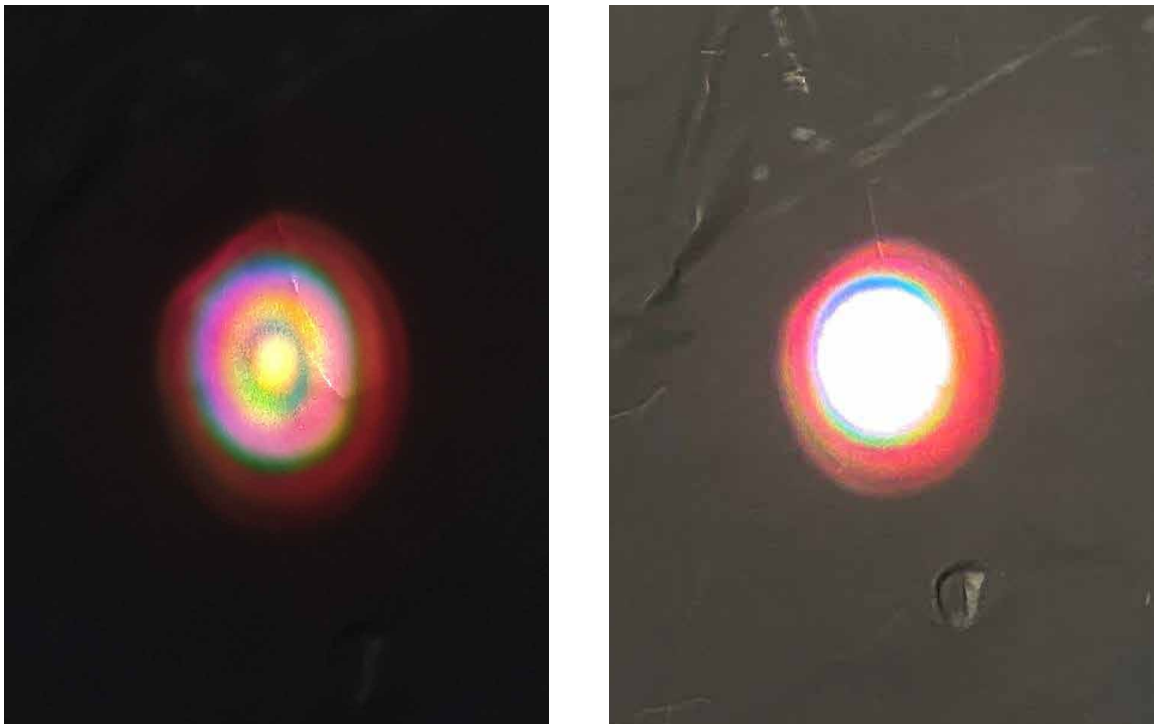

Figure 2.13: Picture of the ”rainbow” created through the optimisation of the fibre.

importance to our group since it represents the first broadband pulse in our laboratory. It is important here to remind ourselves that all this occurred while the fibre was constantly under realignment.

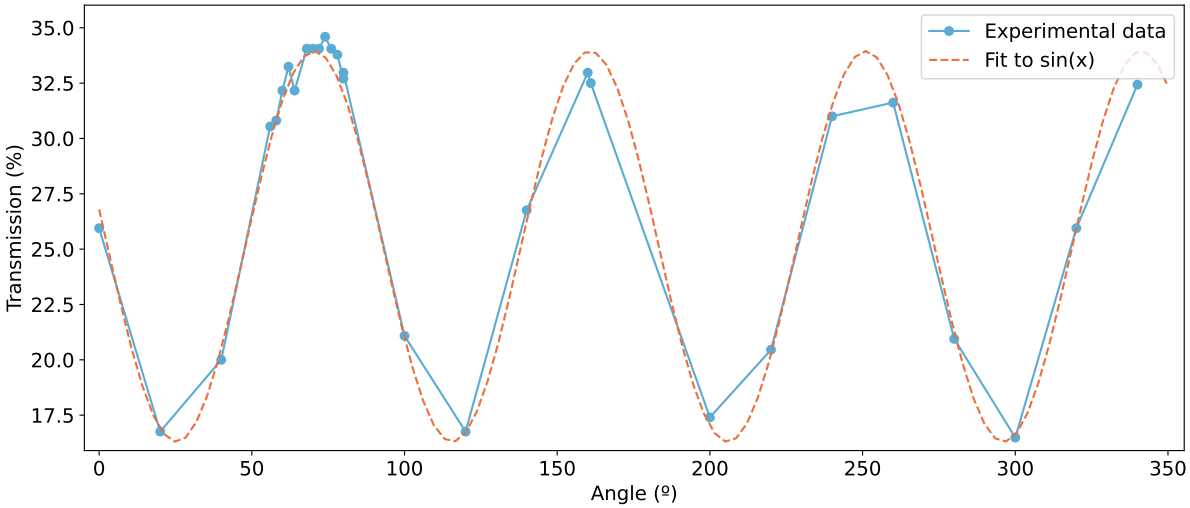

Figure 2.14: Energy Transmission in function of the $\lambda/2$ waveplate angle.

At this moment, we finally knew how to achieve broadband pulses but our transmission rate was still weak. To correct this, we looked further into the polarisation of the input since this was the only variable we could update (the beam pointing didn't allow for the proper improvement of the coupling of the fibre). First, we tried to align horizontally the line in the Brewster windows that indicates the polarisation that crosses the optical component. And then, believing this was correct, we rotated the waveplate into the angle with the biggest transmission rate. A study of how these two quantities are related is shown in

figure 2.14 and confirms that changing the angle of our waveplate even for just 5 degrees might imply a fall in the transmission of 3%. This will be extremely important once we pass to our next phase.

2.3 Compression

Once the spectrum is broadened, we could finally arrive at the installation of the last part of our setup. Due to the quasi-octave spanning spectral range, new optics had to be used, instead of the narrowband dielectric or metallic mirrors used in the laboratory. After the fibre we used, then, Femtosecond Optimized Silver Mirrors from Newport Corporation with $R > 99\%$ from 600-1000nm with near zero GDD over extended bandwidth. To correct the divergence of the beam after the waveguide we took advantage also of a broadband concave mirror with $f = 75$cm.

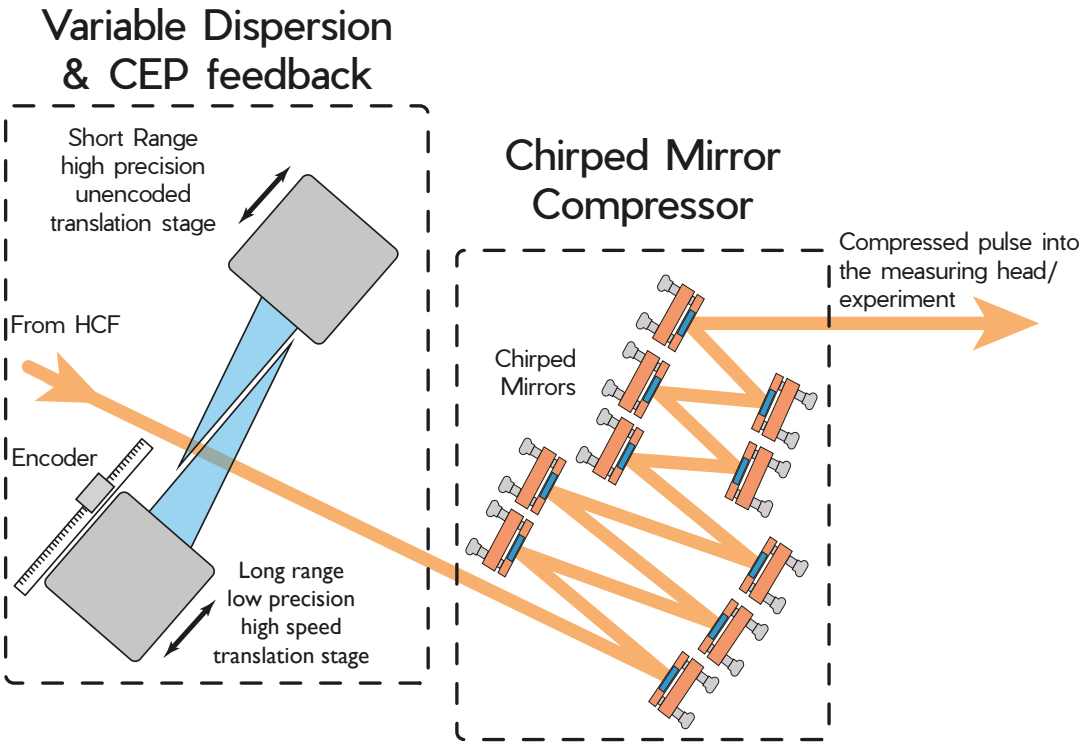

Figure 2.15: Schematic of the d-scan setup. Adapted from [53]

Once the beam is recollimated, we redirected it into the D-Scan system [53–55]. The d-scan technique is a novel method for the measurement and compression of ultrashort pulses that doesn't rely on spectral shearing nor on spectrally resolved autocorrelation. It relies instead on the manipulation of the spectral phase of a single pulse under test. This is done using a pulse compressor and the subsequent measurement of the spectrum arising from the interaction of the beam with a medium with an optical nonlinearity i.e. using the MIIPS method described in chapter 1. This system is composed of a pair of wedges, to give continuous dispersion, a series of chirped mirrors and a measuring head, connected with the translation stages of the wedges as demonstrated in figure 2.15. The D-Scan present in the VOXEL laboratory was set up in air in a different optical table than the HCF system but has vacuum compatibility for future experiments.

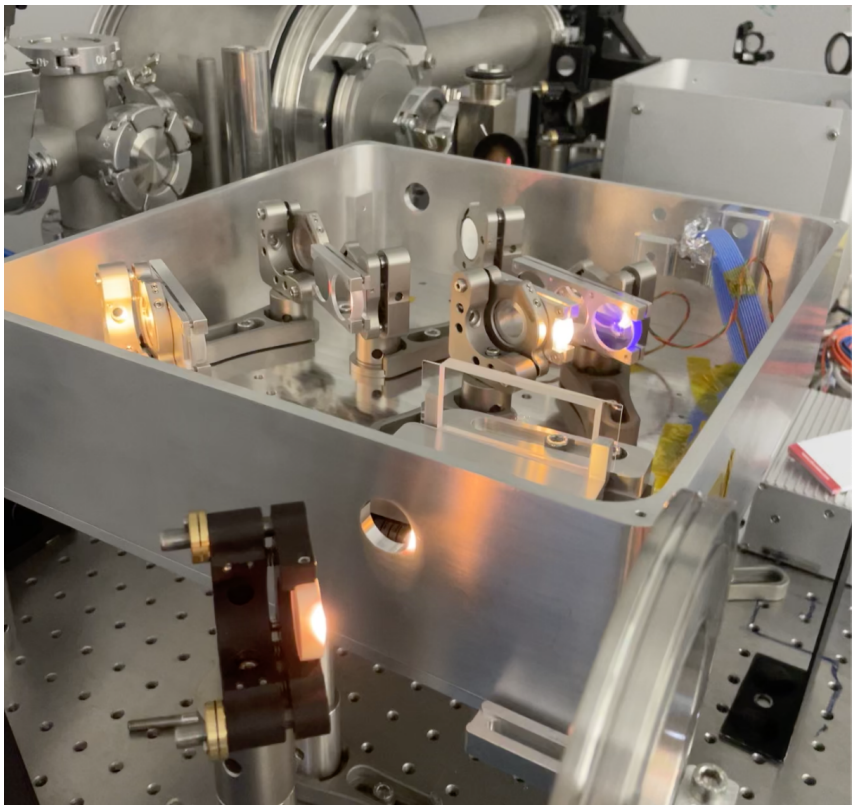

Figure 2.16: Photography of the D-Scan when the broadened pulse is propagating through the compression section.

The installation was rather easy, mostly due to the help of Rosa Romero and Paulo T. Guerreiro from Sphere Ultrafast Photonics. The compressor part of the D-Scan implies only that the input beam was parallel to the plane of entrance of the D-Scan and that the chirped mirrors had two bounces out of each mirror (this can be changed to just one bounce per mirror in case less dispersion needs to be added). This can be seen in 2.16. After, we used a wedge to sample the beam into the SHG measuring head, where a type-I BBO crystal is used to create the nonlinear effect needed and two spectrometers resolve both the fundamental and the second-harmonic spectrum. This is all retrieved in the company-made software.

At first, alignment of the beam into the measuring head was needed but, after a while, a signal was detected in the D-Scan trace. An image from the software is shown in figure 2.17. This slight extension of the red zone into 350nm gives a hint of the D-Scan trace desired, it is, however, obscured by the signal from the fundamental spectrum. This occurs when the polarisation going into the measuring head is not exactly P-polarised. This was solved by rotating the waveplate before the HCF in order to achieve a cleaner signal shown in figure 2.18. It would, of course, make more sense to include a waveplate after the fibre but we didn't have any broadband $\lambda/2$ available and a search for one has taken longer than expected. Once we had the signal, we needed also to include a fused silica window of 3 mm before the D-Scan to decrease the amount of dispersion necessary into the D-Scan range, and so lower the trace vertically in the SHG D-Scan trace.

Although the installation was easy, the optimisation was not. Several variables needed to be con-

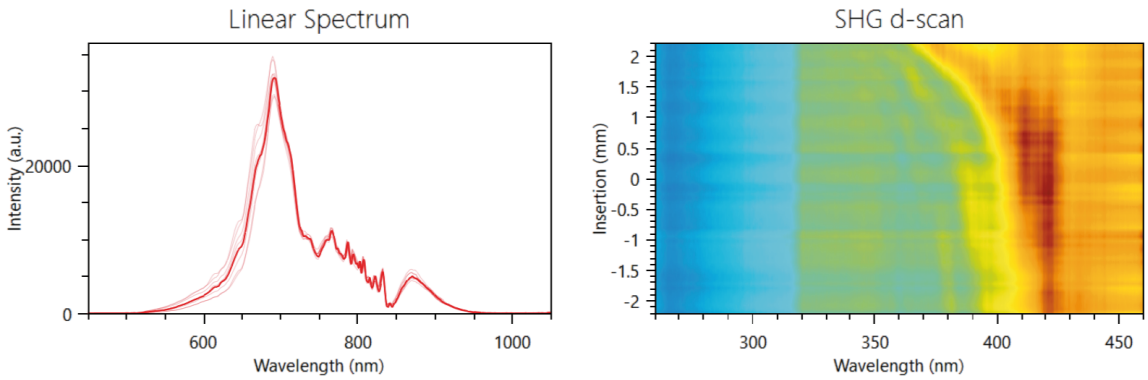

Figure 2.17: Linear spectrum of the post-compressed pulse (left) and its SHG d-scan trace (right) when a signal started appearing.

sidered and tweaked while also managing the failing beam pointing. An adjustment of the Brewster windows in the input and output tubes was also needed to correct the polarisation and increase the efficiency while also achieving a clear SHG signal. Lastly, the amount of dispersion added by the compression system in the Astrella also had to be adjusted since the input phase also determines the amount of broadening that emerges.

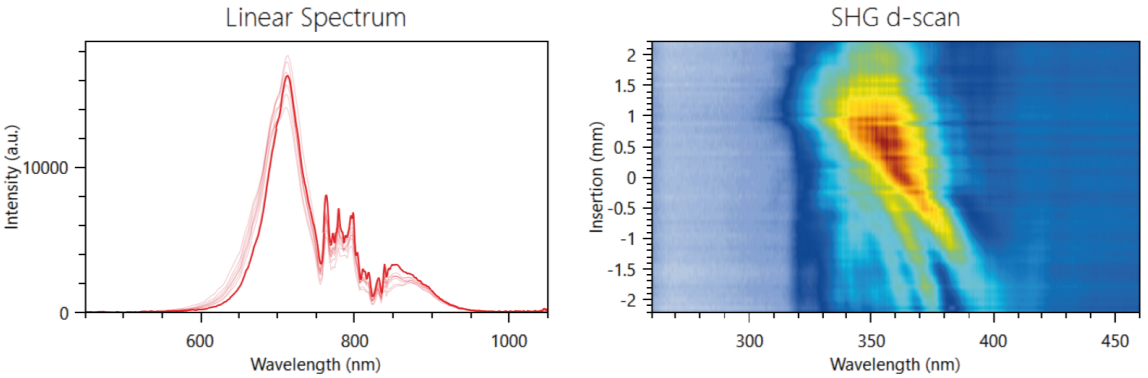

Figure 2.18: Linear spectrum of the post-compressed pulse (left) and its SHG d-scan trace (right) with a change in polarisation.

A schematic of this section of the post-compression system is present in figure 2.19. More recently, adjustments have been made to the system to allow for HHG with broadband pulses but unfortunately, there was no time to continue with the experiment.

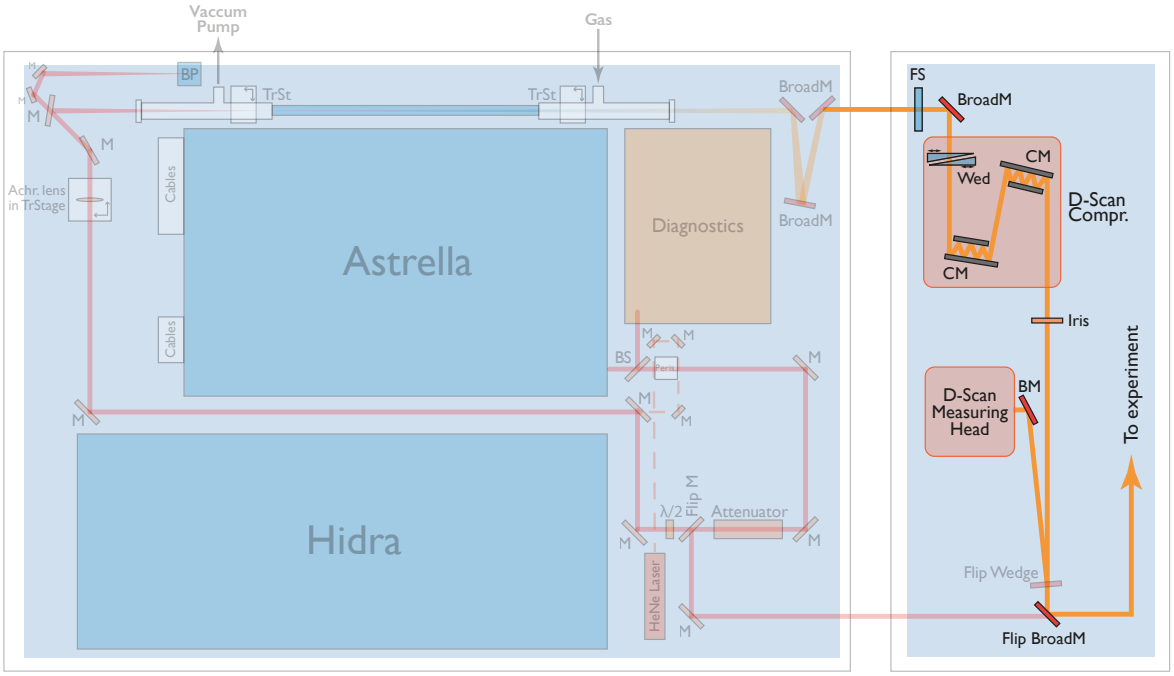

Figure 2.19: Scheme of the setup of the D-Scan in the VOXEL lab.

2.4 Results

The gas pressure defines how much broadening happens and so a study was done in order to analyse the amount of broadening for each pressure of Argon ($n_2 = 10.8 \times 10^{-20} \text{cm}^2/\text{W}$ at atmospheric pressure [56]).

The broadening started to occur with a pressure of 0.6bar and increased until 1.8bar where the system set a hard limit of input pressure. This analysis was done with differential pumping to protect the fibre from the creation of plasma at the entrance of the fibre, especially since the beam was constantly drifting and depositing energy in the cladding. Once the beam is stabilised further studies can be conducted. The evolution of the spectrum is represented in figure 2.20. There was also an attempt to do this study with Helium ($n_2 = 0.3 \times 10^{-20} \text{cm}^2/\text{W}$ at atmospheric pressure) and Neon ($n_2 = 1 \times 10^{-20} \text{cm}^2/\text{W}$ at atmospheric pressure) but the first needed metal tubes to prevent leaks due to the small size of the atom and the second is out of reach due to the current worldwide shortage.

Some interesting observations can be made from this study, in particular, the unsymmetrical nature of the broadening and the presence of self-steeping most notorious when the pressure increases to 1.6-1.8 bar, a consequence of the same phenomena: the peak of the pulse will propagate slightly slower than its flanks, as described in chapter 1. For this reason, we focused our D-Scan measurements around the pressure of 1.2 bar, where we find a broad enough spectrum to achieve single-cycle FTL but safety from effects of self-steepening and the possible collapse of the pulse [57].

The spectra here has to be observed with some care. Due to a miscalibration of the Flex Spectrometer from Sarspec and a different sensitivity to different spectral lines, the intensity profile of the above spectra is different from reality. We can then visualise the evolution of the bandwidth with the knowledge

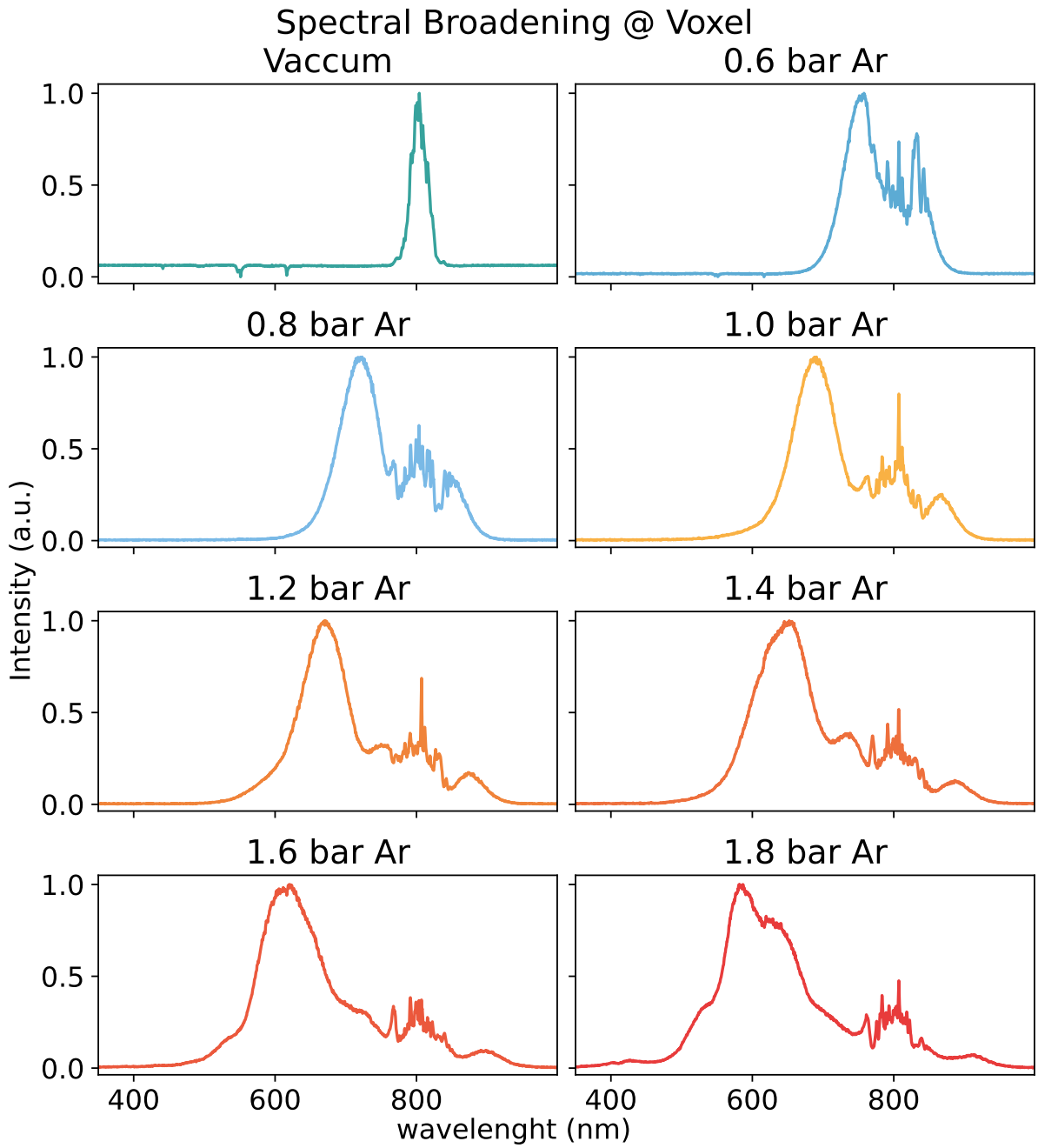

Figure 2.20: Evolution of the normalised spectral shapes with increasing gas pressure in the HCF of the VOXEL lab.

that the intensity of each wavelength does not correspond to a real value. There was also some instability in the intensity of the spectra during measurement due to the lack of stability in the beam pointing and hence the coupling of the correct mode.

This is the reason why the two spectra in figure 2.21 differ so much even though there taken seconds apart under the same conditions. Due to this attenuation on the red part of the spectrum, there's no proper way to calculate the RMS of the spectral width and hence the corresponding FTL. This will be done in the next chapters to properly understand how the evolution of broadening corresponds to a shorter FTL.

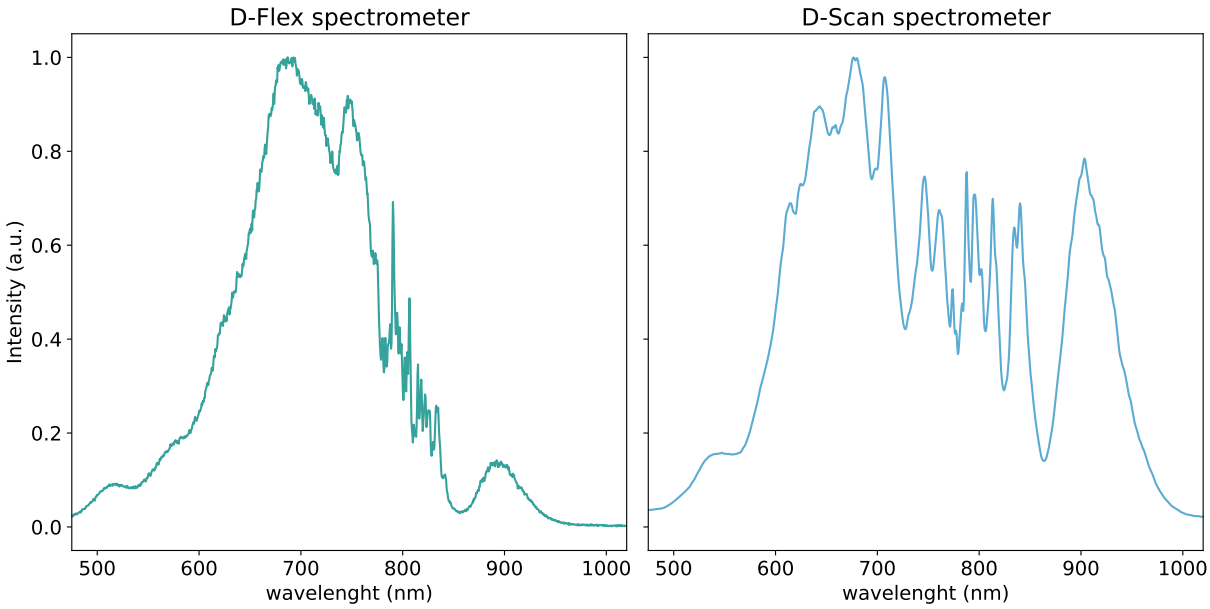

Figure 2.21: Normalised spectral profile of the beam post-HCF with 1.2 bars of Argon and differential pumping in a Flex Spectrometer from Sarspec (left) and in the D-Scan spectrometer.

The spectrum in figure 2.21 is also responsible for the shortest pulse duration achieved during this thesis. With a time-limited pulse width of 3.24fs, we managed to achieve a pulse width of **3.81fs** (less than 1.5 optical cycles for 800nm where one optical cycle corresponds to 2.7fs) with an RMS error of 2.1% given by the D-Scan software based on MIIPS. In this particular measurement, an input of $E_{in} = 797\mu$J was placed into the fibre and transmission of only 27% was achieved. This was improved later, and values of transmission of almost 40% were sometimes measured. Unfortunately, due to time constraints and the equipment constraints already mentioned, a proper study and optimisation of this transmission were not possible, there is however a lot of potential for improvement, and this is to be done in a couple of months.

A quick look into figure 2.22 reveals a thin but obviously tilted D-Scan trace, corresponding then to a low GDD but an intense TOD. This unfortunately cannot be solved at VOXEL, only a material with proper GDD/TOD ratio or with only TOD compensation can correct this. Sphere Ultrafast Photonics has done some studies on our initial results showing that with a proper passive dispersion compensation optical component (DCO) our TOD can be corrected at ease. Only with this correction will we be able to achieve FTL pulses.

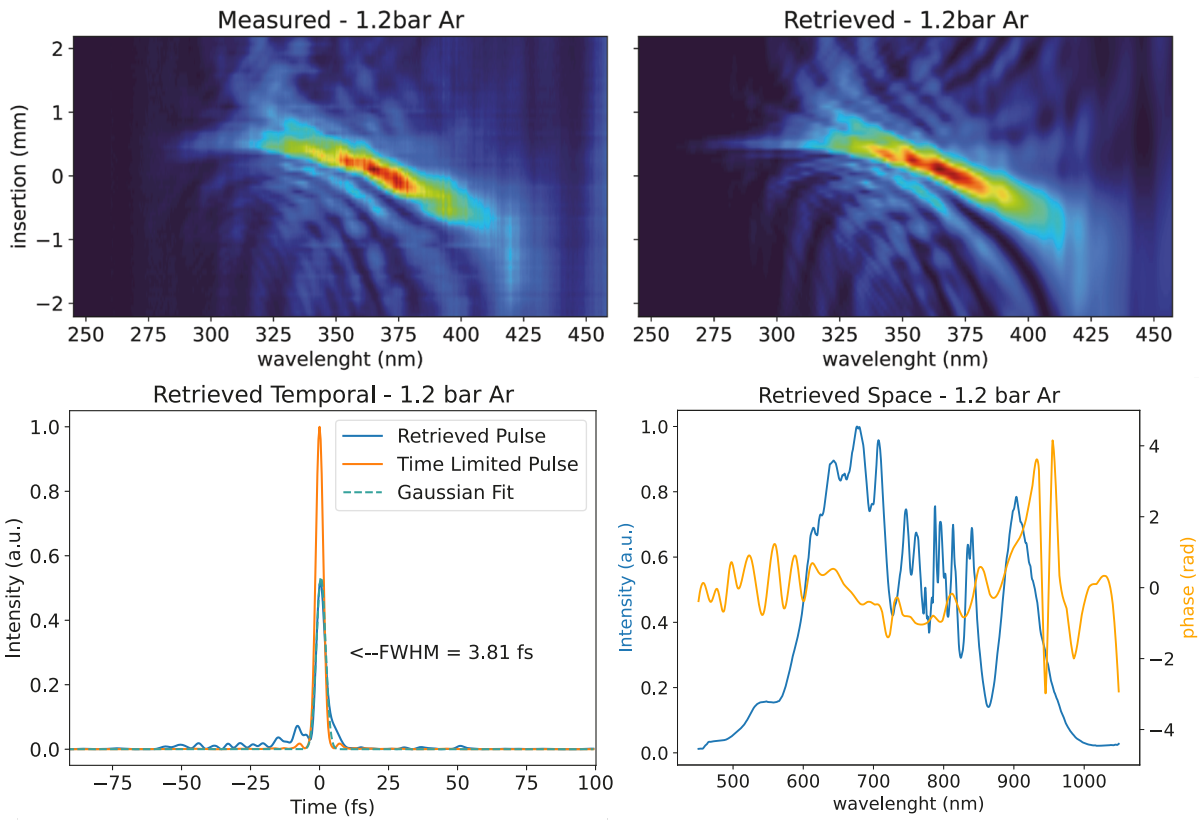

Figure 2.22: Measured (top left) and Retrieved (top right) D-Scan trace of the optimal HCF broadening in the VOXEL lab with 1.2 bar of Argon, $E_{in} = 797\mu$J and transmission of 27%. Along with the corresponding temporal (bottom left) and spatial (bottom right) retrievals.

2.5 Summary and Conclusions

- We have achieved pulses of less than 4 fs, i.e. 1.5 optical cycles in the VOXEL lab;
- At the end of this thesis we have 33% of transmission along the fibre but this can be optimised to up to 50 % with some new resources;
- After analysing the pulse's characteristics, we concluded that the pointing drift might be the main reason why the coupling is not more efficient;
- To correct the beam pointing, a beam stabilisation system has already been commissioned;
- Even without the corrections, we are now ready to create broadband harmonics and a new broadband beamline has been created.

Chapter 3

Post Compression with a Hollow Core Fibre at the Laboratoire d'Optique Appliquée

3.1 Research infrastructure

To better understand the HCF method of post-compression, we had the privilege of collaborating with colleagues from the *Laboratoire d'Optique Appliquée* (LOA) a part of *Institut Polytechnique de Paris*. More specifically, we collaborated with the Optical-Cycle Physics (PCO) group, created in 2005 and led by Dr. Rodrigo Lopez-Martens. The group studies the interaction of high-intensity lasers with matter with the goal of following and controlling the collective movement of relativistic electrons (with a velocity close to the speed of light) on a time scale below an oscillation cycle of the laser light.

The PCO group is at the state of the art of laser development and post-compression, representing a more developed and complex laser facility. Understanding post-compression, and in particular its limitations and potential, becomes much easier when there's the possibility of working directly with more established setups and with experts with years long experience in the field. A small internship of one month at the PCO group was then a unique opportunity, making the work at VOXEL much more tranquil and swift.

3.2 Setup of the post-compression system

The PCO group works in the Salle Noire where the fully vacuum-integrated post-compressor setup is placed, as can be seen in figure 3.1. To start, a seed from a Ti:Sapphire double CPA chain delivers pulses of 10mJ (with shot-to-shot stability of $< 0.3\%$ RMS over hours) at 1 kHz repetition rate with temporal contrast of $> 10^{10}$ at ≈ -10 ps before the pulse peak [58]. As seen in chapter 1, sub-2-cycle CEP stabilized pulses are particularly attractive, providing high temporal resolution in time-resolved

experiments and also facilitating the generation of isolated attosecond XUV pulses in a simple way. The CEP is stabilised with an automatic feedback system, using an error signal from an f-to-$2f$ interferometer (Menlo, APS 800) [59, 60].

The coupling window is rather sensitive to nonlinear effects as previously mentioned and so, to decrease these effects, the PCO group decided to design a large vacuum chamber that is directly connected to the HCF [6]. All the focusing optics were placed in this chamber, including the last 8 chirped mirrors (introducing $\sim -2000\text{fs}^2$) that perform the final compression down to the FTL of 24 fs. This is done so that not even the longer-duration beam suffers dispersion by going through the window.

The chamber was built to a standard that is usually only used in ultrahigh vacuum applications. This was done since air has a nonlinear refractive index many times higher than Helium and, in particular, the ionisation level is much lower, and even more so in hydro-carbonates which easily pollute surfaces. The Teflon tube from the gas bottle to the chamber was also replaced by a stainless steel tube to avoid losses. Recently, a contrast filter [61] was also installed to reduce the noise in the setup, having a temporal contrast of 10^{11}.

The post-compression system in *Salle Noire* uses three main strategies to scale the technique of the ~ 0.4 TW peak power of the CPA chain.

First, a stretched flexible hollow core fibre was used so that an arbitrary length of interaction was accessible without losing the waveguide properties [62], this was set at 2.5 m with 536μ m. A conical glass taper was also introduced coaxially to the fibre to create strong protection from eventual misalignment or pedestals in the spatial beam profile. After, a reflective mirror telescope focuses the beam into the fibre with an effective focus of ~ 4.2 m. This is maintained with active-beam pointing stabilisation (like the one under commission at VOXEL) to ensure hour-long stability of the coupling into the fibre. Notice how a leak from the first and last mirrors is directed to photosensitive detectors in the near and far fields, which will measure the error signal for the stabilisation system.

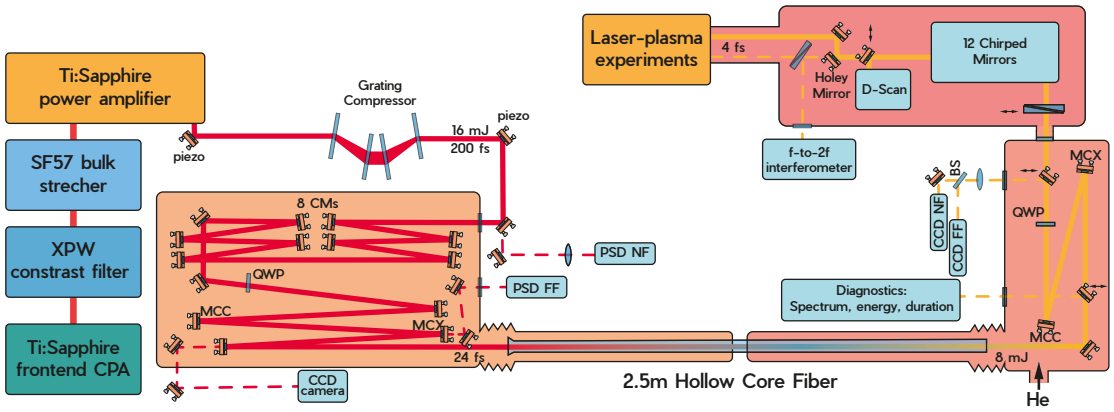

Figure 3.1: Schematics of the vacuum-integrated stretched flexible hollow fibre pulse compressor setup at *Salle Noire*. PSD photosensitive detector, NF near field, FF far field, piezo piezo-driven mirror mounts, MCX convex mirror, MCC concave mirror, QWP quarter-wave plate. Adapted from [63].

Second, the fibre is differentially pumped with high-purity Helium gas, creating a stable pressure

gradient across the waveguide from pressures from < 0.1 mbar in the entrance to 2 bar at the output. As before, differential pumping is employed so that no undesirable nonlinear effects occur at the entrance of the fibre while also enhancing the coupling efficiency and its stability. Differential pumping is also a good way to counteract the decreasing nonlinearity due to the losses that occur throughout the fibre.

Third, circular polarisation was used, in contrast to the setup in Lisbon. This decision comes from the mitigation effect that circular polarisation has both on multi-photon ionisation and self-focusing. The circular polarisation also reduces losses and instabilities due to the cycling of energy between fibre modes [64]. For this, two broadband quarter-waveplates are inserted before and after the fibre in order to switch from linear to circular polarisation and back.

Finally we reach the output chamber, where, two removable mirrors send the beam to diagnostics of position, spatial profile, spectrum and pulse energy. Two other mirrors then make alignment possible into the far and near-field references. A 3 mm fused-silica window separates the helium-filled chamber from the vacuum chamber that follows. In this new chamber, we find a pair of motorised fused silica wedges, exactly as the setup of the D-Scan discussed in 2.3, following a set of highly dispersive (-40 fs^2 each) 12 chirped mirrors (PC70, Ultrafast Innovations) that further compress the pulse into optimum pulse compression. This occurs, of course, with some fine-tuning of the wedges. The chamber also features a D-Scan measuring head already described that, in collaboration with the wedges, measures the compressed pulse. Note that the measuring head is also in vacuum, compared to the VOXEL setup where currently the whole compression and diagnostics is in air. In 2020, the group achieved 3.4 ± 0.1 fs pulses of FWHM using 1.3 bars of Helium with a spectrum broad enough for a FTL duration of 2.9 fs, these results can be explored in [63]. A rather interesting study of how *Salle Noire* is affected by Spatio-temporal couplings is presented in [65].

3.3 Results

The experimental results that are described in this section were obtained at LOA in March of 2022 with the help of Dr. Louis Daniault and PhD student Jaismeen Kaur who guided us through the alignment and data acquisition procedures. This evolution is plotted in figure 3.3. As we can see, the increase in the bandwidth of the spectrum is similar to the one in the VOXEL laboratory (figure 2.20) with the difference of having the full intensity profile here, without the filtering at IR wavelengths that occurs at VOXEL due to the spectrometer response.

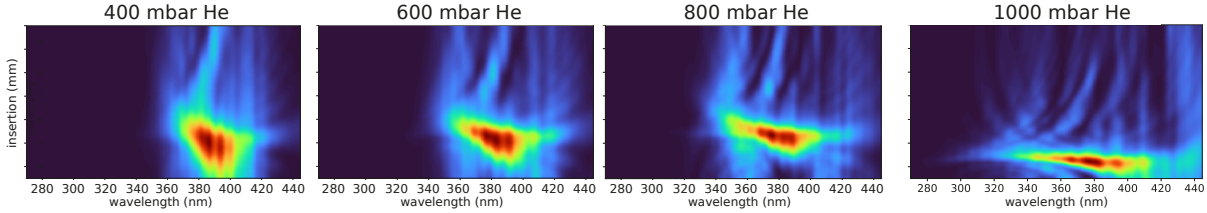

Figure 3.2: Evolution of the D-Scan trace through increasing gas pressure.

At Lisbon, we have the optimum pressure around 1200 mbar with a resource to Argon. At *Salle*

Noire, we find a similar spectral width when employing 1000 mbar of Helium on the output of the HCF. In the Helium-filled fibre, it is clear that a lot less self-focusing and ionisation occurs, as shown by the lack of a ”bump” in the 500-600 nm range.

There was also the opportunity to obtain a D-Scan trace for different pressures of He above 400 mbar, which gives rather interesting results. As you can see in figure 3.2 it is rather easy to tune the pulse duration almost continuously, making the D-Scan trace longer and narrower.

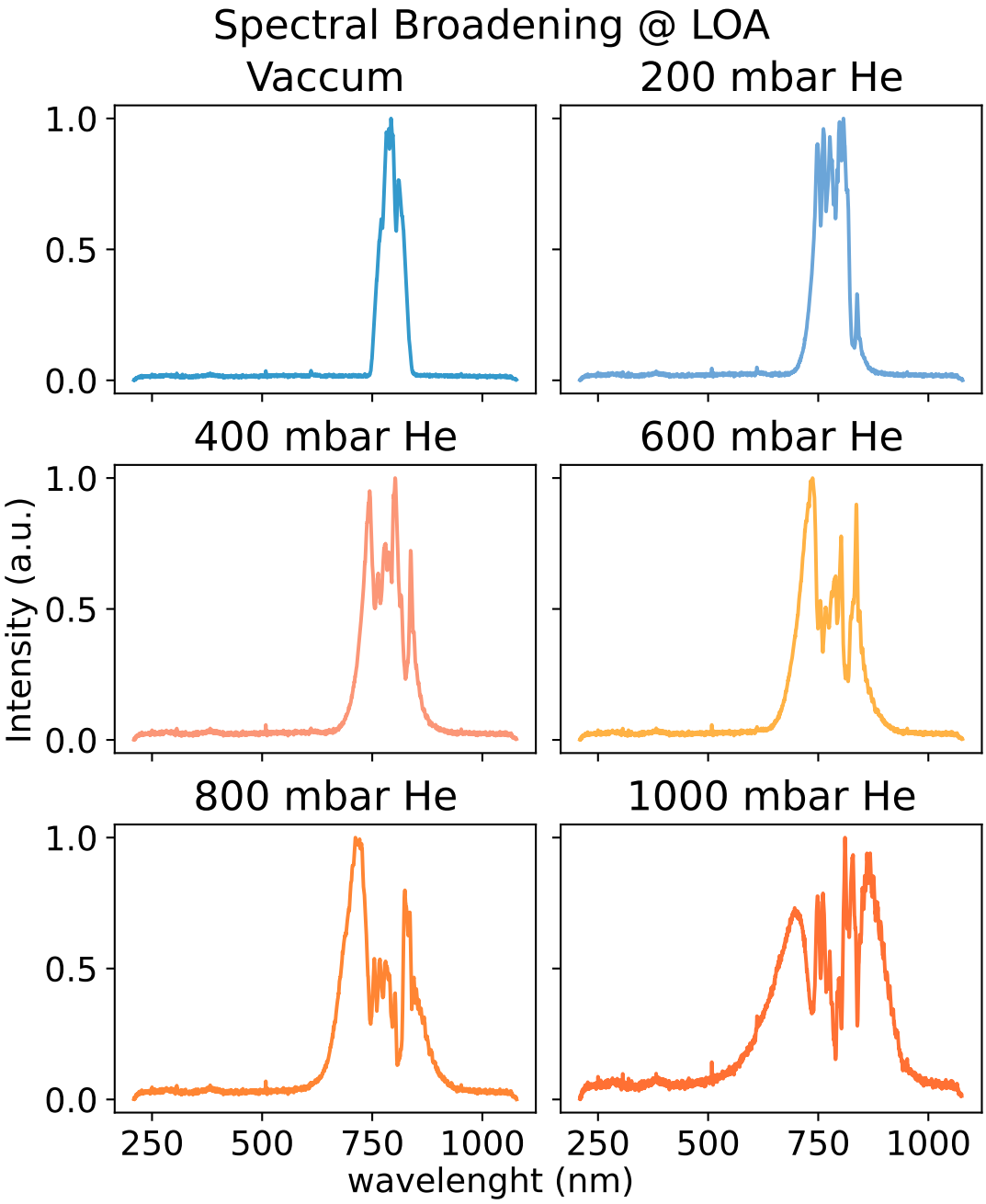

Figure 3.3: Evolution of the normalised spectral shapes with increasing gas pressure in the HCF of Salle Noire of LOA.

In the case of the setup at LOA, the TOD is already corrected without the need for passive dispersion optics with specific GDD/TOD. This happens since the whole setup is mostly in vacuum, only having a

noble gas in the spectral broadening area. Having the beam interact only with fused silica adds a lot of GDD but less Third-Order Dispersion, which, as we know is much harder to compress.

In figure 3.4 we find a more detailed analysis of the pulse with the shortest pulse duration. As just mentioned, the trace is almost perfectly horizontal and occupies a few limited amounts of insertion i.e. is almost perfectly compressed down to FTL [1]. This translates to FWHM=3.9 fs, a value that, I believe, could be lower still with a more lengthy study but such was not possible, in fact, values of 3.4 fs and 3.6 fs are cited in [6, 63]. It is worth noticing how the spectrum profile phase becomes more horizontal in comparison to the one we achieved in Lisbon.

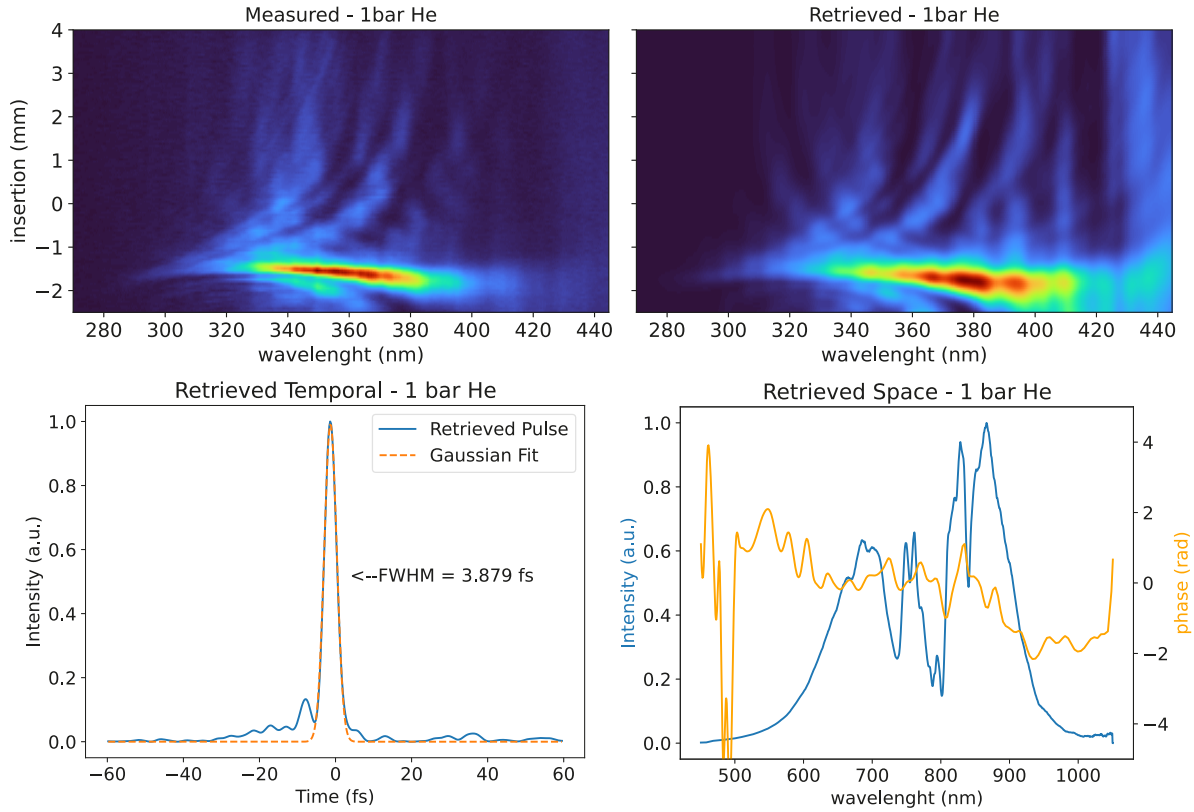

Figure 3.4: Measured (top left) and retrieved D-Scan trace (top right), temporal (left bottom) and spacial (bottom right) retrievals of the optimal HCF broadening in the *Salle Noire*.

There were however some imperfections in the compression. First, there's a slight remaining TOD of a few fs^3. Second, around the 550-700 nm range, the phase is clearly variating a lot, due to the chirped mirrors used, this however offers no significance since the spectral intensity in the area is close to zero. Smoothing these oscillations and correcting the TOD would increase the peak power and reduce the pulse duration making it much closer to FTL. Much more complex is the range under 550nm, where the phase is completely uncontrollable, at this time there are, not yet, chirped mirrors available that make compression in this region possible and so a hard limit is, for now, set in the duration of 3.4 fs or 1.3 optical cycles.

There was also the possibility of analysing how the CEP feedback loop behaved. From figure 3.1

[1] The trace is lower in the vertical axis since the optimal compression point needs less GDD then the zero insertion supports.

we see that a reflection from the front face of a pair of thin wedges is used to generate the f-to-2f signal, which, as before mentioned, provides information regarding necessary changes. The error signal calculated is used to modulate the phase offset of the oscillator, locking electronics to correct for slow CEP drifts accumulated through the laser chain [63]. In figures 3.5 and 3.6 we see the original relative CEP stability and the relative CEP stability after the corrections described.

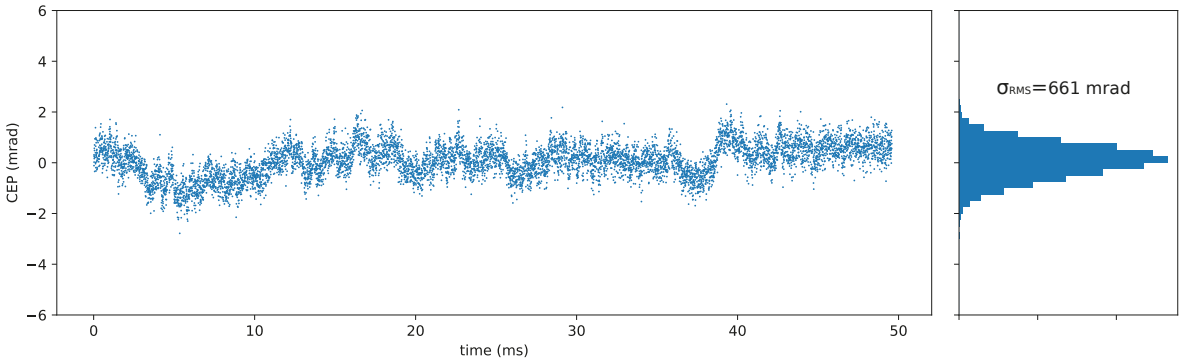

Figure 3.5: Relative CEP stability without feedback.

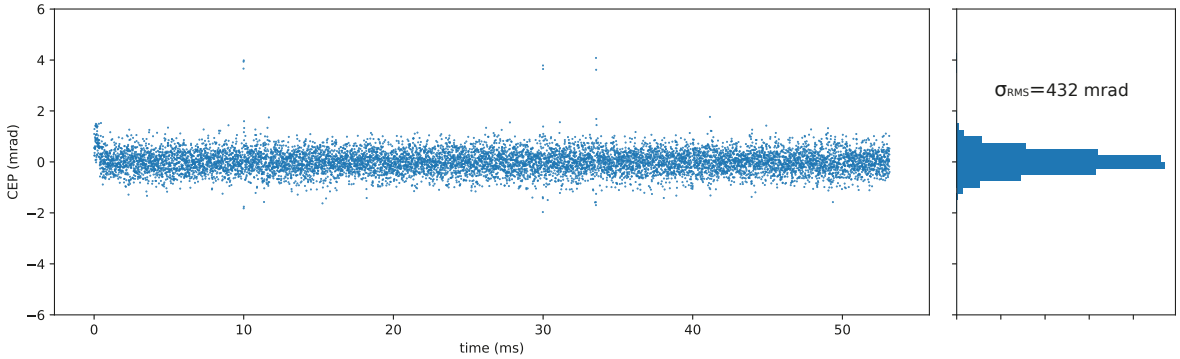

Figure 3.6: Relative CEP stability with feedback.

The stabilisation of CEP lowers the σ_{RMS} from 661 mrad down to 432 mrad, allowing the constant creation of isolated attosecond pulses, the motivation for this work. At the VOXEL laboratory, we have no way of measuring the CEP variations and so we can expect variations around 700 mrad since we use also a Ti:Sapphire system with similar capabilities.

To study how the FTL decreases with increasing pressure we plotted both the RMS spectral width and the FTL pulse width in figure 3.7. The spectral broadening shows a behaviour close to the theoretical $\sqrt{1+x^2}$ [6] with deviations that we believe derive from possible pollution inside the HCF. We can, from this linear increase, also conclude that only SPM is occurring in the fibre with no obvious sign of the onset of self-focusing.

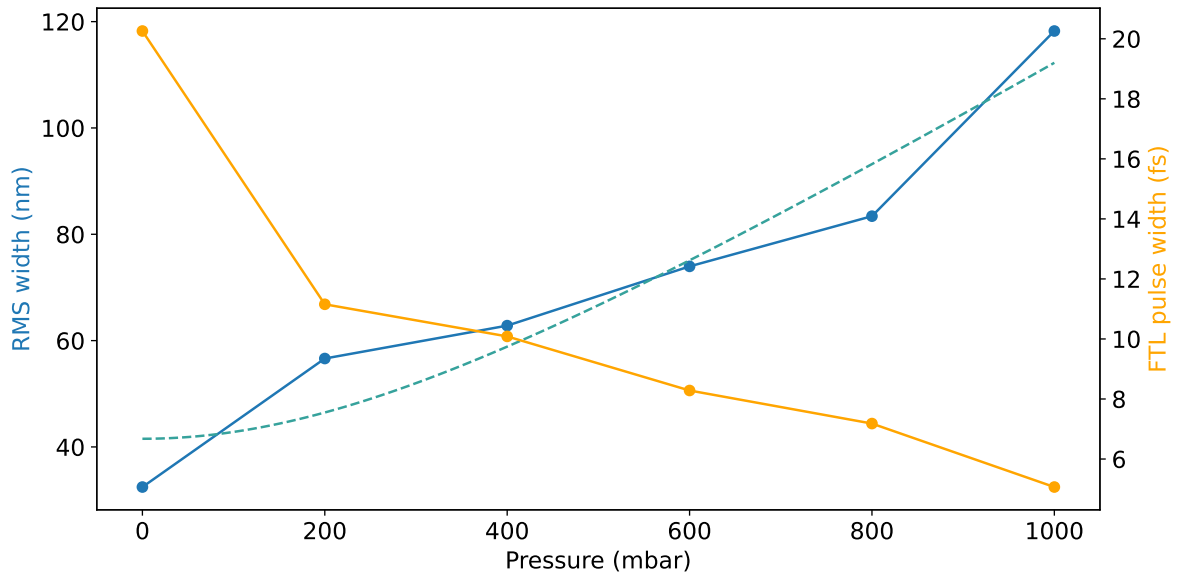

Figure 3.7: Evolution of the RMS spectral widths (blue) and FTL pulse widths (yellow) for different pressures of Helium inside the fibre. The green dashed line represents a fit of the experimental RMS spectral widths to the theoretical $\sqrt{1+x^2}$.

3.4 Summary and Conclusions

- We presented the Hollow-Core Fiber setup of the *Salle Noire* of LOA, one of the setups in the front edge of post-compression;
- Analysed how the spectral broadening behaves in a larger, differentially pumped helium-filled fibre;
- Achieved maximum compression with a pressure of 1 bar of helium at the output. There we found FWHM=3.9 fs, with minimum GDD and TOD;
- Measured the Carrier Envelope Phase with and without a feedback loop for stabilisation;
- Plotted the RMS width and FTL pulse duration in function of gas pressure and concluded it followed the expected trend.

Chapter 4

Post Compression with a Multipass Cell

Although this thesis is mostly focused on broadening in Hollow-Core Fiber for a true understanding of post-compression methods there's also the need to look further into the currently most used method of free propagation: the gas-filled Multipass Cell.

4.1 Accumulated B-integral and Scaling Rules

Introduced in 1.3.1, the MPC has a simple geometry consisting of two identical mirrors with radius of curvature R separated by a distance L as described in 1.3.1. There are two main options to create a nonlinear medium inside the cavity, using plates and filling the cavity with a nonlinear gas.

Here we will mostly look at the second option since such was the nature of the setup that was available to us in LOA. The nonlinear phase here is continuously accumulated while the beam travels on a distance comparable to or larger than the Rayleigh range and so results in larger robustness of the beam with respect to space-time couplings than when the B-integral can be considered to be accumulated in a single transverse plane, as is the case for bulk plate-based MPCs. The intuitive picture is that the Spatio-temporal components of the beam/pulse are simultaneously modified by the nonlinearity and mixed by diffraction, which homogenises the Spatio-temporal field [23].

The study of MPCs is of course extensive and complex and so the reader is advised to read further into the subject in [23, 26, 66], since a deeper description of spectral broadening is out of the scope of this thesis. Let us, instead, present a summary of the theory of the spectral broadening present in this type of setups.

To start, since we know that the goal is to homogenise the nonlinear phase over the beam, let's look at the definition used in guided-wave nonlinear optics,

$$B_{roundtrip} = 4\frac{2\pi n_2 P_{peak}}{\lambda}\int_0^{L/2}\frac{1}{A_{eff}(z)}\mathrm{d}z \tag{4.1}$$

where n_2 is the nonlinear refractive index of the gas and P_{peak} is the peak power assumed independent of the propagation distance in the absence of significant dispersion, as before. A_{eff} is still the local effective area, in this case defined as $A_{eff} = \pi\omega^2(z)$. Equation 4.1 gives values that are equal to half the B-integral accumulated on-axis (corresponding to the maximum intensity), because of the Gaussian shape of the beam.

It is then possible to calculate the B-integral in function of the MPC parameters R and L knowing the the critical power for self-focusing is $P_{crit} = \frac{3.77\lambda_0^2}{8\pi n_0 n_2}$ (one of the limits of this method, as in the HCF),

$$B_{roundtrip} = \pi \frac{P_{peak}}{P_{crit}} atan\left(\sqrt{\frac{L}{2R-L}}\right). \tag{4.2}$$

We can then present the design rules of a gas-filled MPC. First, the input power limits the pressure for a given noble gas due to the critical power for self-focusing. Second, the MPC geometry is limited by (i) the gas ionisation at the waist and (ii) the damage threshold of the mirrors. The mirror damage usually leads to geometries of near concentric cells (L close to $2R$), that increase rapidly the beam size at the stability edge. This, however, decreases the beam size at the waist, interfering with the ionisation limit. This might not be possible to appease for a given curvature radius and so both R and L might need to be increased. This process is responsible for the design in the range of 10 m-long cells for high energy systems in the 100mJ range. More on scaling rules can be visited in [67].

A MPC gives different results, limitations and potential. To analyse this, let us present the MPC designed by the PCO group.

4.2 Multipass Cell at LOA

At *Salle Noire 2.0*, a Ti:Sapphire laser system (Femtopower Pro-HE) delivers 30 fs compressed pulses of 1.2 mJ energy at 1 kHz of repetition rate with an acoustic-optic programmable dispersive filter (Dazzler by Fastlight) in the main amplifier that allows for the fine-tuning of the spectral phase. The beam is then spatially filtered under vacuum in a 21 cm HCF of 250 μm of diameter, fixing the beam waist position and dimensions at the output. With an efficiency of 80%, the energy throughput is 1 mJ.

The HCF-filtered beam then enters the MPC stage made of two 2" enhanced silver-coated mirrors with 1.5 m radii of curvature separated by $\sim$ 3 m, making this a nearly concentric cavity. The number of passes is variable and can go up to 18 with two small rectangular silver mirrors that allow the injection and the pick off of the beam. The setup is locked inside an airtight cavity filled with argon at different pressures. A set of lenses after the HCF matches the beam waist at the centre of the MPC to a diameter of $\sim$ 250 μm, keeping the beam caustic periodic throughout the passes in the MPC [68]. The Dazzler is used to compensate for the dispersion from air, lenses and windows so that the beam that enters the MPC is at FTL. Finally, at the output, the beam is temporally compressed by a set of double-angle chirped mirrors (PC 42 from Ultrafast Innovations) and two fused silica wedges to finely compensate the pulse spectral phase, similar to the compression from the D-Scan and the HCF at LOA. To analyse the beam both in space and time, a single shot SHG-FROG and an imaging spectrometer are employed.

This is schematised in figure 4.1.

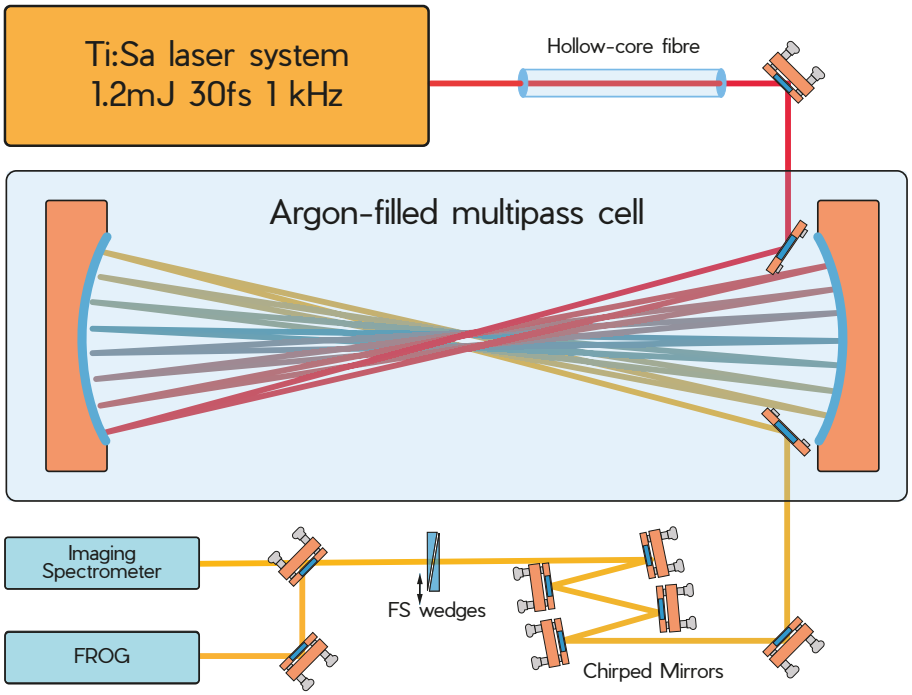

Figure 4.1: Scheme of the multipass cell used in Salle Noire 2.0 of LOA.

4.3 Results

The output spectrum was studied through several gas pressures having always 16 passes in the MPC. This is plotted in figure 4.2.

One can immediately see that the spectrum is much more symmetrical throughout the whole spectral broadening range, as would be expected from theory. Until around 150 mbar the spectral broadening is linear with no excessive distortion of the spectral profile, saturating at high pressures as seen in figure 4.3 where the RMS spectral width and the corresponding FTL are plotted through several gas pressures. This shows that spectral broadening increases linearly with the gas pressure up to $\sim$ 150 mbar but saturates at higher pressures. The gas dispersion is also pressure dependent and so plays a crucial role in spectral broadening. At lower pressures, the propagation is considered dispersion free. There, the beam is subjected to pure SPM in all 16 passes with a constant temporal profile. This is the reason why, at first, the spectrum increases linearly with gas pressure.

The changes come when the gas pressure reaches 150 mbar, there the spectral width starts increasing along with the dispersion coefficient of the gas and there's a temporal spread of the pulses for the last passes. This decreases the peak power and so spectral broadening starts to be limited. However, SPM along with dispersion leads to a much smoother spectral profile compared to dispersion-less spectral broadening like the one we have in the HCF, where strong modulations appear with pure SPM.

At even higher pressures, this is even more aggravated and the spreading comes earlier and at

earlier passes. This, of course, means that the passes that follow have little contribution to spectral broadening. It might happen also that chirped pulses accumulate SPM and the onset of nonlinear spectral phase at high orders can degrade the pulse compressibility. It means that many passes do not necessarily correspond to shorter pulses.

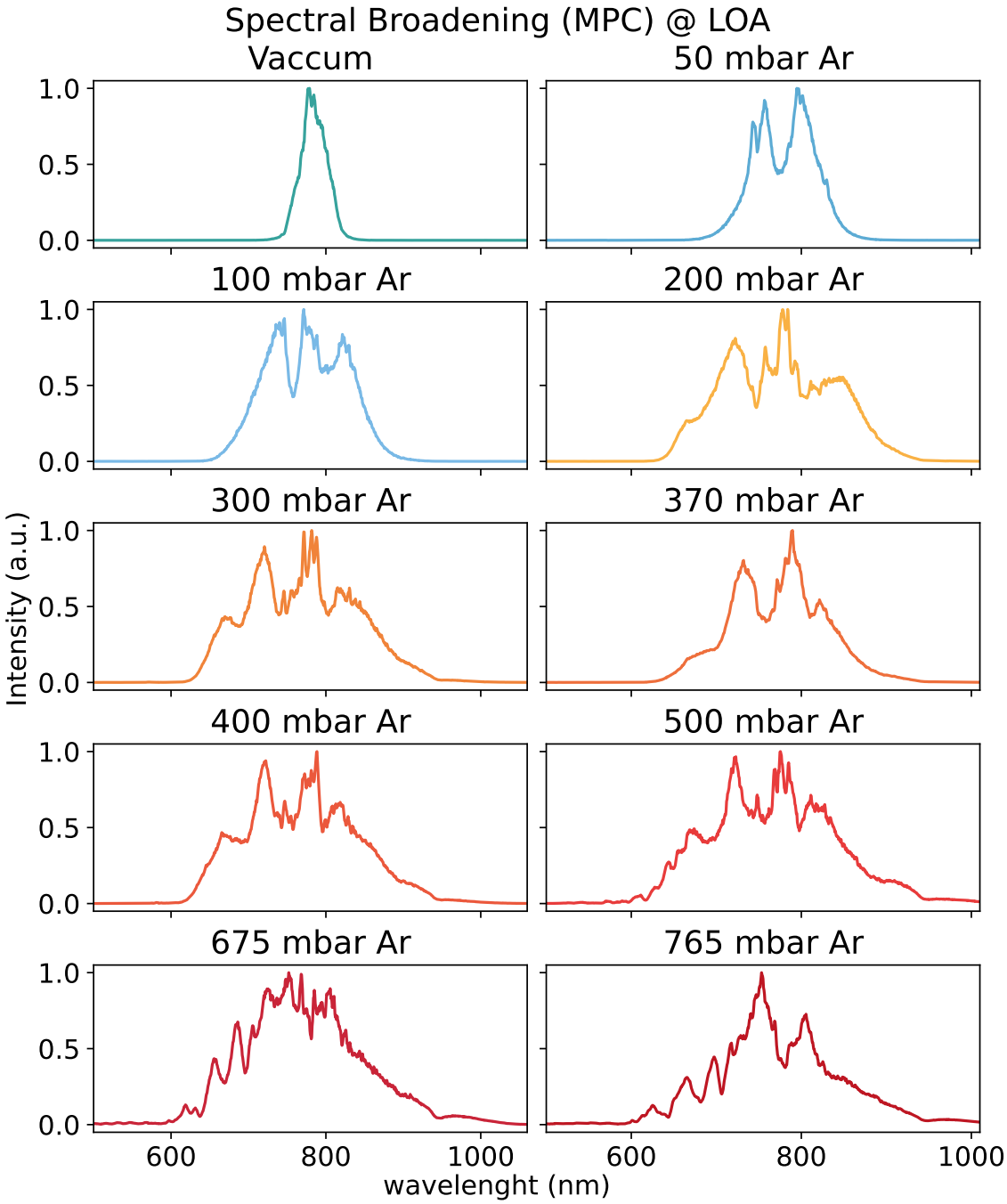

Figure 4.2: Evolution of the normalised spectral shapes with increasing gas pressure in the MPC of Salle Noire of LOA.

From 500 mbar forward, the spectra start to include distortions and a pedestal with some oscillations in the shorter wavelengths. The onset of this distortion is very steep with increasing gas pressure and determines the point where the spectral quality starts to degrade. This point does not, however,

correspond to the critical power above which catastrophic behaviour starts to occurs. Here we still have a low enough ionisation rate to have noticeable impact under these conditions.

In this area (pressure above 500 mbar), numerical studies done in [68] show that an excessive impact of self-steepening occurs already on the first pass. Self-steepening is a phenomenon that has already been described on 2.4 (and not surprisingly also occurs in MPCs), it creates an optical shock with a highly distorted pulse profile. In the following passes, the interplay between SPM, self-steepening and gas dispersion introduces strong temporal and spectral modulations in the shorter wavelengths that affect the spectral quality and the compressibility of the pulse. Remember that this effect cannot be avoided since it occurs mostly in the first pass, and so there's no way to contradict it by limiting the number of passes. In any case, even for higher pressures, the spectral bandwidth does not increase.

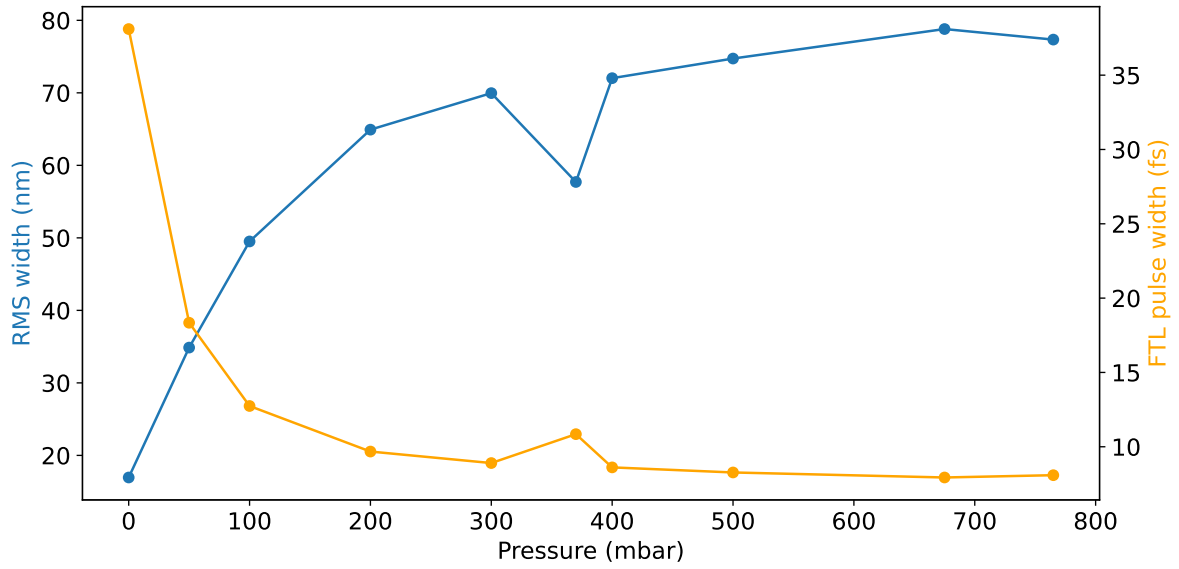

Figure 4.3: Evolution of the RMS spectral widths and FTL pulse widths for different pressures of Helium inside the MPC.

The output energy after the MPC is usually around 79% due to the losses that arise from the inherently flawed mirrors, which have a reflectivity of 98.5% for each pass over the entire bandwidth. After, the 9 pairs of chirped mirrors introduce a group-delay dispersion of 378 fs^2 followed by the two wedges previously mentioned. This compression setup is, of course, also not perfect and the whole post-compression efficiency was measured to be 67%.

In figure 4.4 we find the FROG traces and the correspondent retrieved temporal spacial profiles taken by the SHG-FROG for the optimal gas pressure of 370 mbar. As you can see, the compressed retrieved pulse has a duration of 6.8 fs which corresponds to 3.5 optical-cycles output pulses. There was also the possibility of measuring the beam profile with the imaging spectrometer but, unfortunately, it was impossible to take such measurements due to time constraints. Nevertheless, previous measurements published by the PCO group show that this setup (at variables similar to our measurements) had a nice spectral homogeneity, above 99% at the beam FWHM and above 95% at $1/e^2$ in both the horizontal and vertical dimensions.

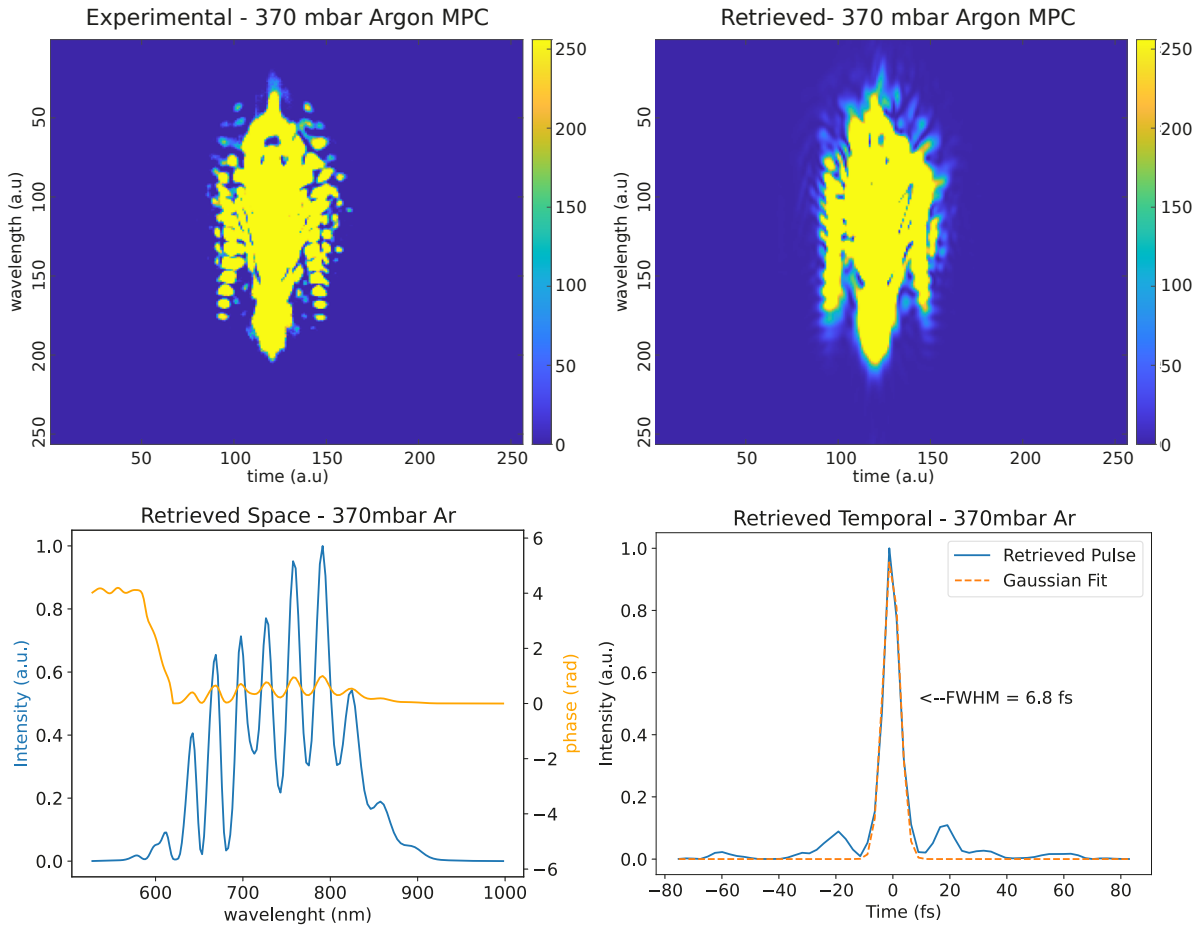

Figure 4.4: Experimental (top left) and retrieved (top right) FROG traces as well as the temporal (bottom left) and spatial (bottom right) retrievals of the optimal MPC broadening in the Salle Noire.

4.4 Cross-polarised wave generation in MPC

During the visit to Paris, there was also the opportunity to take part in the new experiment being developed by the PCO group as described in [69].

The group developed the first implementation of cross-polarised wave generation, XPW [1], in a MPC. XPW generation is a well-established technique that is known to improve temporal contrast by three orders of magnitude with up to 33% internal conversion efficiency [72], given that the input beam is spatially filtered and has a super-Gaussian profile. The MPC, as just described before, has the capability of spatially homogenising non-linear effects and distributing the accumulation over the propagation inside the cell. This creates an overall smooth spectral profile with excellent output beam quality and high conversion efficiency.

To start, the linearly polarised, near FTL pulse describe before (1mJ, 30fs, 1kHz) is inserted into the MPC cavity under vacuum. With the difference that now, two AR-coated 600 mm thick, holographic cut BaF2 crystals are placed approximately 10 cm from the concave mirrors. This two crystals allow for the conversion with a 2% efficiency per pass which is then filtered outside of the MPC by a thin-

[1] See [70] and [71] for further understanding of cross-polarised wave generation.

film polariser. After, a series of chirped mirrors allow for the temporal compression of the spectrally broadened XPW pulses which are then analysed by an SHG-FROG, an Imaging Spectrometer and a 12-orders of magnitude dynamic range third-order auto-correlator (TUNDRA). The setup is schematised in figure 4.5.

This means then that pulse shortening and temporal contrast enhancement of mJ-pulses were simultaneously achieved with a 20% global efficiency giving 18.2fs pulses with measured temporal contrast enhancement of at least 3 orders of magnitude, limited only by the extinction ratio of the polariser.

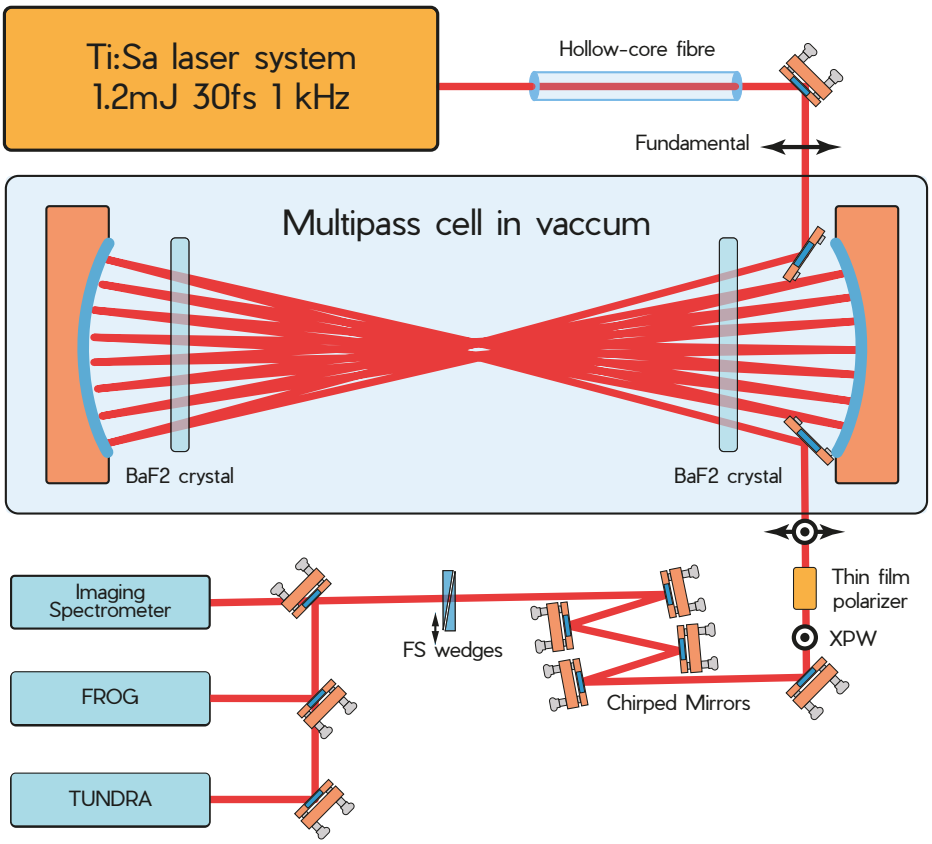

Figure 4.5: XPW-MPC experimental set-up layout. Adapted from [69].

4.5 Summary and Conclusions

- Theory about the accumulated B-integral and scaling rules of Multipass Cell was presented;
- The MPC system of LOA was described;
- An analysis of how spectral broadening behaves in a free propagation technique of post-compression was presented;
- A study was presented on how the gas pressure of Argon affects the RMS bandwidth and the FTL pulse duration of an MPC;
- A maximum compression point was reached, achieving a post-compressed pulse with a FWHM of 6.8 f with a pressure of 370 mbar of Argon. The setup has an efficiency of 67% and so delivers pulses with 670 μJ;
- Finally, we presented our collaboration in an experiment of cross-polarised wave generation within an MPC.

Chapter 5

Discussion

This thesis is composed of not only the installation of a single-cycle pulse source in VOXEL but also of the study of two well-established spectral broadening systems, it makes then perfect sense to compare both and, particularly, justify our preference for the installation of a HCF since the pair represents what constitutes state of art techniques for single or few-cycle laser pulses. Their differences in potential and limitations will be analysed here and are summarised in table 5.1.

The HCF has a first obvious limitation: the ionisation that arises at high intensities. Higher energy inputs are not permitted in common one-meter fibres, in fact, they imply larger capillary cores with corresponding longer interaction lengths that can easily become impractical for table-top use. On the low energy side, these structures are also limited by high losses in the small diameter capillaries needed. Both the limitations on the high and low energy imply that the hollow-core fibre method need to be comprised between a few 100μJ and a few mJ. The MPC can then be a solution to these limitations, being much easier to scale to high-peak and average power with higher efficiency.

The scaling of the gas-filled Multipass Cell is limited only by the damage threshold and the reflectivity of the mirrors, in fact, high power spectral broadening up to 112mJ has recently been achieved [73]. Extending the range of the MPC into the single-cycle regime does, however, come with challenges. In order to maintain the high efficiency and the low B-integral per pass expected, the cavity mirrors must necessarily support near-octave-spanning spectral bandwidth with high reflectivity and low group delay dispersion while still exhibiting a high damage threshold, to maintain the cell size within reason. For this reason, in a lot of cases, it occurs that two different stages have to be implemented. The first, made with high damage threshold dielectric mirrors and high reflectivity but moderate bandwidths, leads to post-compressed pulses of a few 10's of fs and transmission efficiencies well above 95%. The second, requiring large bandwidth optics at the expense of lower reflectivity and damage threshold, yields few-cycle pulses with efficiencies around 80%. This is in contrast to the HCF that, as we know, requires only one stage.

The free-space form of propagation is much easier to implement since it's a much more robust system (not subject to problems like the flexibility of the fibre) making the beam pointing at the output much more flexible. However, for any spectral broadening technique insensitive to beam-pointing instabilities,

pointing instability issues must be addressed before seeding the pulse into the system which can be extremely hard. The fibre option, being much harder to implement as seen in chapter 2, does fix the beam in position and pointing due to the nature of the waveguide, which can be of high importance in several applications.

There is also, of course, the saturation on the spectral width of the Multipass Cell that occurs once self-steepening settles in. Although self-steepening also occurs in HCFs, its effects show themselves at only extremely high gas pressures and can be corrected with some careful compensation from ionisation.

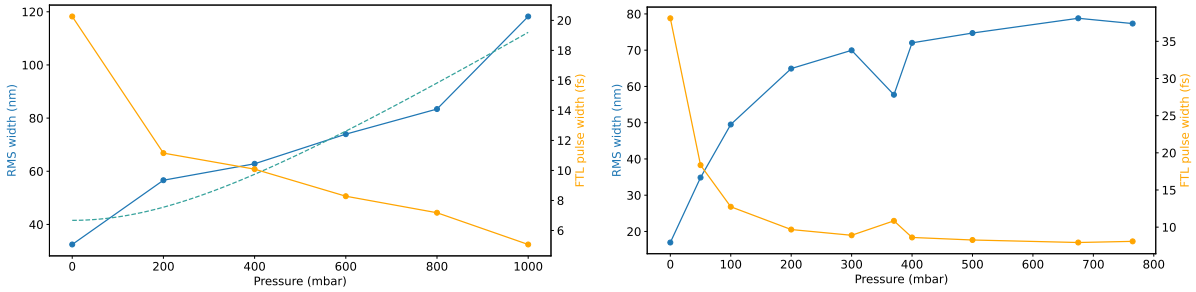

Figure 5.1: Comparison of the response to the increasing pressure of each spectral broadening system (HCF on the left, MPC on the right).

To finalise, both the HCF and the MPC options provide spatial homogeneous spectral broadening but the nonlinear interaction in free-space propagation is distributed over much larger path lengths than in capillaries and so there is a reduction of Spatio-temporal couplings.

Since we already had the Hollow-Core Fiber system available at the VOXEL laboratory, it was obvious that was our choice at this first appproach at a post-compression system. This was, in any case, fortunate since the the capability of achieving single-cycle pulses was much more established in this method (even with the causality of achieving lower efficiencies). It also became evident that the extremely precise pointing stability that comes with a HCF was of great importance for the applications we desire to achieve in the VOXEL lab.

	Hollow-Core Fibre	Multipass Cell
Efficiency[1]	$\sim$ 50%	$\sim$ 79%
Energy Range	100μJ - mJ	$\sim$ 10μJ - $\sim$ 110mJ
Beam pointing (input)	Extremely sensitive	Not sensitive
Beam pointing (output)	Extremely precise	Depends on the input
Spatial Homogeneity	Yes	Yes
Spatio-temporal Couplings	Sometimes	No
Response to increasing pressure	Quasi-linear [2]	Saturates at higher pressures
Needs several stages[3]	No	In most cases

Table 5.1: Comparison between the two spectral broadening methods.

[2]For the single-cycle regime
[3]For the single-cycle regime

Chapter 6

Conclusions and Prospectives

In this work we achieved our main goal of having near single-cycle laser pulses available at the VOXEL laboratory. We started by creating a brand new mobile FROG setup capable of measuring the temporal and spectral characteristics of the Astrella beam. We studied how changes in the delay of the Pockels cells and different amounts of dispersion affect these same characteristics. We also measured the beam pointing at focus where the fibre entrance would be placed. Concluded that a beam stabilisation system is needed for hour-long operations due to a drift in the vertical direction.

With proper knowledge of the limitations of our laser we finally started the implementation of the Hollow-Core Fiber system. We moved both the Astrella and the Hydra lasers to create space and started to implement a new beamline in-between the lasers to be directed into the fibre. We aligned the on-axis line of the fibre with both the NIR and HeNe lasers. After, we placed an achromatic lens and found the focus plane where we could achieve optimal coupling into the fibre. We also placed a beam profiler to monitor any changes in beam pointing and coupling. We then placed the rail where the fibre would lay as well as the gas and vacuum systems that were connected to a gas station. We aligned this setup to the previously fixed beam line. Finally, we placed the hollow-core fibre.

We optimised the spectral broadening system by studying different values of gas pressure, input polarisation, dispersion and energy of the input beam. We also optimised the angle of the Brewster windows inserted at the entrance and the output of the fibre. Simultaneously, there was constant attention regarding the coupling into the fibre since any deviations caused permanent damage to the cladding.

With the help of Sphere Ultrafast Photonics, we installed the D-Scan system composed of two stages: a compression system and a measuring head. Again, optimisation was required since all the previous studies had to be repeated for the newly installed D-Scan system which proved to be particularly sensitive to polarisation errors.

We successfully achieved almost octave-spanning spectral width. This resulted in the achievement of sub-4fs pulses with minimal group delay dispersion and transmission of 33%. These results represent a powerful tool for table-top single-cycle laser pulses in the VOXEL laboratory. We also installed a new single-cycle beam line to create broadband harmonics.

In the *Laboratoire d'Optique Appliquée* (LOA) a part of *Institut Polytechnique de Paris*, we studied

what constitutes the state of the art of post-compression into the single-cycle regime, both in hollow-core fibres and multipass setups. We also collaborated in the creation of a novel setup concerning cross-polarised wave generation in multipass cells, achieving simultaneous pulse shortening and temporal contrast enhancement.

Finally, we compared the two techniques and confirmed, now with a better understanding of the limits and potentials of the method, our preference of a Hollow-Core Fiber for the regime we wanted to achieve.

Future Work

The installation of the beam stabilisation system already commissioned is crucial for the continuous operation of the post-compression system. This needs to be installed and will require a new, hopefully, less arduous, optimisation of the spectral broadening. An autocorrelator should arrive any day now and will permit a more professional analysis of the dispersion of the pulse and so a new study on how the dispersion of the input beam affects the spectral broadening should be done.

After these corrections of the setup, not achievable before due to time constraints and lack of the resources just mentioned, the setup is prepared to be employed in the creation of the isolated attosecond pulses that gave the motivation for this thesis. A novel attosecond holography setup [74] designed with the capability of retrieving sub-fs, 100 nm-scale information has never been demonstrated with true attosecond pulses. This experiment has been planned and should be implemented in the next months.

Finally, work performed at LOA allowed us to study the compression of much higher energy pulses. This study will allow the design of a new post-compression station at the expanded VOXEL laboratory, currently under design.

Contributions

The work of this thesis has been presented in:

- The V International Conference on Applications of Optics and Photonics (AOP) in Guimarães, Portugal on July 18th-22th, 2022 (oral presentation) ;
- The ELI Summer School 2022 (ELISS2022) in Szeged, Hungary on August 30th-September 2nd, 2022 (poster);
- The 2022 Frontiers in Optics + Laser Science Conference (FiO + LS) in Rochester, New York, USA on October 17th–20th, 2022 (poster).

At end of this work, an article for Micromachines is being prepared for the special issue *Optics and Photonics—Micro and Nano Structures, Materials and Devices (AOP 2022)*.

Bibliography

[1] S. E. Künzel, "Characterization, optimization and applications of coherent XUV sources," eng, Ph.D. dissertation, 2017.

[2] S. M. Teichmann, F. Silva, S. L. Cousin, and J. Biegert, "Importance of intensity-to-phase coupling for water-window high-order-harmonic generation with few-cycle pulses," *Physical Review A*, vol. 91, no. 6, p. 063 817, 2015.

[3] D. Strickland and G. Mourou, "Compression of amplified chirped optical pulses," *Optics Communication*, vol. 56, pp. 219–221, 3 1985.

[4] T. Nagy, P. Simon, and L. Veisz, "High-energy few-cycle pulses: Post-compression techniques," *Advances in Physics: X*, vol. 6, no. 1, p. 1 845 795, 2020.

[5] P. Rigaud *et al.*, "Supercontinuum-seeded few-cycle mid-infrared opcpa system," *Optics express*, vol. 24, no. 23, pp. 26 494–26 502, 2016.

[6] F. Böhle, "Near-single-cycle laser for driving relativistic plasma mirrors at khz repetition rate - development and application," Ph.D. dissertation, Dec. 2017.

[7] M. J. Weber, *Handbook of optical materials*. CRC press, 2018.

[8] R. Trebino, *Frequency-Resolved Optical Gating: The Measurement of Ultrashort Laser Pulses*. Springer US, 2000.

[9] R. W. Boyd, *Nonlinear optics*. Academic press, 2020.

[10] K. Midorikawa, "Ultrafast dynamic imaging," *Nature Photonics*, vol. 5, no. 11, pp. 640–641, 2011.

[11] M. Lewenstein, P. Balcou, M. Y. Ivanov, A. L'Huillier, and P. B. Corkum, "Theory of high-harmonic generation by low-frequency laser fields," *Phys. Rev. A*, vol. 49, pp. 2117–2132, 3 Mar. 1994.

[12] P. á. Corkum and F. Krausz, "Attosecond science," *Nature physics*, vol. 3, no. 6, pp. 381–387, 2007.

[13] I. P. Christov, M. M. Murnane, and H. C. Kapteyn, "High-harmonic generation of attosecond pulses in the "single-cycle" regime," *Phys. Rev. Lett.*, vol. 78, pp. 1251–1254, 7 Feb. 1997.

[14] K. Midorikawa, "Progress on table-top isolated attosecond light sources," *Nature Photonics*, vol. 16, no. 4, pp. 267–278, 2022.

[15] M. Chini, K. Zhao, and Z. Chang, "The generation, characterization and applications of broadband isolated attosecond pulses," *Nature Photonics*, vol. 8, no. 3, pp. 178–186, 2014.

[16] S. Mondal *et al.*, “Intense isolated attosecond pulses from two-color few-cycle laser driven relativistic surface plasma,” *Scientific Reports*, vol. 12, no. 1, pp. 1–12, 2022.

[17] F. Demartini, C. H. Townes, T. K. Gustapson, and P. L. Kelley, “Self-steepening of light pulses,”

[18] W. Simmons, J. Hunt, and W. Warren, “Light propagation through large laser systems,” *IEEE Journal of Quantum Electronics*, vol. 17, no. 9, pp. 1727–1744, 1981.

[19] C. Rolland and P. B. Corkum, “Compression of high-power optical pulses,” *JOSA B*, vol. 5, no. 3, pp. 641–647, 1988.

[20] V. Petrov, W. Rudolph, and B. Wilhelmi, “Compression of high-energy femtosecond light pulses by self-phase modulation in bulk media,” *Journal of Modern Optics*, vol. 36, no. 5, pp. 587–595, 1989.

[21] S. Y. Mironov *et al.*, “Thin plate compression of a sub-petawatt ti: Sa laser pulses,” *Applied Physics Letters*, vol. 116, no. 24, p. 241 101, 2020.

[22] C.-H. Lu *et al.*, “Generation of intense supercontinuum in condensed media,” *Optica*, vol. 1, no. 6, pp. 400–406, 2014.

[23] M. Hanna, F. Guichard, N. Daher, Q. Bournet, X. Délen, and P. Georges, “Nonlinear optics in multipass cells,” *Laser Photonics Reviews*, vol. 15, Oct. 2021.

[24] C.-H. Lu, T. Witting, A. Husakou, M. J. Vrakking, A. Kung, and F. J. Furch, “Sub-4 fs laser pulses at high average power and high repetition rate from an all-solid-state setup,” *Optics express*, vol. 26, no. 7, pp. 8941–8956, 2018.

[25] J. Schulte, T. Sartorius, J. Weitenberg, A. Vernaleken, and P. Russbueldt, “Nonlinear pulse compression in a multi-pass cell,” *Optics Letters*, vol. 41, no. 19, pp. 4511–4514, 2016.

[26] M. Hanna *et al.*, “Nonlinear temporal compression in multipass cells: Theory,” *JOSA B*, vol. 34, no. 7, pp. 1340–1347, 2017.

[27] M. Müller, J. Buldt, H. Stark, C. Grebing, and J. Limpert, “Multipass cell for high-power few-cycle compression,” *Optics Letters*, vol. 46, no. 11, pp. 2678–2681, 2021.

[28] C. Vozzi, M. Nisoli, G. Sansone, S. Stagira, and S. De Silvestri, “Optimal spectral broadening in hollow-fiber compressor systems,” *Applied Physics B*, vol. 80, no. 3, pp. 285–289, 2005.

[29] M. Nisoli, S. De Silvestri, and O. Svelto, “Generation of high energy 10 fs pulses by a new pulse compression technique,” *Applied Physics Letters*, vol. 68, no. 20, pp. 2793–2795, 1996.

[30] E. A. Marcatili and R. Schmeltzer, “Hollow metallic and dielectric waveguides for long distance optical transmission and lasers,” *Bell System Technical Journal*, vol. 43, no. 4, pp. 1783–1809, 1964.

[31] M. Miranda *et al.*, “Fast iterative retrieval algorithm for ultrashort pulse characterization using dispersion scans,” *JOSA B*, vol. 34, no. 1, pp. 190–197, 2017.

[32] H. Timmers, Y. Kobayashi, K. F. Chang, M. Reduzzi, D. M. Neumark, and S. R. Leone, “Generating high-contrast, near single-cycle waveforms with third-order dispersion compensation,” *Optics letters*, vol. 42, no. 4, pp. 811–814, 2017.

[33] J. C. Travers, T. F. Grigorova, C. Brahms, and F. Belli, "High-energy pulse self-compression and ultraviolet generation through soliton dynamics in hollow capillary fibres," *Nature Photonics*, vol. 13, no. 8, pp. 547–554, 2019.

[34] J. A. Giordmaine, P. M. Rentzepis, S. L. Shapiro, and K. W. Wecht, "Two-photon excitation of fluorescent by picosecond light pulses," *Applied Physics Letters*, vol. 11, pp. 216–218, 7 Oct. 1967.

[35] R. Trebino *et al.*, "Measuring ultrashort laser pulses in the time-frequency domain using frequency-resolved optical gating," *Review of Scientific Instruments*, vol. 68, no. 9, pp. 3277–3295, May 1997.

[36] D. Kane and R. Trebino, "Characterization of arbitrary femtosecond pulses using frequency-resolved optical gating," *IEEE Journal of Quantum Electronics*, vol. 29, no. 2, pp. 571–579, 1993.

[37] R. Trebino *et al.*, "Measuring ultrashort laser pulses in the time-frequency domain using frequency-resolved optical gating," *Review of Scientific Instruments*, vol. 68, no. 9, pp. 3277–3295, 1997.

[38] K. W. DeLong and R. Trebino, "Improved ultrashort pulse-retrieval algorithm for frequency-resolved optical gating," *J. Opt. Soc. Am. A*, vol. 11, no. 9, pp. 2429–2437, Sep. 1994.

[39] R. Trebino and D. J. Kane, "Using phase retrieval to measure the intensity and phase of ultrashort pulses: Frequency-resolved optical gating," *J. Opt. Soc. Am. A*, vol. 10, no. 5, pp. 1101–1111, May 1993.

[40] C. Iaconis and I. A. Walmsley, "Spectral phase interferometry for direct electric-field reconstruction of ultrashort optical pulses," *Opt. Lett.*, vol. 23, no. 10, pp. 792–794, May 1998.

[41] Y. Coello *et al.*, "Interference without an interferometer: A different approach to measuring, compressing, and shaping ultrashort laser pulses," *J. Opt. Soc. Am. B*, vol. 25, no. 6, A140–A150, Jun. 2008.

[42] J. M. Dela Cruz, I. Pastirk, V. V. Lozovoy, K. A. Walowicz, and M. Dantus, "Multiphoton intrapulse interference 3: Probing microscopic chemical environments," *The Journal of Physical Chemistry A*, vol. 108, no. 1, pp. 53–58, 2004.

[43] B. Xu, J. M. Gunn, J. M. D. Cruz, V. V. Lozovoy, and M. Dantus, "Quantitative investigation of the multiphoton intrapulse interference phase scan method for simultaneous phase measurement and compensation of femtosecond laser pulses," *JOSA B*, vol. 23, no. 4, pp. 750–759, 2006.

[44] Y. Coello, B. Xu, T. L. Miller, V. V. Lozovoy, and M. Dantus, "Group-velocity dispersion measurements of water, seawater, and ocular components using multiphoton intrapulse interference phase scan," *Applied optics*, vol. 46, no. 35, pp. 8394–8401, 2007.

[45] V. V. Lozovoy, B. Xu, Y. Coello, and M. Dantus, "Direct measurement of spectral phase for ultrashort laser pulses," *Opt. Express*, vol. 16, no. 2, pp. 592–597, Jan. 2008.

[46] G. O. Williams *et al.*, "Impact of free electron degeneracy on collisional rates in plasmas," *Physical Review Research*, vol. 1, no. 3, p. 033 216, 2019.

[47] J. Duarte *et al.*, "Computed stereo lensless x-ray imaging," *Nature Photonics*, vol. 13, no. 7, pp. 449–453, 2019.

[48] G. O. Williams *et al.*, "Tracking the ultrafast xuv optical properties of x-ray free-electron-laser heated matter with high-order harmonics," *Physical Review A*, vol. 97, no. 2, p. 023 414, 2018.

[49] *Leader in laser solutions and photonics technology: Coherent*.

[50] A. F. do Carmo Ribeiro, "Development of a mobile frog setup for the measurement of ultrashort laser pulses," M.S. thesis, Instituto Superior Técnico, Universidade de Lisboa, Jul. 2019.

[51] I. Sytcevich *et al.*, "Characterizing ultrashort laser pulses with second harmonic dispersion scans," *JOSA B*, vol. 38, no. 5, pp. 1546–1555, 2021.

[52] L. Verwaal, "Towards generating isolated attosecond xuv pulses through high harmonic generation," Department of Applied physics at Eindhoven University of Technology, 2022.

[53] F. Silva, M. Miranda, B. Alonso, J. Rauschenberger, V. Pervak, and H. Crespo, "Simultaneous compression, characterization and phase stabilization of gw-level 1.4 cycle vis-nir femtosecond pulses using a single dispersion-scan setup," *Optics express*, vol. 22, no. 9, pp. 10 181–10 191, 2014.

[54] M. Miranda, T. Fordell, C. Arnold, A. L'Huillier, and H. Crespo, "Simultaneous compression and characterization of ultrashort laser pulses using chirped mirrors and glass wedges," *Optics express*, vol. 20, no. 1, pp. 688–697, 2012.

[55] E. Conejero Jarque *et al.*, "Universal route to optimal few-to single-cycle pulse generation in hollow-core fiber compressors," *Scientific reports*, vol. 8, no. 1, pp. 1–10, 2018.

[56] C. Bree, A. Demircan, and G. Steinmeyer, "Method for computing the nonlinear refractive index via keldysh theory," *IEEE Journal of Quantum Electronics*, vol. 46, no. 4, pp. 433–437, 2010.

[57] A. L. Gaeta, "Catastrophic collapse of ultrashort pulses," *Physical Review Letters*, vol. 84, no. 16, p. 3582, 2000.

[58] A. Jullien *et al.*, "Carrier-envelope-phase stable, high-contrast, double chirped-pulse-amplification laser system," *Optics letters*, vol. 39, no. 13, pp. 3774–3777, 2014.

[59] S. Koke, C. Grebing, B. Manschwetus, and G. Steinmeyer, "Fast f-to-2f interferometer for a direct measurement of the carrier-envelope phase drift of ultrashort amplified laser pulses," *Optics letters*, vol. 33, no. 21, pp. 2545–2547, 2008.

[60] F. Böhle *et al.*, "Compression of cep-stable multi-mj laser pulses down to 4 fs in long hollow fibers," *Laser Physics Letters*, vol. 11, no. 9, p. 095 401, 2014.

[61] A. Jullien *et al.*, "10^{10} Temporal contrast for femtosecond ultraintense lasers by cross-polarized wave generation," *Optics letters*, vol. 30, no. 8, pp. 920–922, 2005.

[62] T. Nagy, M. Forster, and P. Simon, "Flexible hollow fiber for pulse compressors," *Applied Optics*, vol. 47, no. 18, pp. 3264–3268, 2008.

[63] M. Ouillé *et al.*, "Relativistic-intensity near-single-cycle light waveforms at khz repetition rate," *Light: Science & Applications*, vol. 9, no. 1, pp. 1–9, 2020.

[64] X. Chen *et al.*, “Generation of 4.3 fs, 1 mj laser pulses via compression of circularly polarized pulses in a gas-filled hollow-core fiber,” *Optics letters*, vol. 34, no. 10, pp. 1588–1590, 2009.

[65] A. Jeandet *et al.*, “Survey of spatio-temporal couplings throughout high-power ultrashort lasers,” *Optics Express*, vol. 30, no. 3, pp. 3262–3288, 2022.

[66] A.-L. Viotti *et al.*, “Multi-pass cells for post-compression of ultrashort laser pulses,” *Optica*, vol. 9, no. 2, pp. 197–216, 2022.

[67] R. M. Kaumanns, “Generation of Energetic Femtosecond Pulses at High Average Power,” eng, Ph.D. dissertation, 2020.

[68] L. Daniault *et al.*, “Single-stage few-cycle nonlinear compression of millijoule energy ti: Sa femtosecond pulses in a multipass cell,” *Optics Letters*, vol. 46, no. 20, pp. 5264–5267, 2021.

[69] J. Kaur *et al.*, “Cross-polarized wave generation in multi-pass cells,” in *High Intensity Lasers and High Field Phenomena*, Optica Publishing Group, 2022, JTh6A–2.

[70] N. Minkovski, G. Petrov, S. Saltiel, O. Albert, and J. Etchepare, “Nonlinear polarization rotation and orthogonal polarization generation experienced in a single-beam configuration,” *JOSA B*, vol. 21, no. 9, pp. 1659–1664, 2004.

[71] S. Kourtev, N. Minkovski, L. Canova, A. Jullien, O. Albert, and S. Saltiel, “Improved nonlinear cross-polarized wave generation in cubic crystals by optimization of the crystal orientation,” *JOSA B*, vol. 26, no. 7, pp. 1269–1275, 2009.

[72] A. Jullien *et al.*, “Highly efficient nonlinear filter for femtosecond pulse contrast enhancement and pulse shortening,” *Optics letters*, vol. 33, no. 20, pp. 2353–2355, 2008.

[73] M. Kaumanns, D. Kormin, T. Nubbemeyer, V. Pervak, and S. Karsch, “Spectral broadening of 112 mj, 1.3 ps pulses at 5 khz in a lg 10 multipass cell with compressibility to 37 fs,” *Optics Letters*, vol. 46, no. 5, pp. 929–932, 2021.

[74] G. O. Williams *et al.*, “Fourier transform holography with high harmonic spectra for attosecond imaging applications,” *Optics Letters*, vol. 40, no. 13, pp. 3205–3208, 2015.

[75] E. Hecht, *Optics*. Addison-Wesley, 2001.

[76] A. Suda, M. Hatayama, K. Nagasaka, and K. Midorikawa, “Generation of sub-10-fs, 5-mj-optical pulses using a hollow fiber with a pressure gradient,” *Applied Physics Letters*, vol. 86, no. 11, p. 111 116, 2005.

[77] K. Falk, “Experimental methods for warm dense matter research,” *High Power Laser Science and Engineering*, 2018.

[78] J. Schötz *et al.*, “Phase-matching for generation of isolated attosecond xuv and soft-x-ray pulses with few-cycle drivers,” *Physical Review X*, vol. 10, 4 Oct. 2020.

[79] D. Bar-Lev and J. Scheuer, “Plasmonic metasurface for efficient ultrashort pulse laser-driven particle acceleration,” *Physical Review Special Topics - Accelerators and Beams*, vol. 17, no. 12, Dec. 2014.

[80] A. L'Huillier and P. Balcou, "High-order harmonic generation in rare gases with a 1-ps 1053-nm laser," *Physical Review Letters*, vol. 70, no. 6, p. 774, 1993.

[81] M. Krebs *et al.*, "Towards isolated attosecond pulses at megahertz repetition rates," *Nature photonics*, vol. 7, no. 7, pp. 555–559, 2013.

[82] A. Börzsönyi, Z. Heiner, M. P. Kalashnikov, A. P. Kovács, and K. Osvay, "Dispersion measurement of inert gases and gas mixtures at 800 nm," *Appl. Opt.*, vol. 47, no. 27, pp. 4856–4863, Sep. 2008.

Appendix A

Instruction Manual for the installation of the Hollow-Core Fibre

A new instruction manual will be presented here to ensure a quicker and simpler future replication of our work.

To start, in the new beam line created, directed towards the HCF, one has to be cautious to take extreme care of the polarisation that should be perfectly linear and parallel to the table (in order to cross the Brewster windows placed at the input and output of the fibre). Luckily, the HHG beamline already requires an ultrafast attenuator (Laser Beam Attenuator, Ultrafast Version, Altechna) composed of a waveplate [1] followed by two broadband thin film polarizers. Rotating the waveplate rotates the incoming beam, which is then cleaned by the two broadband polarisers who remove any light whose polarisation is not vertical. In this way, the angle of the waveplate commands the amount of cleaned vertical polarised light that exits the attenuator. Although not ideal, since the polarisation is vertical and not horizontal, this attenuator does insure proper correctement of the polarisation and should be placed at the start of both beamlines, just as seen in figure 2.1. To correct the direction of polarisation a new $\lambda/2$ waveplate must be set afterwards [2].

Once a correctly polarised beam is established, the beam has to be redirected around the Astrella into an axis parallel to the hedge of the optical table. This is a necessity since only there we find a straight line long enough to place the HCF setup while keeping the ability to adjust the alignment. With two dielectric mirrors, the beamline between the lasers is aligned and then two other mirrors align the beam path where the HCF is to be placed. This task requires caution since the beam height needs to match the limitations of the translation stages. Through the same mirrors create a second coincident visible line using a HeNe alignment laser ($\lambda_0 = 632.8$ nm), this will be used in order to safely and easily align the fibre support system.

It is then necessary to study how the beam will be coupled into the fibre itself, for this, an achromatic lens with $f = 750$ mm should be placed right before the second to last mirror. The lens placement is

[1] A $\lambda/2$ waveplate is an optical device that alters the polarisation state of a light wave travelling through it
[2] More information regarding the basics of polarisation can be found in [75].

a consequence of the lack of space in the optical table and the closeness to the mirror is a form of prevention from any damage resulting from the high fluence of the focused beam. As seen in 1.3.2 a very precise beam diameter is necessary to properly couple just the fundamental node and so the lens needs to be installed on top of three manual translation stages (xyz) that allow a correct alignment of the lens and some fine-tuning of the focal spot.

The next step is to find the plane where the beam diameter is exactly $2\omega_0 = 160\mu$m. For this, take advantage of the same beam profiler used in 2.1.2 that, along with measurements of beam pointing, also measures the beam diameter at the plane where it is placed. Some astigmatism may be present at the beam focus and should be corrected through additional alignment of the lens. In our installation, it did not disappear totally, so in the future, it would perhaps make sense to design some new focusing system with more control of aberrations. In any case, the plane closest to the desired 160μm diameter is to be marked on the table in the most careful way possible.

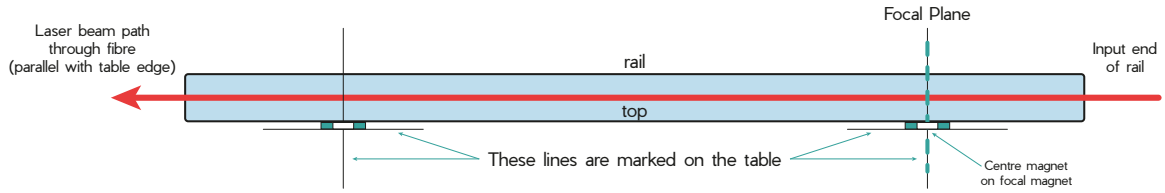

Figure A.1: Schematic of the position of the marked axis used for installation of the hollow core fibre.

Once the previous steps are accomplished, the user can finally start to install the system that supports the fibre. Since the whole setup needs to be perfectly parallel to the table, a flexible enough system should be placed on the table, for our laboratory, it comes in the form of a rail with two magnetic spots which are controlled with two translation stages, one with three-axis and the other with just two (to avoid redundancy at the axis parallel to the table). To know where to place these stages, the following steps should be followed attentively. First, place the rail onto the optical table and make sure to have it follow the beamline. Second, while still being careful to follow the beamline, place the centre of the first magnet at the plane previously drawn on the table, this will be your reference for the placement of the fibre. Lastly, mark on the table the lines described in figure A.1, these are the axis that our translation stages are to follow.

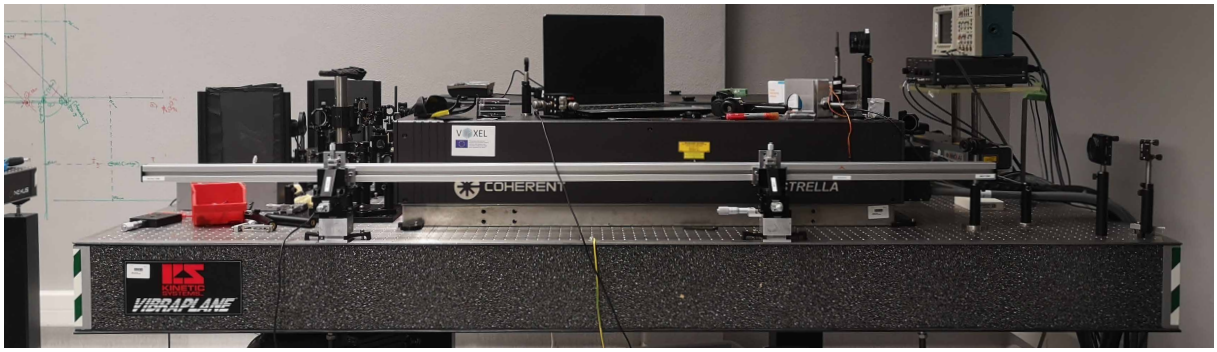

Figure A.2: Rail installed at the VOXEL laboratory.

After a very delicate placement of the translation stages onto the drawn axis, place the rail on top. Two things are of note here: (i) the axis drawn along the rail corresponds to the end of the metal cylinder that will hold the fibre, not to the translation stage itself, (ii) two o-rings need to be placed beneath the rail between the basis and the horizontal axis to prevent any undesired movement. This point in the installation process is shown in figure A.2.

With the rail placed along the beamline it is now necessary to adjust its height to the one set by the beamline. To align this, and to correct any mistake along the other two axes, place on the rail the support blocks that will soon support the fibre. On top of these support blocks, insert an alignment piece (a cylinder piece of glass with a hollow core), made to mimic the fibre throughout the rail. To easily and safely align this setup use only the previously aligned HeNe beam (that also mimicked the HCF beamline). Once the alignment laser is seen at the centre of the alignment piece throughout the rail one can finally say that the rail is aligned. While we performed these steps, a regrettable fact did appear, after several iterations of the alignment process: either the rail or the table are not exactly as parallel to the floor as ideal. A user might notice this flaw in the installation process, however, as unfortunate as it is, one needs not worry since the curvature is within the limits permitted by the fibre geometry.

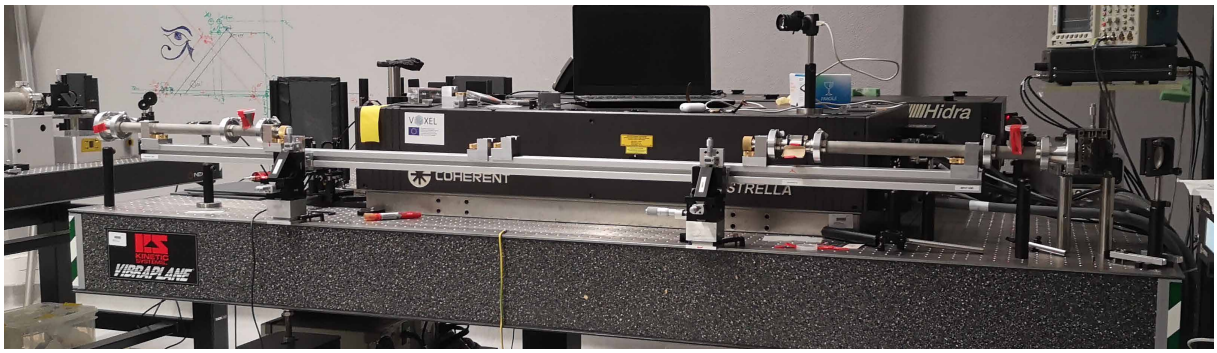

Figure A.3: Installation of the input and output tubes onto the rail.

Once the rail is parallel to the table (within limits), it's time to start building the gas system. For this, place the two tubes with built-in Brewster windows at both extremes of the rail as seen in figure A.3. Needing three operable modes, the spectral broadening system comes also with a gas control station. To be able to implement both vacuum and gas-filled options in the HCF, begin by installing a dry (oil-free) vacuum pump and a Pirani gauge, used to control the number of particles still within the fibre. Both objects need to be connected to the input tube through a 4-way cross where a 6mm OD tube needs also to be placed in order to connect the tube to the gas control as represented by the Vacuum Pump signal in A.4, A.5 and A.7. On the output side, insert a 6mm OD tube and connect it to the gas control station on the right side which is, of course, connected to the supply valve. The gas supply is to be offered by another 6mm OD tube connecting the gas cylinder of noble gas to the pressure regulator on the gas control station. In order to fit the range of the gas control station a new pressure regulator has to be placed on the output of the gas cylinder to maintain the pressure in the tube between 4 and 10 bar.

As before mentioned the system needs to work in three different modes: evacuation, static fill and differential pumping. We will now describe them.

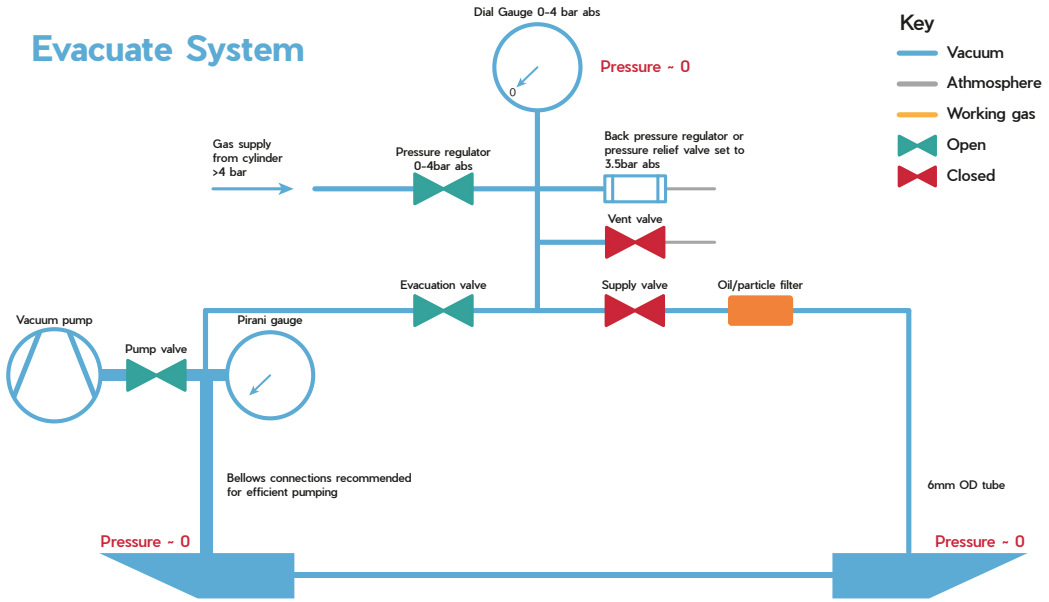

Figure A.4: Schematic of the Evacuate System mode used to clean impurities.

The first, used to clean all the impurities present within the tubes of the whole system, is represented in figure A.4. This mode, of course, requires the pump valve to be open, as well as the evacuation valve. It is also necessary to open the pressure regulator but not before closing the gas cycling valve, since this mistake might cause the user a whole cylinder of very rare and expensive gas. This mode is also the reason why, for safety, we need the vent valve connected to an external exhaust tube.

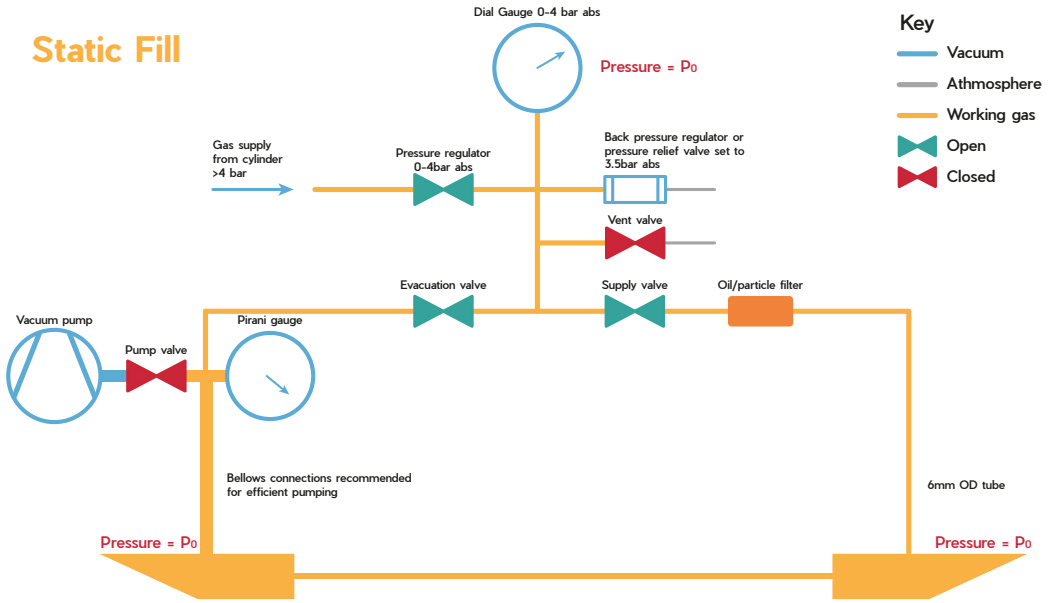

Figure A.5: Schematic of the Static Fill mode used for constant pressure.

The second, represented in figure A.5, enables a static fill of the noble gas throughout the entire fibre. For this, we close the pump valve as well as the vacuum pump and open the supply valve. To make sure the proper pressure is achieved and there are no impurities are present in the fibre, the first mode should be performed before starting this one. It also makes sense to close the pressure regulator

down to 0 after the vacuum method so that the next mode can be properly controlled.

The third, and final mode, represented in figure A.7, represents the most recent innovation in the world of hollow-core fibres, the differential pumping system, introduced by K. Midorikawa's group. This technique consists of inputting the gas at the output while evacuating the beam path at the front part of the waveguide [76]. This is done in order to mitigate filamentation-induced beam reshaping at the entrance of the fibre that can prevent the proper coupling of the beam. An example of filamentation is shown in figure A.6.

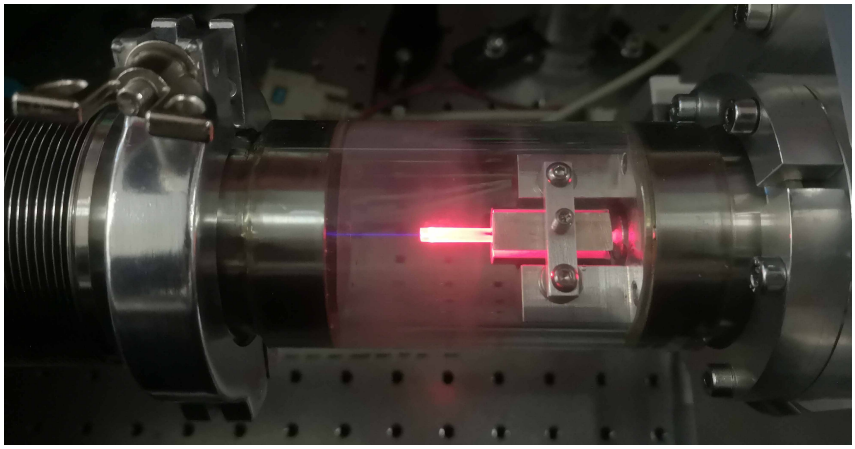

Figure A.6: Example of ionisation at the entrance of a fibre.

This technique also makes the nonlinear interaction build up gradually which delays self-focusing and ionisation inside the fibre suppressing higher-order eigenmodes. In this gas control station, the technique is achieved by closing the evacuation valve and opening the pump valve. This mode will obviously require a higher input pressure and will decrease the effective interaction length to around $L_{eff} \sim 2/3L$ but the fibre already had the length necessary for this procedure.

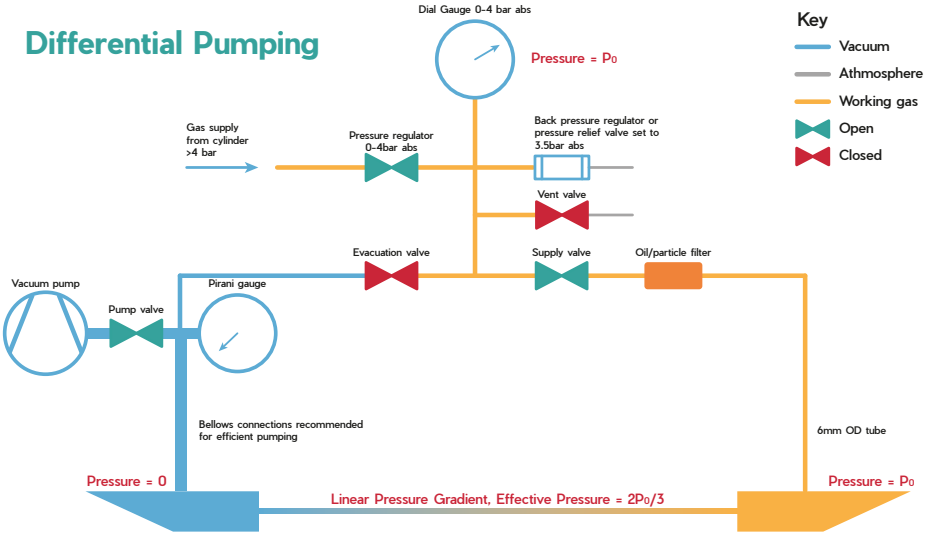

Figure A.7: Schematic of the Differential Pumping mode used to create a linear pressure gradient.

The final step in this long operation is, naturally, to place the fibre itself. The fibre at the VOXEL

lab is a one-meter-long fibre from Imperial College London Consultants with an inner core of 250 μm. The fragility of the cladding and the incredibly thin geometry of the waveguide make this an exceedingly delicate task. To start, both the input and output tubes are placed further away from the centre of the rail to create enough space to place the fibre carefully onto the support blocks. The fibre can only be only held with glove-covered hands to prevent any contamination from oil or other natural contaminants. At both ends of the waveguide, place a brass nut followed by an o-ring, attentively, over the fibre, with extreme care not to touch its tip. After, to allow the proper coupling necessary, place the entrance of the fibre at the focal plane with the "top" tag pointing to the ceiling. While making sure that the fibre remains fixed at the proper placement just achieved, move the input tube slowly through the fibre until it is seen on the small window present on the mentioned tube. Again, while securely fixing the fibre, but not so aggressively to cause damage, reallocate the output tube to a place where only 5 cm of the fibre are coupled inside the tube. The final task is to securely tighten the bolts by hand while avoiding any sort of torsion or rotation of the fibre [3].

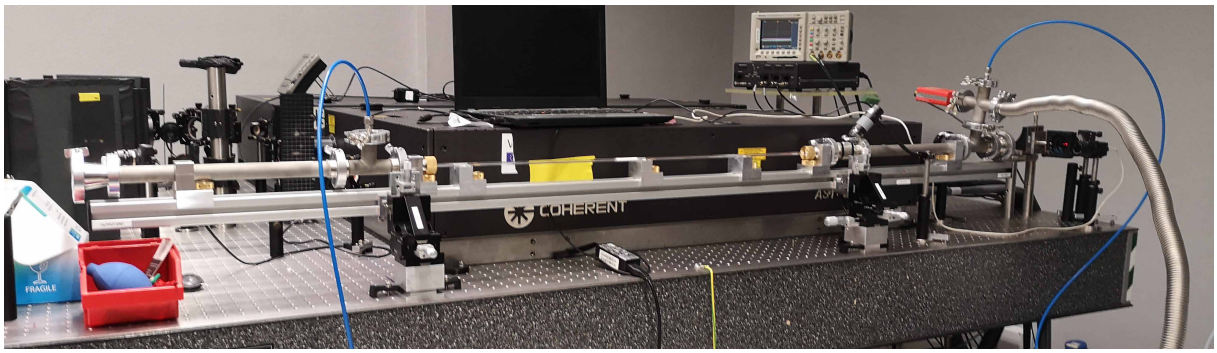

Figure A.8: Whole Setup installed, including the Hollow-Core Fibre.

The whole spectral broadening system is schematised in figure A.9.

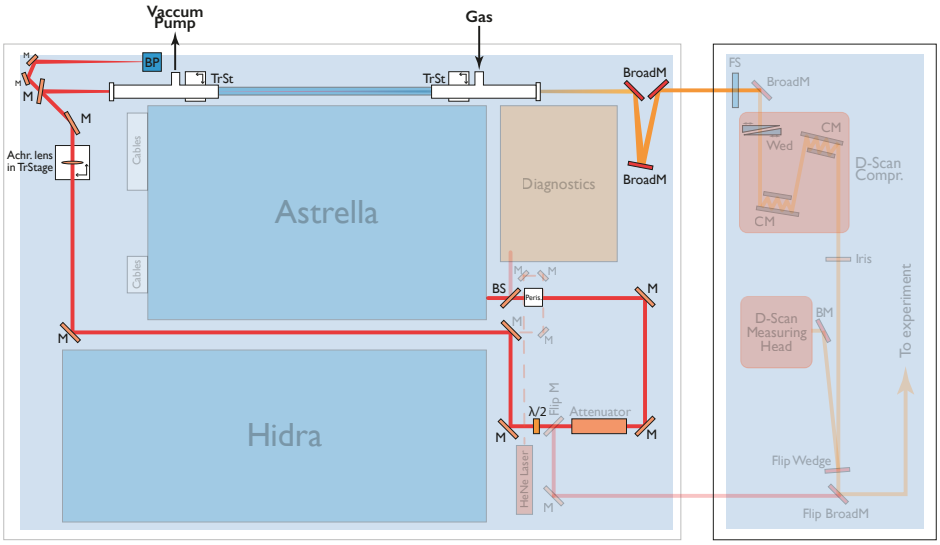

Figure A.9: Scheme of the setup of the HCF in the VOXEL lab.

[3] This step cannot be forgotten or underachieved in any way. Starting the vacuum pump with the brass nuts still loose, even a little, would suck the fibre out of place, as we learned from experience.